UTTAC-94, 2025

UTTAC

ANNUAL REPORT 2024

TANDEM ACCELERATOR COMPLEX, CRiES, University of Tsukuba
https://www.tac.tsukuba.ac.jp/

UTTAC

ANNUAL REPORT 2024

April 1, 2024 – March 31, 2025

UTTAC-94, 2025

Editors: T. Moriguchi, K. Sasa, Y. Yamato, M. Matsumura, and E. Kita
Editorial Team: M. Sataka, H. Naramoto, and H. Kudo (Editor-in-Chief)

UTTAC ANNUAL REPORT is a series of issues, which describes annual research activities at Tandem Accelerator Complex, Center for Research in Radiation, Isotopes, and Earth System Sciences (CRiES), University of Tsukuba.

All reports are written on authors' responsibility and thus the editorial staff are not liable for the contents of the report.

Tandem Accelerator Complex, CRiES, University of Tsukuba
Tennodai 1-1-1, Tsukuba, Ibaraki 305-8577, Japan
annual@tac.tsukuba.ac.jp

***Cover*:** Sample Collection for Accelerator Mass Spectrometry (AMS): Investigation of Iodine-129 in Spring Water in Kanazawa

PREFACE

This annual report covers research and development (R&D) carried out at University of Tsukuba Tandem Accelerator Complex (UTTAC) during the fiscal year 2024 (1 April 2024 – 31 March 2025). The topics include not only accelerator-based R&D using the 6MV tandem and 1MV Tandetron accelerators, but also radioisotope-based R&D employing positron annihilation spectroscopy and Mössbauer spectroscopy. It should be noted that several issues within industry-led research remain unreported, mainly due to patent-related concerns.

September 1, 2025

Editorial Board

Newly enrolled students visiting the accelerator facility at UTTAC are being briefed on its operations.

CONTENTS

1.

ACCELERATOR OPERATION AND RELATED STUDIES

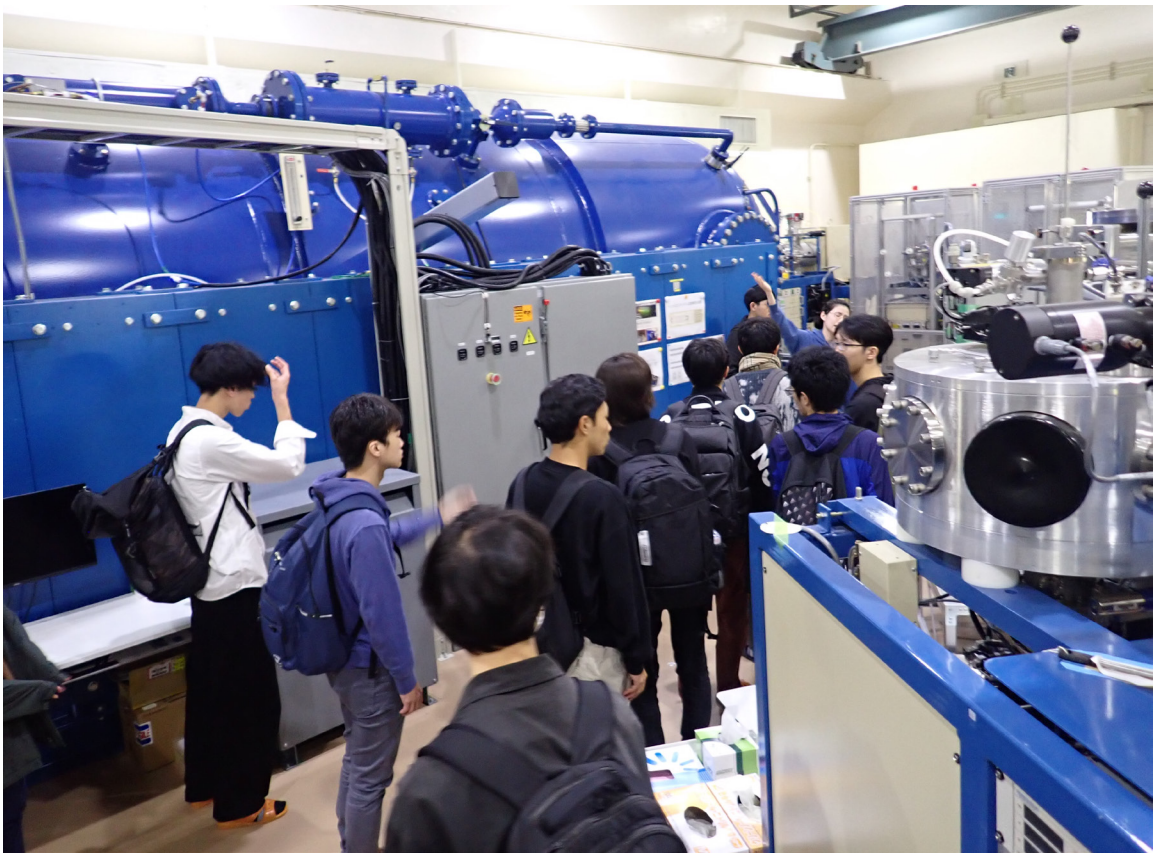

Undergraduate students on a tour learn about the tandem accelerator from a graduate student.

1.1 Accelerator operation 2024

T. Yoshida, S. Ishii, T. Takahashi, Y. Yamato, M. Matsumura, T. Moriguchi, K. Sasa

University of Tsukuba Tandem Accelerator Complex (UTTAC) is promoting the maintenance and operation of the tandem accelerator facility consisting of the 6MV Pelletron tandem accelerator and the 1MV Tandetron accelerator for cooperative researches both inside and outside University of Tsukuba.

1MV Tandetron accelerator

The 1MV Tandetron accelerator has 2 negative ion sources and 4 beamlines. The operating time and the experimental beam time of the 1MV Tandetron accelerator were 2,368.5 and 517.1 hours, respectively, during the total service time in FY2024. The 1MV Tandetron accelerator operated for 102 days in FY2024, with 382 participants and 59 research programs conducted. Figures 1 and 2 show classification of the accelerated ions and of experimental purposes, respectively. In FY2024, many molecular beams of H_2, Li_2, C_2, CH_2, O_2 and OH were supplied for cluster-beam experiments. At the end of March 2025, the total number of approved research programs was 5 for on-campus and 3 for off-campus. The terminal voltage instability, reported since FY2022, has been also observed sometimes in FY2024. This troublesome problem has been mostly resolved by long conditioning before operating the accelerator.

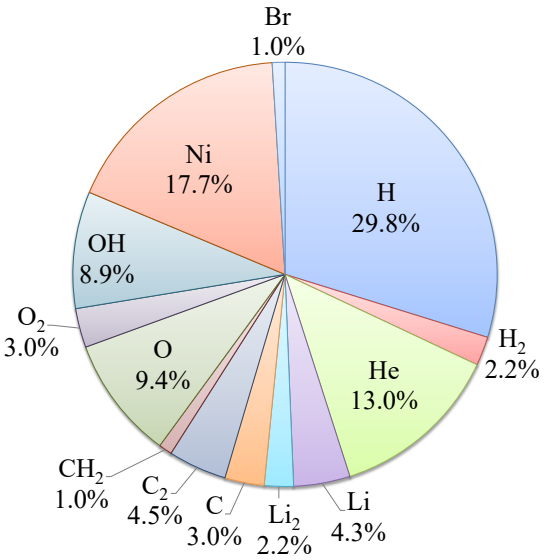

Fig. 1. Accelerated ions by the 1MV Tandetron accelerator in FY2024.

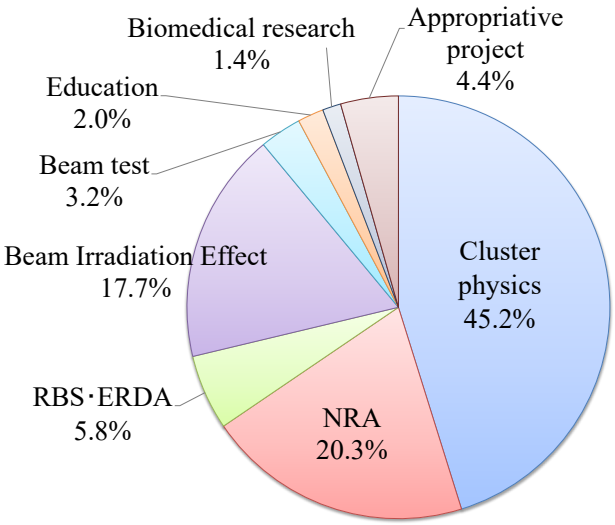

Fig. 2. Utilization details of the 1MV Tandetron accelerator during FY2024.

6MV Pelletron tandem accelerator

The 6MV Pelletron tandem accelerator has 5 negative ion sources and 12 beamlines. The operating time and the experimental beam time of the 6MV Pelletron tandem accelerator were 1,481.7 and 1,265.1 hours, respectively, during the total service time in FY2024. The operating time increased by about 52% compared to that in the last fiscal year [1]. The experimental beam time in FY2024 is the longest since FY2020 when

the activity in research and education at UTTAC was seriously influenced by the COVID-19 disaster. The 6MV Pelletron tandem accelerator operated for 133 days in FY2024, with 955 participants and 83 research programs conducted. Figure 3 shows the beam time histogram with respect to the terminal voltage. Figures 4 and 5 show classification of the accelerated ions and of the experimental purposes, respectively. At the end of March 2025, the number of approved research programs was 14 for on-campus and 6 for off-campus.

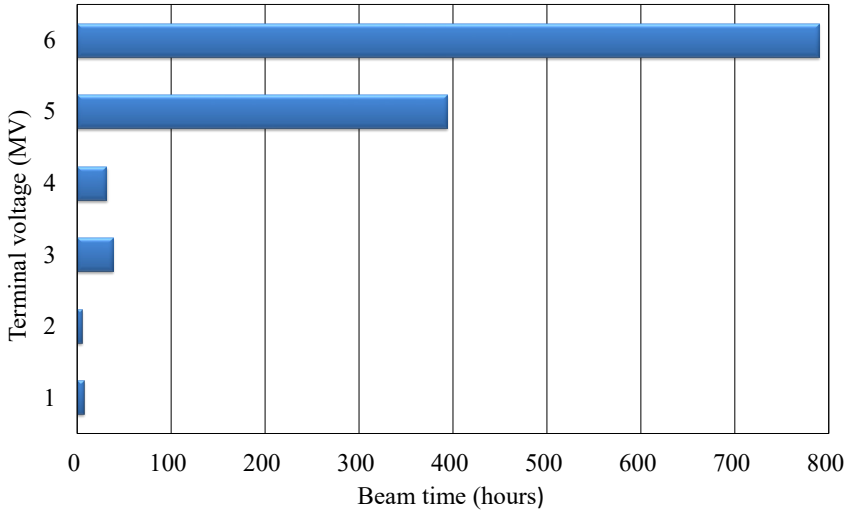

Fig. 3. Beam time histogram as a function of the terminal voltage for the 6MV Pelletron tandem accelerator in FY2024.

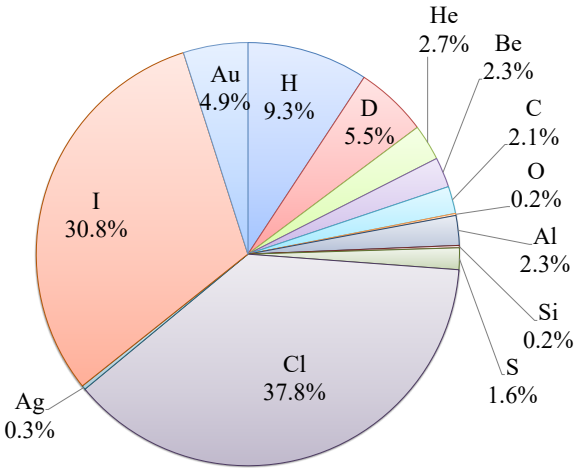

Fig. 4. Accelerated ions by the 6MV Pelletron tandem accelerator in FY2024.

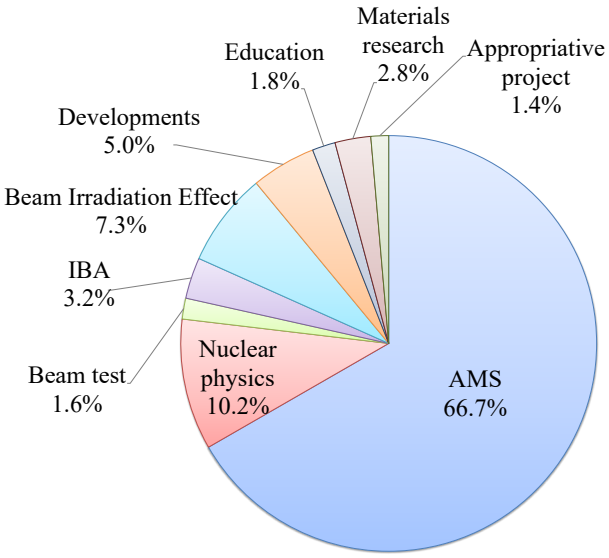

Fig. 5. Utilization details of the 6MV Pelletron Tandem Accelerator during FY2024.

Reference

[1] T. Moriguchi et al., UTTAC Annual Report 2023, UTTAC-93 (2024) 1.

1.2 Approach to possible energy of ions obtainable with the 6MV tandem accelerator

M. Sataka, T. Takahashi, H. Naramoto, H. Kudo, K. Sasa

Acceleration tests of ion beams from the 6MV tandem accelerator are ongoing [1]. While our focus has been on high-energy ion beams, there is a recent requirement of low-energy heavy ion beams [2]. In this year, we have conducted acceleration tests with low terminal voltages.

We measured beam current distributions of Au ions at terminal voltages of 2 and 3 MV. Figure 1 shows the results of Au ion acceleration tests for terminal voltages between 2 and 6 MV, together with the previous data [1]. The dependence of ion current on the terminal voltage is not very accurate. It is seen that the ion current distribution at a terminal voltage of 2 MV is extremely lower than the others. This is because the injected ion current to the accelerator cannot be increased due to serious electron loading.

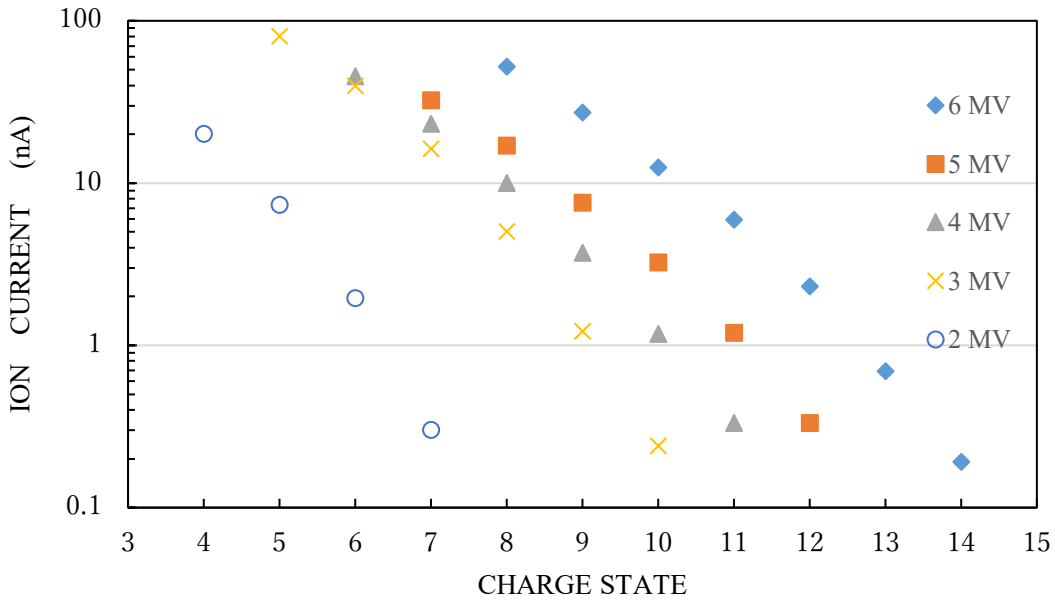

Fig. 1. Ion beam current distributions of Au ions at terminal voltages from 2 to 6 MV.

We have also tested acceleration of low-energy H^+ ions below 1 MeV without using a shorting rod. In this case, molecular ions of TiH^- and CaH_3^- were used as injected ions. TiH^- ions were accelerated with a terminal voltage of 1 MV, decomposed with a gas stripper, thereby we obtained a ~1 MeV H^+ beam with ~0.1 nA current, together with H_2^+ and H_3^+ ion beams. Similarly, CaH_3^- ions were accelerated with a terminal voltage of about 1.5 MV, decomposed with a gas stripper, thereby a 0.5 MeV H^+ beam with ~0.001 nA current was obtained. The H^+ beams thus accelerated can be used for experiments requiring a faint H^+ beam.

Faint beams are so far used mainly for radiation resistance test of electronic devices for space use [3]. However, it was found that impurity ions can be accidentally mixed into a high-energy faint beam. Figure 2 shows energy spectra of Si ions accelerated to 66 and 72 MeV, which were measured using a surface barrier detector in a scattering chamber after passing through the analyzing magnet. The 66 MeV Si beam contains an impurity content of about 1%, although it is negligible in most of the irradiation resistance tests. The source of these impurities is currently unknown. Indeed, the impurity content does not change by changing

the ion cones of negative ion source, nor by changing the setting of the stripper inside the accelerator terminal. Furthermore, the impurities do not significantly change by slightly changing the applied currents of the bending magnet and Q-lenses to increase the scattered beam at the inner surface of the vacuum equipment. Table 1 shows the ions which are verified as usable faint beams. The ions with lower charge states than those presented by red circles are also available. Note that these ions are free of impurities.

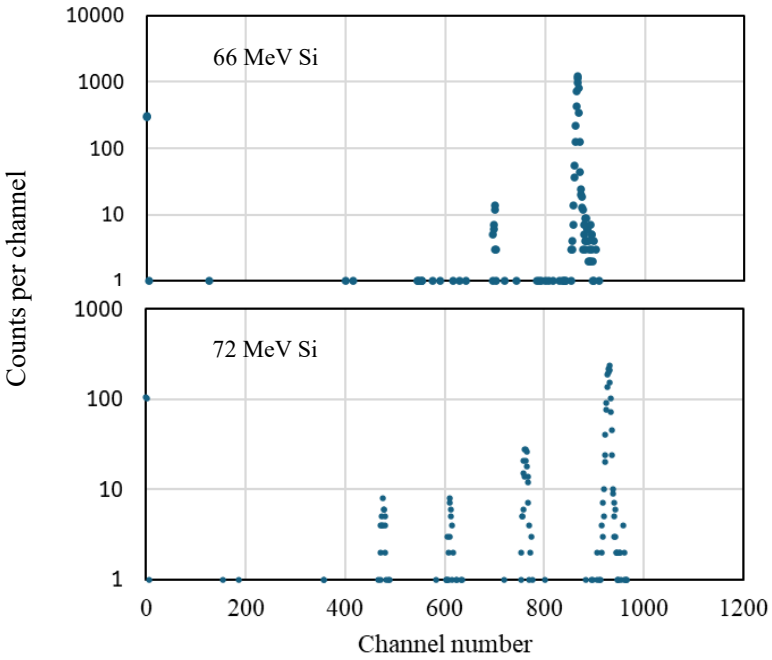

Fig. 2. Energy spectra of Si beams accelerated to 66 MeV (top) and 72 MeV (bottom). The peaks at lower than 800 channel are due to impurities, see the text.

Table 1. Ions that can be used at present as faint beams without impurities

charge	Energy								
state	(MeV)	H	Li	C	O	F	Al	Si	S
14	90								
13	84								
12	78								
11	72								○
10	66							○	
9	60						○		
8	54				○	◌			
7	48							○	
6	42			○					
5	36				◌				
4	30								
3	24		◌		○				
2	18								
1	12	◌							

References

[1] M. Sataka et al., UTTAC Annual Report 2023, UTTAC-93 (2024) 5 and references therein.

[2] K. Awazu et al., this annual report 4.4.

[3] M. Takahashi et al., this annual report 5.2.

2.

NUCLEAR AND COLLISION-BASED RESEARCH

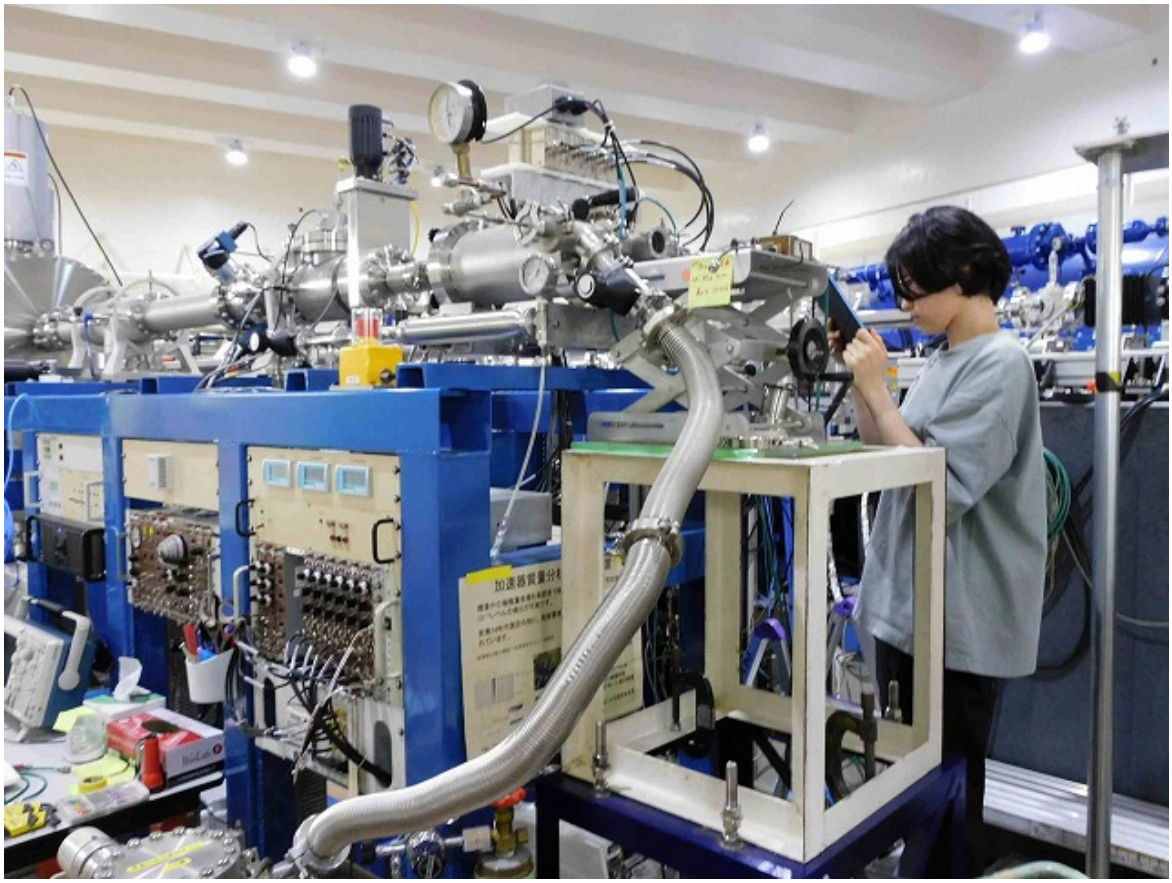

Detector Setup for Experiments with Unstable Nuclear Beams

2.1 Measurement of a low-energy reaction cross section of deuteron on a carbon target

K. Watanabe[1], R. Iwamoto[1], Y. Kikuchi[1], D. Nagae[1], S. Nishizawa[1], T. Suzuki[1], K. Takiura[1], T. Yamaguchi[1,2], I. Yasuda[1], T. Moriguchi, H. Kobayashi, M. Mikawa, M. Mitsui, A. Ozawa, A. Yano

We report an ongoing project of the reaction cross section of deuteron on a carbon target at low energy. The aim of this experiment is to examine the applicability of low-energy reaction cross sections to determine matter radii with Glauber model type analysis. Generally, reaction cross sections have been measured at energies higher than 40 MeV/nucleon at in-flight facilities [1]. The Glauber model analysis has been applied to determine matter radii, where the cross sections are described as a sum of individual nucleon-nucleon scatterings between the projectile and target. With the advancement of recent isotope separation on-line (ISOL) and post-acceleration techniques, many low-energy radioactive beams have been developed. Therefore, a new low-energy technique of radius measurement for radioactive nuclei is desired. This study will be a challenge to extend the conventional method at high energies to low energies. The measured cross sections will also contribute to a basic reaction database for various applications.

A 12 MeV deuteron beam from the 6MV tandem accelerator at UTTAC was delivered to the A7 course, where a set of detector telescopes was arranged in a vacuum chamber. The intensity of the faint beam used was typically 600 cps with an additional collimator (ϕ8 mm in diameter) in front of the detector system. The incident deuterons were counted using a newly developed plastic scintillation detector placed upstream of the reaction target. The detector consists of a 100-μm-thick plastic scintillator (Eljen Technology EJ-212, 6 mm height $\times$ 6 mm width) light shielded by a 2-μm-thick aluminized mylar and multi-pixel photon counters (MPPC: Hamamatsu Photonics S13360-6075CS) optically guided from the both ends. A photograph of the detector is shown in the left panel of Fig. 1, where the detector placed on an aluminum stand is compact to be used anywhere for beam monitoring. The energy deposit to the plastic scintillator in the present case was approximately 0.76 MeV. Typical signals from the MPPC are shown in the right panel of Fig. 1, where both pulses from the ends of the scintillator were $\sim$400 mV after a proper amplification for charge measurement. A carbon target with a thickness of 15 mg/cm^2 was used as a reaction target. It was mounted on a movable ladder frame in the chamber. Downstream of the reaction target, particle identification was performed using a ΔE-E counter telescope consisting of three silicon detectors (S1, S2, and S3), each with a thickness of 190 μm.

The transmission method was used to measure the reaction cross section, σ_R, described as

$$\sigma_R = -\frac{1}{t} \ln \left(\frac{R_i}{R_o} \right), \tag{1}$$

where t denotes the target thickness, i.e., the number of nuclei per unit area. $R_i = N_2^i/N_1^i$ represents the ratio of counts of outgoing deuterons N_2^i to that of the incoming ones N_1^i for a target-in run. $R_o = N_2^o/N_1^o$ is a similar ratio for a target-out run, which is necessary to subtract the reaction

[1]Saitama University
[2]Visiting associate professor appointment

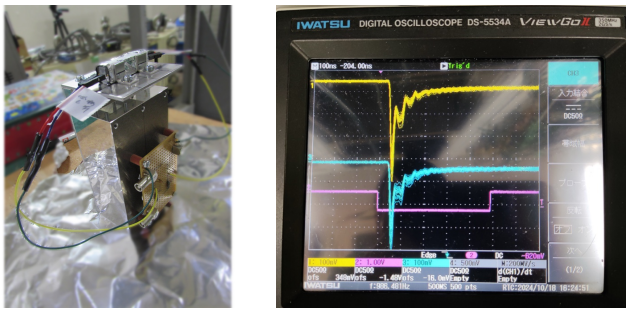

Fig. 1. Setup of the detector and typical pulse shape from the deuteron counter placed upstream of the reaction target.

events in the detectors. Note that the incident beam energy was the same for the target-in and target-out runs. The deuteron counter upstream provides N_1^i and N_1^o in a proper gate on an energy deposit spectrum. The numbers of unreacted deuterons, N_2^i and N_2^o, are obtained from the silicon stack telescope downstream. Separating protons and deuterons in the telescope is essential. The protons are produced from either the deuteron breakup or $^{12}\mathrm{C}(d,p)$ stripping reaction. Figure 2 shows a typical particle identification plot in which the hyperbolic loci of deuterons and emitted protons are clearly observed. An analysis of the ΔE-E method is in progress.

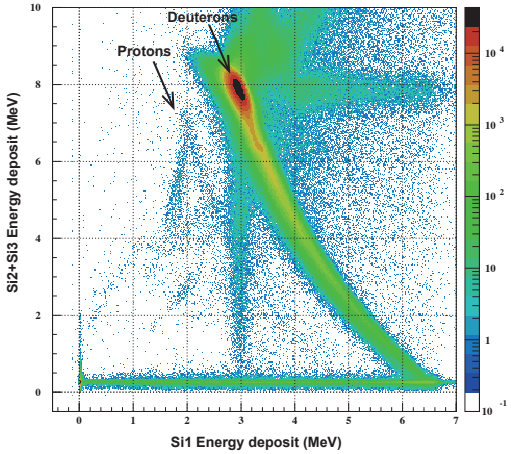

Fig. 2. Typical particle identification plot of the silicon ΔE-E counter telescope. The horizontal axis shows an energy deposit in Si1, and the vertical axis shows the sum of those in Si2 and Si3.

In summary, as the first attempt at measuring low-energy reaction cross sections, the transmission method was effective, providing a good separation of deuterons and protons. However, for a conclusive result, more systematic data with better statistics are needed. In the near future, we will apply for an upgraded experiment to reduce the systematic uncertainties related to the pileup effect, different target materials and thicknesses, and beam energy adjustments.

Reference

[1] A. Ozawa, in *Matter radii and density distributions*, edited by I. Tanihata, H. Toki, T. Kajino, Handbook of Nuclear Physics (Springer 2023), Chapter 6.

2.2 Gamma-ray measurement induced by the ^{7}Li(p, n)^{7}Be reaction

T. Moriguchi, A. Ozawa, M. Mikawa, M. Mitsui, K. Sasa, T. Takahashi, S. Ishii

The amount of ^{7}Li production predicted by the Big Bang nucleosynthesis (BBN) [1] is estimated to be about three times higher than the observation. This discrepancy, called the cosmological lithium problem, remains an open question [2]. The amount of ^{7}Li produced in BBN is considered to depend on that of ^{7}Be ($T_{1/2}$ = 53.3 days) produced, hence the nuclear reactions involved in the production or destruction of ^{7}Be are important. Extracting ^{7}Be directly from the tandem accelerator as an ion beam is expected to be useful for studies of nuclear reactions related to BBN. For this purpose, it is necessary to prepare samples containing ^{7}Be for the ion source. In FY2024, we attempted to produce ^{7}Be via the ^{7}Li(p, n)^{7}Be reaction.

When ^{7}Be decays to ^{7}Li via electron capture, the resulting ^{7}Li nucleus, initially in its first excited state, transitions to the ground state by emitting a 477.6 keV gamma ray. The detection of this gamma ray is evidence for the production of ^{7}Be. In the present experiment, a 2 MeV proton beam of ~100 nA current from the 1MV Tandetron accelerator was used to irradiate a Li_2O target placed in the vacuum chamber on the C course. This target was made by pressing a mixture of Li_2O and Ag powders. An energy threshold of proton beams for the ^{7}Li(p, n)^{7}Be reaction is 1.88 MeV. After the irradiation for 30 minutes, the Li_2O target was removed from the vacuum chamber. Its gamma-ray spectrum was measured by a high-purity germanium detector (Canberra Industries, Inc., Cryo-Pulse 5 plus) for 40 minutes.

Figure 1 shows the measured gamma-ray spectrum. The 477.6 keV peak is clearly observed. Taking the experimental conditions into account, the observed yield of this peak is in reasonable agreement with the prediction derived from the nuclear database [3]. Next, we will measure the yield of ^{7}Be contained in rainwater using sample preparation procedures for accelerator mass spectrometry.

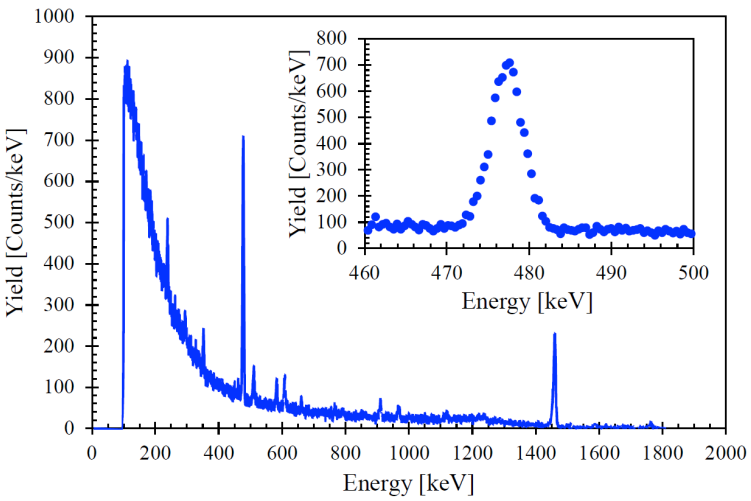

Fig. 1. Gamma-ray spectrum of a Li_2O target irradiated with a 2 MeV proton beam. The inset shows the expanded spectrum around the 477.6 keV peak.

The present experiment was conducted as part of a course of Target Oriented Group Study offered by the College of Physics, and we thank Y. Saito, who was a student of this course, for the data analysis.

References

[1] R. H. Cyburt et al., Rev. Mod. Phys. 88 (2016) 015004.

[2] B. D. Fields: Ann. Rev. Nucl. Part. Sci. 61 (2011) 47.

[3] EXFOR Database, IAEA Nuclear Data Section, https://www-nds.iaea.org/exfor.

2.3 Development of ^{10}Be and ^{14}C beams using an AMS system for nuclear experiments

M. Mikawa, T. Moriguchi, A. Ozawa, K. Sasa, T. Takahashi, M. Matsumura, T. Yoshida, A. Yano, H. Zhang, M. Mitsui, T. Matsumoto, H. Kobayashi

Accelerator Mass Spectrometry (AMS) can detect extremely small amounts of long-lived nuclides (^{10}Be, ^{14}C, ^{36}Cl, ^{129}I, etc.). It has been applied for studies of environmental dynamics using seawater or rainwater, and of cosmic ray event using Antarctic ice core [1]. We are attempting to use the AMS system at UTTAC as an RI beam generator of long-lived nuclides. The RI beams produced by the AMS system have an advantage of highly monoenergetic character since they are provided directly from the ion source, not by nuclear reactions. To use an RI beam of a long-lived nuclide from the AMS system, it is needed to minimize energy loss when passing through absorber gas, and increase beam intensity (1 to 10 kcps). In FY2024, we mainly developed ^{10}Be and ^{14}C beams.

Figure 1 shows the experimental setup at the end of the AMS beamline (L4). To btain a ^{10}Be beam, the pressure of the Ar absorber gas was optimized, thereby eliminating the interference of ^{10}B due to its larger energy loss in the absorber than ^{10}Be. In the standard setting for ^{10}Be-AMS, the absorber is filled with Ar gas at 71.5 Torr. We reduced the Ar gas pressure, while the ionization chamber (IC) for particle identification was kept vacuum. The signals of ^{10}Be and ^{10}B were measured by a newly installed silicon semiconductor (Si) detector at the end of the beam line.

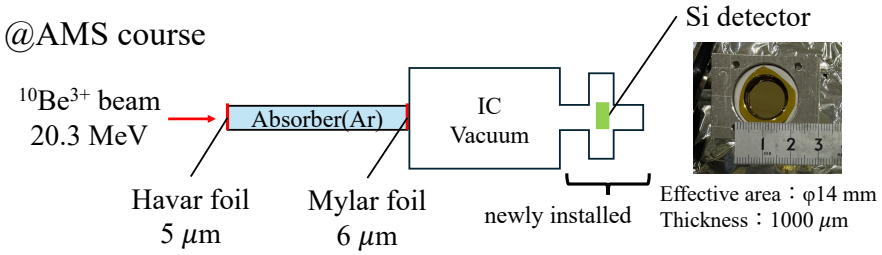

Fig. 1. Experimental setup for ^{10}Be.

Figure 2 shows energy spectra obtained from the Si detector (a) for the AMS setting and (b) for reduced gas pressure. When the Ar gas pressure is 73 Torr (the AMS setting), ^{10}Be is mainly counted (Fig. 2(a)). However, when the Ar gas pressure is reduced to 53 Torr, the number of ^{10}B counts becomes as high as that of ^{10}Be (Fig. 2(b)). Below 40 Torr, the intensity of ^{10}B is so high that the Si detector malfunctions. Additionally, the count rate of ^{10}Be is maximally ∼70 cps for the standard sample (^{10}Be/Be ∼ 10^{-11}) in ^{10}Be-AMS. To ensure the availability of ^{10}Be beams, it is required to remove ^{10}B signals while increasing the ^{10}Be intensity.

To develop ^{14}C beams, we reduced the P10 gas pressure of IC. Figures 3(a) and (b) show the particle identification (PI) diagrams of IC when the gas pressure of P10 is 70 and 10 Torr,

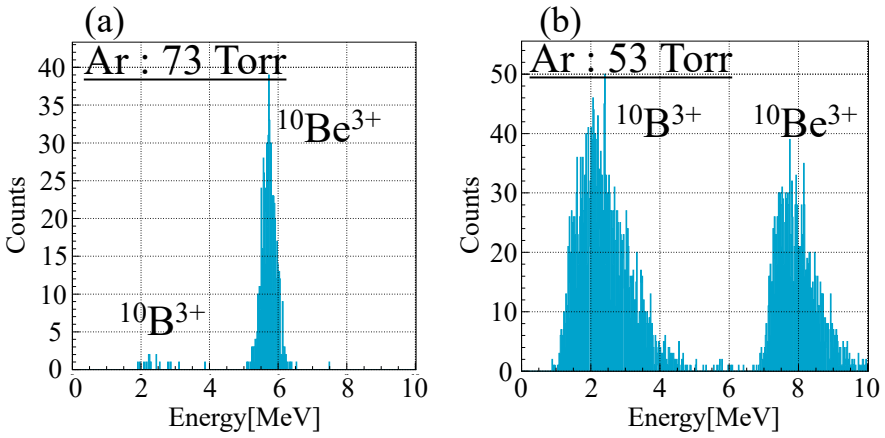

Fig. 2. Energy spectra obtained by the downstream Si detector when IC was evacuated and the absorber gas pressure was set to (a) 73 and (b) 53 Torr.

respectively. In the standard AMS setting, the pressure of P10 in IC is 75 Torr. At a similar pressure of 70 Torr, ^{14}C can be sufficiently separated from the interfering nuclide $^{7}Li^{2+}$ and noise, as shown in Fig. 3(a). The count rate of ^{14}C for the standard sample ($^{14}C/C \sim 10^{-12}$) is maximally ~100 cps. As shown in Fig. 3(b), ^{14}C can be separated from noise even at a pressure of 10 Torr. The energy of ^{14}C after passing through IC at this time is expected to be 18.9 MeV. In addition, when all materials are removed from inside the beamline, the energy width (σ/mean) of ^{14}C is 0.2% when using the Si detector, as shown in Fig. 3(c). In the case of ^{14}C, the influence of interfering nuclides is found to be smaller than that of ^{10}Be, yet a more intense beam is needed.

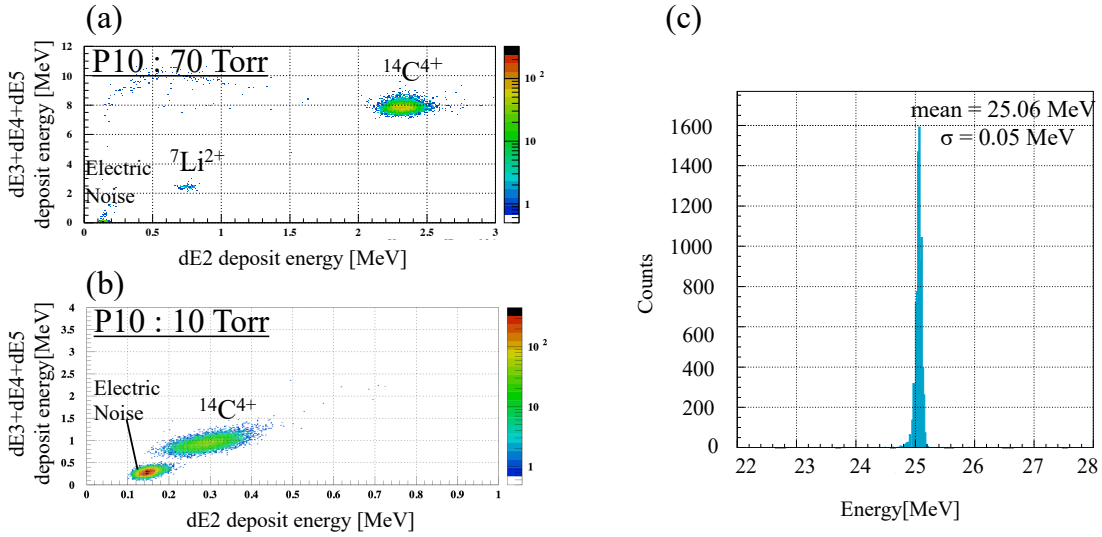

Fig. 3. Particle identification (PI) diagrams in IC when P10 gas pressure is (a) 70 and (b) 10 Torr. (c) Energy spectrum measured by the Si detector when all materials in the beamline were removed.

Reference

[1] K. Sasa et al., this Annual Report 3.1.

2.4 Observation of β-NMR effect of ^{31}S

A. Ozawa, T. Matsumoto, H. Kobayashi, M. Mikawa, M. Mitsui, T. Moriguchi, Y. Yamato, A. Yano, H. Zhang

The nuclear magnetic moment μ is significantly sensitive to nuclear structure. Since the nuclear structure information for unstable nuclei is very limited, measurement of μ for unstable nuclei is indispensable. There are some unstable nuclei, where its absolute μ is known but its sign is unknown. One of them is the unstable nucleus ^{31}S (I^{π}=1/2^{+}, $T_{1/2}$=2.6 s) [1]. Recently, we established effective method to determine the sign of μ [2]. We can apply this method to ^{31}S if we can observe enough β-NMR effect.

In this time, we observed β-NMR effect of ^{31}S using UTTAC 6MV tandem accelerator. To create β-NMR effect, production of polarized ^{31}S is indispensable. Polarized ^{31}S was produced using the polarization transfer reaction ^{31}P($\vec{p}$, n)^{31}S, where a polarized proton ($\vec{p}$) beam was produced from a Lamb-shift-type polarized ion source [3]. The beam energy was 7.9 MeV, and the target was red phosphorous powder which was pressed with Ag to the thickness of roughly 0.5 mm. To investigate the β-NMR effect, static magnetic field H_0=4.45 kG was applied. We also applied the adiabatic fast passage method. To confirm the production of ^{31}S, we checked β-decay lifetime.

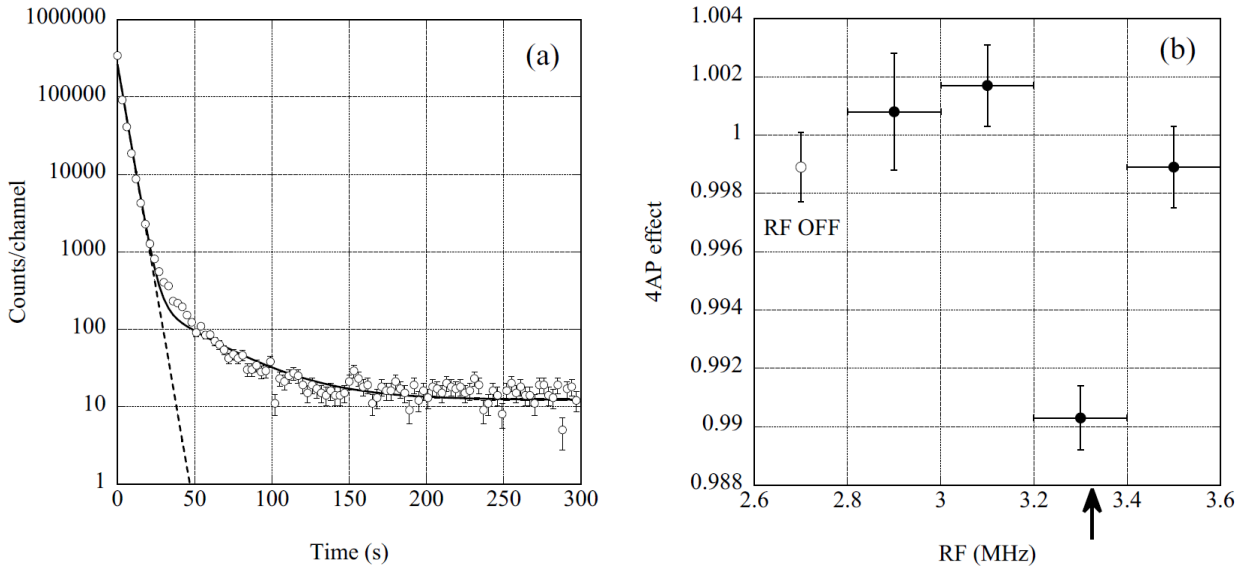

Fig. 1. (a) Typical time spectrum of β-rays for the red phosphorous irradiated with the polarized proton beam of 7.9 MeV. The solid line shows a fitting result using Eq. (1), while the broken line shows the component of ^{31}S. (b) Observed β-NMR spectrum for H_0=4.45 kG. The open circle shows the effect without RF. The arrow shows the Larmor frequency (3.313 MHz) of ^{31}S for H_0=4.45 kG.

The result is shown in Fig. 1. We analyzed the decay curve by the following equation

$$y = C_1 \exp\left(-{}^{\ln 2}/_{2.6} \cdot t\right) + C_2 \exp\left(-{}^{\ln 2}/_{C_3} \cdot t\right) + C_4 , \qquad (1)$$

where C_1~C_4 are variable parameters. A fitted curve is shown by the solid line in Fig. 1 (a). The component of ^{31}S is shown by the broken line in Fig. 1 (a). Thus, ^{31}S is clearly produced. The observed β-NMR spectrum is shown in Fig. 1 (b). The arrow indicates the Larmor frequency (3.313 MHz) of ^{31}S for H_0=4.45 kG. The present β-NMR effect (4AP effect) is roughly 1% with more than 3-σ significancy. It is noted that this effect is roughly half of that reported in Ref. [1]. Since the significant β-NMR effect was observed successfully, we can investigate the sign of μ for ^{31}S in the future experiment.

References

[1] T. Minamisono et al., Phys. Rev. C 14 (1976) 2335.
[2] T. Moriguchi et al., JPS Conf. Proc. 37 (2022) 021201.
[3] A. Ozawa et al., Prog. Theor. Exp. Phys. 2025 053D05.

2.5 Measurement of vicinage effects on convoy electron yield from carbon targets under OH^+ ion bombardment

Y. Yano, U. Ozeki, S. Ishii, K. Sasa, S. Tomita

Convoy electrons are forward-emitted electrons with velocities matching emerging projectiles from solid targets. Previous investigations using C_n^+ molecular ions demonstrated a substantial enhancement in convoy electron yield compared to the sum of that of constituent atomic ions [1,2]. This molecular effect, termed the vicinage effect [3], stems from the close distances and small relative velocities between the constituent atomic ions dissociated from the molecular ion within the solid target.

The prior studies focused only on homonuclear molecular ions. In these cases, the dissociated constituent atomic ions from molecular ions are identical, resulting in nearly equivalent velocities within the solid. On the other hand, vicinage effects in heteronuclear molecular ions remain less explored. For heteronuclear molecular ions, the relative velocities between the constituent atomic ions increase due to a difference in their stopping powers as the target thickness increases. Therefore, the investigation for heteronuclear ions will shed light on the importance of velocity matching between constituent ions.

In this study, we first examined the existence of the molecular effect in convoy electron yield for heteronuclear molecular ion OH^+. Experiments were conducted using the 1 MV Tandetron accelerator at UTTAC. OH^+, O^+, and H^+ ions were accelerated to 120 keV/u and directed onto carbon foil targets of 4.7 μg/cm². Convoy electrons were measured using an electrostatic energy analyzer positioned at 0° relative to the direction of the beam. Energy scans were performed with data acquisition normalized to integrated ion current at each energy step to compensate for beam intensity variations. Ion current normalization was performed using backscattering measurements with a thin Au target to account for charge-state-dependent variations in transmitted ion currents. The backscattered yield, which is directly proportional to incident particle flux via the Rutherford cross-section, provided accurate calibration of the incident particle flux. These normalization methods enabled us to compare the convoy electron yields of different ion species.

Figure 1 shows the electron energy spectra obtained for a 4.7 μg/cm² carbon foil under OH^+, O^+, and H^+ irradiation. The yields were normalized to the number of incident ion. The pronounced peaks near 60 eV, slightly lower than the energy of electrons matching the velocity of the incident ion, are attributed to convoy electrons. The energy shift is due to the energy loss of the incident ion as they pass through the carbon foil. Figure 1 reveals a significantly enhanced yield for OH^+ over O^+, that is larger than the H^+ yield. The convoy electron yield Y is obtained by integrating over the convoy electron peak, and the results are summarized in Table 1. The difference $Y(\mathrm{OH}^+) - Y(\mathrm{O}^+)$ is almost 6 times larger than $Y(\mathrm{H}^+)$, which could originate from the existence of an H^+ ion moving together with an O^+ ion.

The impurity of the $^{17}O^+$ ion in the OH^+ beam was monitored according to the ratio of the backscattering yield of O and H from a thin Au target measured on the same ion beam [4]. The obtained impurity of $^{17}O^+$ was 12.5% in the OH^+ ion beam. Assuming that the convoy electron yield of $^{17}O^+$ is the same as that of $^{16}O^+$, the existence of impurity of $^{17}O^+$ would give only 2.2% increase in convoy electron yield of OH^+ ions. Thus, the substantial enhancement of $Y(\mathrm{OH}^+)$ originates from the existence of an O^+ ion moving together with

a H^+ ion with a close distance and nearly the same velocity. Further systematic experiments are planned to explore this phenomenon.

Table 1. Convoy electron yields from a 4.7μg/cm^2 carbon foil under OH^+, O^+, and H^+ irradiation, and the difference between OH^+ and O^+ yields.

Projectile	$Y(OH^+)$	$Y(O^+)$	$Y(OH^+) - Y(O^+)$	$Y(H^+)$
Convoy electron yield (Arb. Units)	12.6 ± 0.20	10.4 ± 0.11	2.2 ± 0.23	0.365 ± 0.04

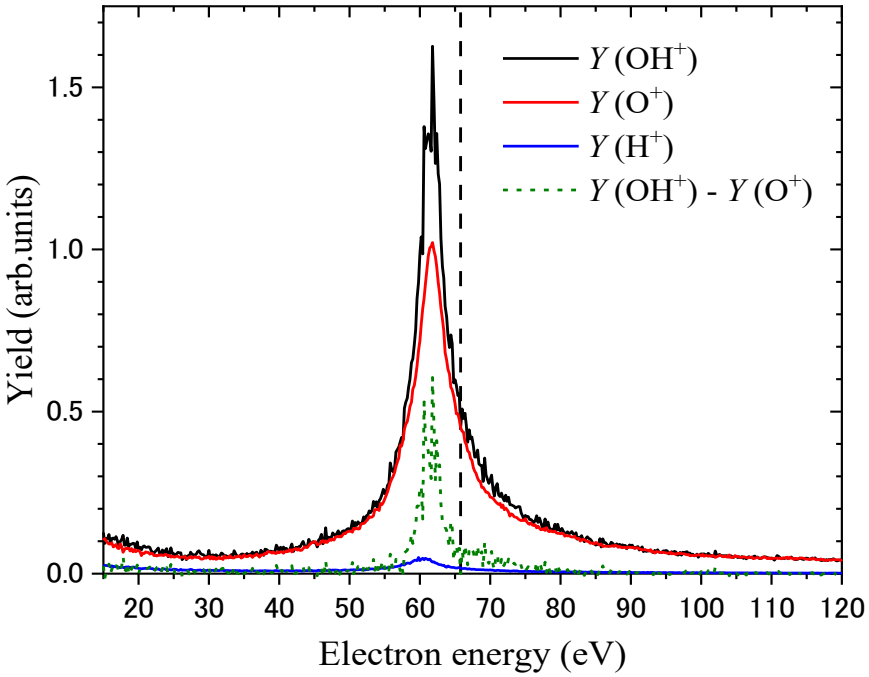

Fig. 1. Electron energy spectra obtained for a 4.7 μg/cm^2 carbon foil under 120 keV/u OH^+ (black line), O^+ (red line), and H^+ (blue line) irradiation, along with the difference between the OH^+ and O^+ spectra (green dotted line). The vertical dotted line indicates the energy of electrons matching the velocity of the incident ion. The pronounced peaks near 60 eV, slightly lower than the energy of electrons matching the velocity of the incident ion, are attributed to convoy electrons.

References

[1] S. Tomita et al., Phys. Rev. A 73 (2006) 060901.

[2] Y. Shiina et al., Phys. Rev. A 110 (2024) 062826.

[3] W. Brandt et al., Phys. Rev. Lett. 33 (1974) 1325.

[4] Y. Yano et al., UTTAC Annual Report 2023, UTTAC-93 (2024) 11.

3.

ACCELERATOR MASS SPECTROMETRY

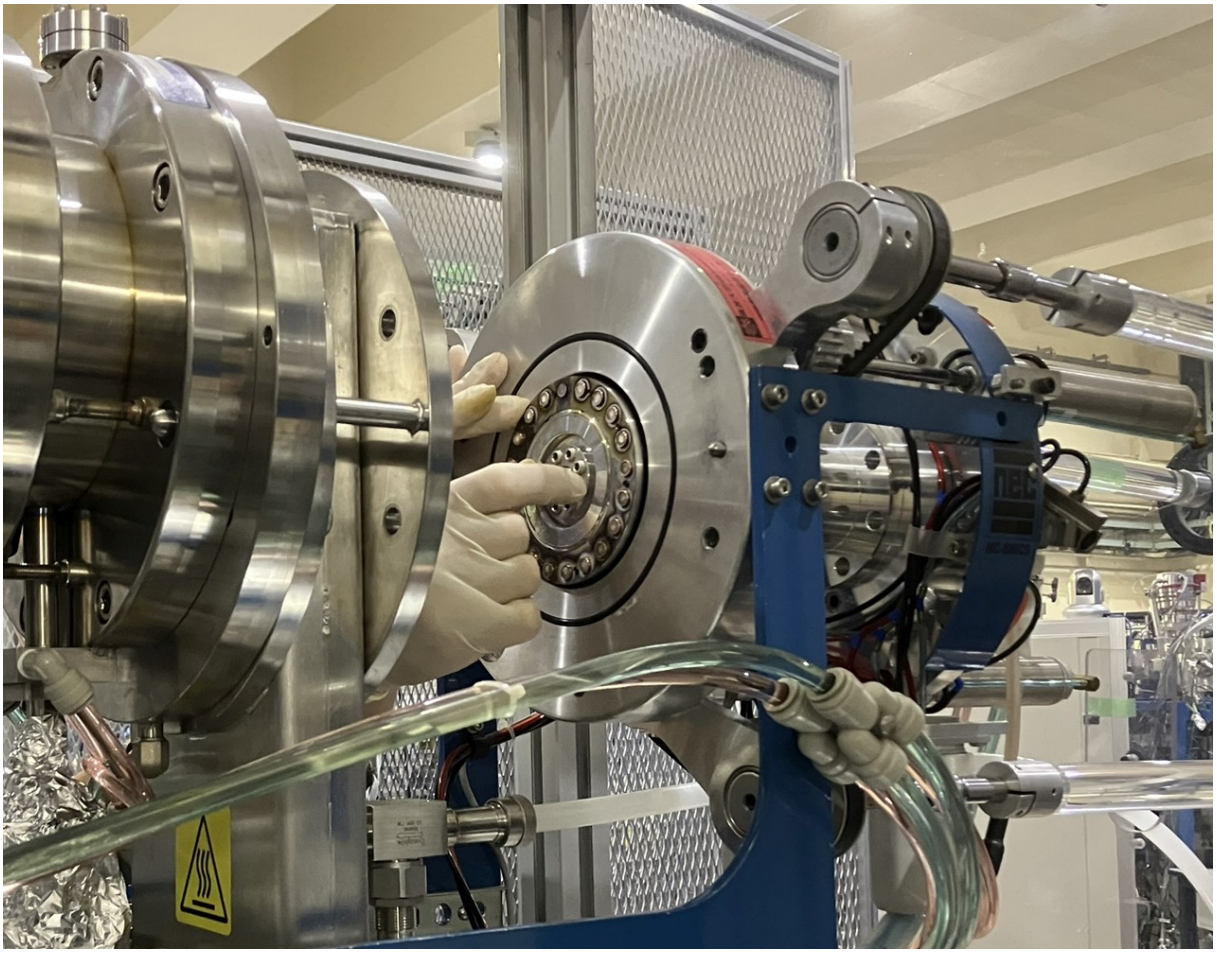

Setup of Samples for AMS Measurements

3.1 Status report of the Tsukuba 6 MV multi-nuclide AMS system in FY2024

K. Sasa, T. Takahashi, M. Matsumura, T. Yoshida, T. Kimura, M. Sakuma, H. Takami, M. Mikawa, T. Moriguchi, T. Matsunaka[1]

The Tsukuba 6 MV multi-nuclide AMS system was operated for a total of 58 days and 843.6 hours in FY2024. We conducted six research projects related to AMS. Figure 1 shows monthly-measured rare nuclides from April 2024 to March 2025. During this period, 713 samples were measured, mainly for ^{36}Cl and ^{129}I. In addition, test measurements of ^{10}Be and ^{14}C were performed for nuclear experiments [1]. Table 1 shows the breakdown of the measured samples. Table 2 shows the measurement status for each rare nuclide. Background isotope ratios ranged from 10^{-14} to 10^{-15}.

In FY2024, there was a problem with the cylinder of the sample rotation mechanism for the MC-SNICS ion source. Currently, the sample wheel can rotate in one direction only, but measurements are being performed. In addition, the beam intensity from the MC-SNICS ion source has been decreasing, and the cause is being investigated.

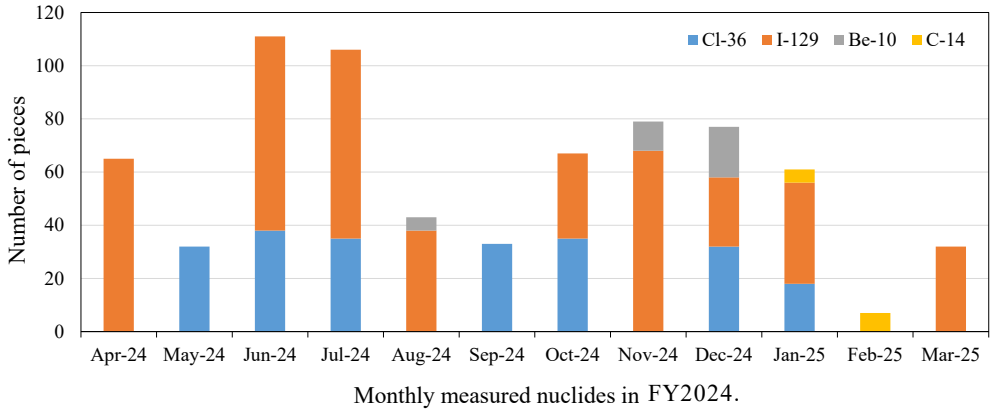

Fig. 1. Monthly-measured nuclides from April 2024 to March 2025.

Table 1. Number of measured samples in FY2024

Nuclides	Reagents & Blanks	Standard samples	Analyzed samples	Total
Be-10	17	14	4	35
C-14	2	10	0	12
Cl-36	66	72	85	223
I-129	58	50	335	443
Sub total	143	146	424	713

Table 2. Beam conditions for nuclides measured in FY2024

Nuclides	Terminal voltage [MV]	Accelerated ion	Total Energy [MeV]	Beam current (Low Energy side F.C.) [μA]	Transmission [%]	Measured/ Known [%]	BKG [atomic ratio]
Be-10	6.0	$^{10}Be^{3+}$	20.3	1.5 ~ 3	15 ~ 20	75	10^{-15}
C-14	5.0	$^{14}C^{4+}$	25.0	0.5 ~ 50	26 ~ 40	–	–
Cl-36	6.0	$^{36}Cl^{7+}$	48.0	~ 10	8 ~ 15	70	10^{-15}
I-129	5.0	$^{129}I^{5+}$	30.0	0.5 ~ 4	5 ~ 10	90 ~ 98	10^{-14}

[1]Kanazawa University

^{10}Be & ^{14}C-AMS

For experimental nuclear physics using beams of unstable nuclides, ^{10}Be and ^{14}C, an attempt has been made to increase the beam intensities using a standard sample of ^{14}C and a rainwater sample of ^{10}Be. ^{14}C with a 4+ charge state was accelerated to 25.0 MeV, as indicated in Table 2. For ^{10}Be AMS, $^{10}BeO^-$ was extracted from BeO samples and accelerated with a terminal voltage of 6.0 MV. $^{9}BeO^-$ beam currents were typically ≤3 μA, with a beam transmission of ~20%. Isobaric interference of ^{10}B was eliminated by the absorber cell in front of the detector allowing detection of 20.3 MeV $^{10}Be^{3+}$.

^{36}Cl-AMS

$^{36}Cl^{7+}$ was detected at 48 MeV in ^{36}Cl-AMS at a terminal voltage of 6.0 MV (Table 2). In FY2024, we conducted ^{36}Cl-AMS to investigate fluctuations in cosmic ray intensity, mainly in Antarctic ice cores [2]. In addition, we have conducted the international joint research project with Guangxi Normal University in China to measure anthropogenic ^{36}Cl in soil, and with KEK to measure ^{36}Cl in activated chloride sheathing covering cables in the large accelerator room [3]. We also conducted an experiment to estimate the accumulated thermal neutron dose using ^{36}Cl at the CHARM experimental facility at CERN.

^{129}I-AMS

^{129}I-AMS has been performed under the beam condition of $^{129}I^{5+}$ with 30.0 MeV at the terminal voltage of 5 MV (Table 2). In FY2024, we investigated interlaboratory comparative tests for NIST SRM (Standard Reference Material) 3228 and 3230, in which $^{129}I/^{127}I$ ranges from 10^{-14} to 10^{-11}. Detailed results can be found in Ref. [4]. ^{129}I-AMS was applied to ^{129}I tracer studies for surveys of the environmental dynamics of I-129 in the river water [5], the discharge of ALPS-treated water to the sea [6] at Fukushima, and so on.

Measurement history

Figure 2 shows the cumulative number of measured samples since the AMS system started operation. A total of 5,910 samples was measured from FY2016 to 2024.

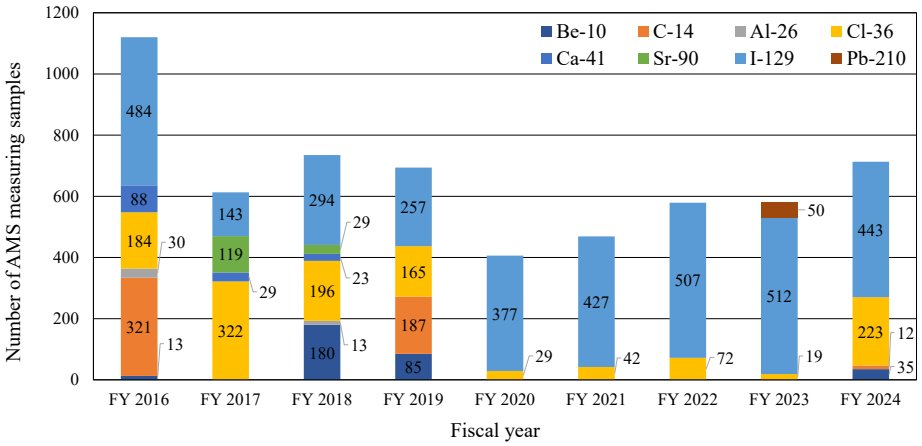

Fig. 2. Cumulative number of measured samples for AMS from FY2016 to 2024.

References

[1] M. Mikawa et al., this Annual Report 2.3.

[2] H. Takami et al., this Annual Report 3.4.

[3] T. Kimura et al., this Annual Report 3.3.

[4] M. Sakuma et al., this Annual Report 3.2.

[5] Y. Wakiyama et al., this Annual Report 3.7.

[6] H. Miura et al., this Annual Report 3.9.

3.2 Interlaboratory comparison of the NIST standards for ^{129}I using Accelerator Mass Spectrometry

M. Sakuma, M. Matsumura, T. Takahashi, T. Yoshida, K. Sasa

^{129}I is a long-lived radionuclide with a half-life time of approximately 15.7 million years and is used in studies such as dating marine sediments and assessing the effects of radioiodine in the environment. Accelerator Mass Spectrometry (AMS) is one of the detection methods for ^{129}I and measures the ratio of the amount of radioisotope ^{129}I to that of the stable isotope ^{127}I in a sample. In AMS, measured ratios are calibrated using valued standard samples. NIST (National Institute of Standards and Technology) is one of the organizations that produce and provide standard samples called SRM (Standard Reference Material). SRM validates its values through comparative verification at several measuring institutions.

In this study, at the request of NIST, we participated in the interlaboratory comparison of new SRMs for ^{129}I and measured the iodine isotopic ratio ^{129}I/^{127}I in the samples using AMS. Figure 1 shows the SRMs tested in this study. There were 5 types of SRMs to be measured, with 5 ^{129}I solution ampules per type, hence a total of 25 ampules were measured. The reference value of SRM's ^{129}I/^{127}I is $5.7 \times 10^{-14} \sim 5.7 \times 10^{-11}$. When preparing the sample, $AgNO_3$ was added to the ^{129}I solution to form AgI precipitates which were used as a target for AMS measurement. However, since the blank sample did not contain any iodine, stable iodine (Deepwater Chemicals, Inc.) was added for AgI preparation. ^{129}I/^{127}I of this stable iodine is about 1.5×10^{-14} [1]. In addition, standard samples prepared by Purdue University [2] were used to calibrate measured ^{129}I/^{127}I values.

Fig. 1. Standard Reference Material (SRM) for ^{129}I tested in this study at the request of NIST.

AMS measurement was performed by the 6 MV tandem accelerator at UTTAC. Table 1 shows ^{129}I/^{127}I measurement results of the SRMs tested in this study. Although the error range of measurement results is large for blank and stable iodine added to blank, the difference between them is small. For SRM 3230a Level B1 (^{129}I/^{127}I reference value: 5.7×10^{-13}), SRM 3228 Level A2 (^{129}I/^{127}I reference value: 5.7×10^{-12}), and SRM 3230a Level B2 (^{129}I/^{127}I reference value: 5.7×10^{-11}), the results are not inconsistent with the reference value. Regarding SRM 3228 Level A1 (^{129}I/^{127}I reference value: 5.7×10^{-14}), there is a difference by a factor of ~2 between the measured and the reference values. This difference is thought to be due to the difficulty in preparing samples with low ^{129}I/^{127}I and the limit of measurement sensitivity of AMS.

We compiled the results and submitted the report to NIST. The official value will be considered based on the reported results from the institutions participating in the interlaboratory comparison.

This work was supported by JSPS KAKENHI Grant Number 23K23269.

Table 1. $^{129}I/^{127}I$ measurement results of SRMs for ^{129}I in this study

SRM name	Reference $^{129}I/^{127}I$	Measured $^{129}I/^{127}I$
blank	-	$(3.55 \pm 0.23) \times 10^{-14}$
Stable iodine (added to blank)	1.5×10^{-14} [1]	$(2.54 \pm 0.38) \times 10^{-14}$
SRM 3228 Level A1	5.7×10^{-14}	$(10.22 \pm 0.41) \times 10^{-14}$
SRM 3230a Level B1	5.7×10^{-13}	$(5.79 \pm 0.10) \times 10^{-13}$
SRM 3228 Level A2	5.7×10^{-12}	$(5.08 \pm 0.05) \times 10^{-12}$
SRM 3230a Level B2	5.7×10^{-11}	$(5.08 \pm 0.10) \times 10^{-11}$

References

[1] H. Matsuzaki et al., Nucl. Instr. Meth. Phys. Res. B 361 (2015) 63.

[2] P. Sharma et al., Nucl. Instr. Meth. Phys. Res. B 123 (1997) 347.

3.3 Analysis of ^{36}Cl generated in power cable sheaths at a high energy accelerator facility

T. Kimura, G. Yoshida[1], H. Matsumura[1], M. Matsumura, T. Sanami[1], M. Ishida[1], E. Watanabe[1], K. Tsugane[1], E.J. Lee[1], R. Shiobara[2], M. Mitsuhashi[2], A. Toyoda[1], H. Yashima[3], Y. Hirano[2], Y. Nakayashiki[2], K. Oishi[2], S. Kurita[4], M. Nakada[4], T. Saze[4], B.N. Thien[5], T. Takahashi, T. Yoshida, K. Sasa

Particle accelerators are widely used in physics experiments, medical treatment, and industrial applications. However, a negative aspect associated with the accelerators is radioactivity resulting from nuclear reactions of not only accelerated particles, but also secondary particles (especially fast neutrons and thermal neutrons) with the beamline and shielding materials. Such radioactive nuclides eventually generate radioactive (activated) waste when the accelerator facility is decommissioned.

One of the large accelerators that has already been shut down is the 12GeV Proton Synchrotron (12GeV-PS) at the High Energy Accelerator Research Organization (KEK), where activation has been observed over a wide area of the accelerator tunnel. In particular, strong activation has been confirmed at the beam branching sections leading to the EP1 and EP2 beamlines [1]. Compared to concrete and electromagnets, power cables are small in volume and have not been targeted for activation surveys. Some power cable sheaths contain chlorine, and the stable isotope ^{35}Cl has a relatively large thermal neutron capture cross-section of 43.6 barn, which generates ^{36}Cl through the ^{35}Cl(n, γ)^{36}Cl reaction. ^{36}Cl is a long-lived radioactive nuclide with a half-life of about 3.01×10^5 years and remains for a long time. In addition, ^{36}Cl disintegrates mainly by β^- decay to ^{36}Ar (98.1%) without emitting gamma rays, making it difficult to evaluate the quantity. However, UTTAC has a lot of experience in measuring ^{36}Cl by accelerator mass spectrometry (AMS) using the 6MV tandem accelerator and, accordingly, this analysis technique is readily available for the present analysis of ^{36}Cl. Recently, we have sampled the power cable sheath from the 12GeV-PS and measured ^{36}Cl by AMS [2]. In this study, we attempted to quantify ^{36}Cl in the sheath of the power cable of the EP1 septum magnet, which is significantly activated within the 12GeV-PS.

The experimental procedures are outlined below. A power cable connected to the EP1 septum magnet in the 12 GeV-PS main ring was taken out and the sheath was stripped off to prepare a sample. First, in order to quantify the chlorine concentration in the cable sheath, we conducted fluorescence X-ray analysis using a handheld fluorescence X-ray analyzer and neutron activation analysis using the ^{37}Cl(n, γ)^{38}Cl reaction at the Kyoto University Research Reactor (KUR). Next, approximately 0.5 g of sheath was combusted in an argon/oxygen gas stream, and the generated gas was collected with water. The collected trapped water was analyzed by ion chromatography to confirm that sufficient Cl^- concentration was obtained. In addition, a chlorine carrier was added to the trapped water to dilute it to an isotope ratio suitable for AMS (^{36}Cl/^{nat}Cl ratio ~10^{-11}). Then, AgCl was purified by repeatedly performing chemical operations such as adding $AgNO_3$

[1]High Energy Accelerator Research Organization (KEK)
[2]Japan Environment Research Co., Ltd.
[3]Kyoto University
[4]National Institute for Fusion Science
[5]The Graduate University for Advanced Studies

to the trapped water, and the AgCl was used as a sample for AMS measurements. Three samples were prepared using the above steps from the EP1 cable sheath that we collected at the same point.

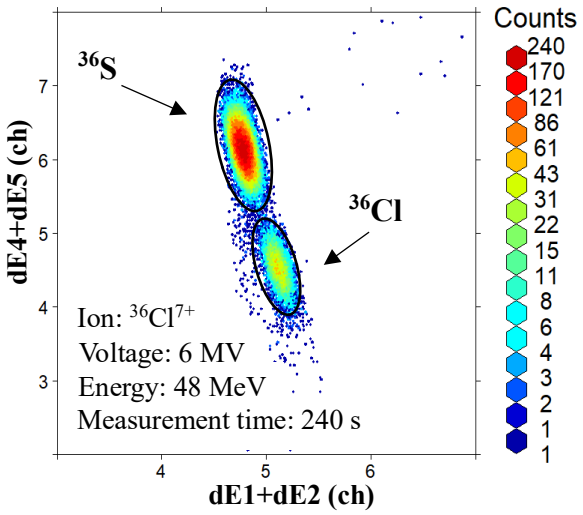

Fig. 1. AMS spectrum of a cable sheath (sample 1).

Table 1. Measurement conditions for AMS

Terminal voltage	6 MV
Stripper foil	4.8 μg cm^{-2} thick carbon
Detector entrance window	75 nm thick Si_3N_4
Detector gas	Isobutane 27 Torr
Measurement time	240 s

Table 2. Measured $^{36}Cl/^{35}Cl$ ratios of samples

Sample	$^{36}Cl/^{35}Cl$ ratio
1	$(6.65 \pm 0.21) \times 10^{-9}$
2	$(6.40 \pm 0.20) \times 10^{-9}$
3	$(6.20 \pm 0.20) \times 10^{-9}$

Figure 1 shows the AMS spectrum of the sample prepared by isotope dilution. The measurement conditions for AMS are shown in Table 1. Chlorine ions (Cl^-) were extracted from the AgCl sample, accelerated with an acceleration voltage of 6 MV by the AMS system at UTTAC, and Cl^{7+} at 48 MeV was detected in a gas ionization detector [3]. By using the gas ionization detector, the ^{36}S and ^{36}Cl signals were separated from each other based on the difference in energy loss. As shown in Fig. 1, the amount of ^{36}Cl in the cable sheath was quantified. The measured $^{36}Cl/^{35}Cl$ ratios of the samples are shown in Table 2. These results indicate that the sheath of the power cable connected to the EP1 septum magnet has a $^{36}Cl/^{35}Cl$ ratio of approximately 10^{-9} to 10^{-8}. Due to its extremely long half-life, ^{36}Cl has not been a primary focus in previous activation studies; however, this measurement suggests that its existence cannot be overlooked. In the future, it will be necessary to investigate all cables in the PS main ring.

References

[1] H. Kawamura et al., Japanese Society of Radiation Safety Management 22nd Annual Meeting in Shizuoka, 2A1-5, 2023.

[2] G. Yoshida et al., Japan Society of Nuclear and Radiochemical Sciences 68th Symposium, 1A10, 2024.

[3] K. Sasa et al., Nucl. Instr. Meth. Phys. Res. B 437 (2018) 98.

3.4 Search for cosmic ray events in 990BCE using the cosmogenic nuclide ^{36}Cl

H. Takami, K. Sasa, M. Matsumura, T. Yoshida, T. Takahashi, A. Matsuzaki[1], F. Miyake[1]

The incidence of large amounts of cosmic rays generated by astronomical events such as γ-ray bursts from outside the solar system and solar flares onto the Earth is collectively called a cosmic ray event. When cosmic rays enter the atmosphere, they induce a chain of nuclear reactions that produce radionuclides called cosmogenic nuclides, such as ^{10}Be, ^{14}C, and ^{36}Cl. The production rate of cosmogenic nuclides by cosmic-ray events depends on the type, energy, and intensity of the cosmic rays. By measuring the abundance ratio and concentration of cosmogenic nuclides in tree rings and ice core samples, we can confirm the trace and origin of cosmic-ray events. Traces of Solar Energetic Particle events (SEP events), which are thought to be caused by solar flares, have been discovered to occur in 774/775 AD and 993/994 AD by a research group at Nagoya University [1]. In addition, traces of cosmic ray events are predicted to exist in 990BCE based on ^{14}C analysis of tree rings [2].

In this study, ^{36}Cl isotope ratios in NDF2018 Antarctic ice core samples [3] corresponding to the 990BCE and surrounding ages were measured using the AMS instrument at UTTAC. We also analyzed the change of ^{36}Cl concentrations in the sample. The results are shown in Fig. 1. The peaks of ^{36}Cl concentration changes are seen around 1000 BCE and 987 BCE, but no peak is seen around 990 BCE.

In the ^{10}Be measurement of the same sample conducted by a research group at Nagoya University, a synchronized peak was observed around 1000 BCE. However, there was a shift in the peaks of each nuclide around 995 BCE and 987 BCE. The mean level of the variation pattern of ^{36}Cl/^{10}Be is 0.064 ± 0.028, which is lower than the theoretical value of 0.11 [3]. This may be due to the fact that the measured samples covered a short period of time, only about 30 years, and that the period with such low value was chosen unexpectedly.

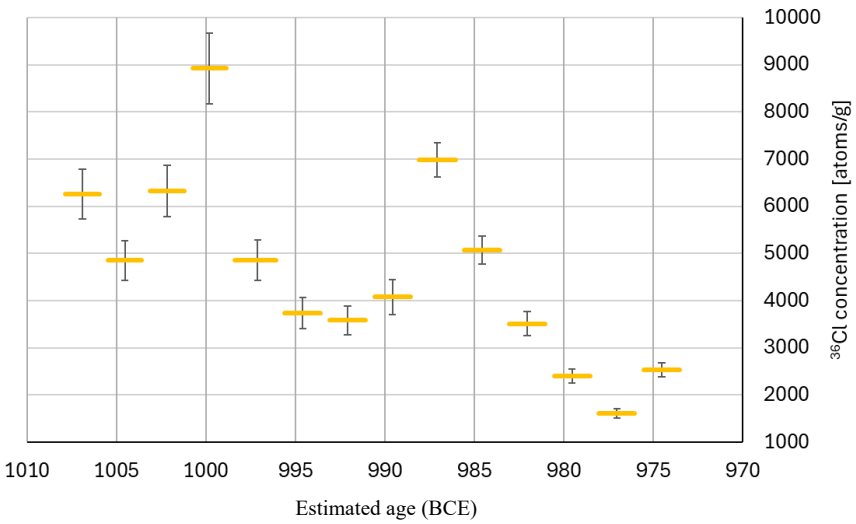

Fig. 1. ^{36}Cl concentration fluctuation of NDF2018 Antarctic ice core samples from 1007 BCE to 974 BCE.

The ^{36}Cl/^{10}Be value of the synchronized 1000 BCE peak is 0.134 ± 0.014, and the corresponding proton energy is 125 ± 15 MeV. Considering that the proton energies of SEP events range from a few MeV to 100 MeV, it is inferred that the peak of the estimated age 1000 BCE identified in this study is not from a large-

[1]Nagoya University

scale SEP event such as the 774/775 AD event. It is also possible that the synchronized peaks at ^{10}Be and ^{36}Cl of 1000 BCE are due to the same cause as the ^{14}C 990 BCE peak identified in the previous study, given that the error in the age estimate calculation for the NDF2018 Antarctic ice core sample is estimated to be ±10 years. A further detailed discussion of the peak and the estimated age discrepancy requires clarification of the accumulation rate from a geoscientific perspective.

References

[1] F. Miyake et al., 2013, Nat. Commun. 4, Article number: 1748.

[2] M. Sakamoto et al., Radiocarbon 66 (2024) 1992. [DOI: 10.1017/RDC.2023.50]

[3] https://cp.copernicus.org/articles/19/293/2023/

[4] J. Masarik and J. Beer, J. Geophys. Res. 104 (1999) 12099.

3.5 Performance of iodine-129 AMS measurements at University of Tsukuba (FY2024)

M. Matsumura, K. Sasa, T. Takahashi, T. Yoshida, T. Matsunaka[1]

The performance of ^{129}I measurements by accelerator mass spectrometry (^{129}I-AMS) has been reported since 2017 [1]. In FY2024, we have measured 443 samples prepared as AgI targets, which is 63% of all the measured AMS samples, The details are shown in Fig. 1 and described also in this annual report by K. Sasa et al. Figure 2 shows the measured blank values of AgI precipitated from carrier-reagent, called old iodine, and the ^{127}I beam current measured by the MFC02-2 Faraday cup before injection to the accelerator. The average of the ^{129}I/^{127}I ratios was $(3.0 \pm 1.3) \times 10^{-14}$ in FY2024. The average of ^{127}I beam current at the MFC02-2 cup was 3.2 μA in FY2016–2017 and decreased year by year. However, contrary to such a trend, it seems to have increased slightly to 1.5 μA in FY2024.

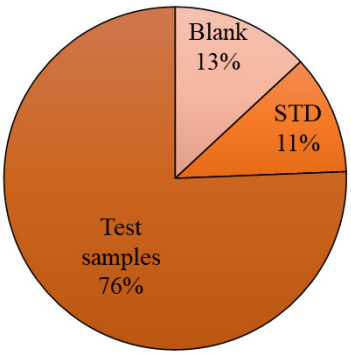

Fig. 1. Measured samples by ^{129}I AMS in FY2024.

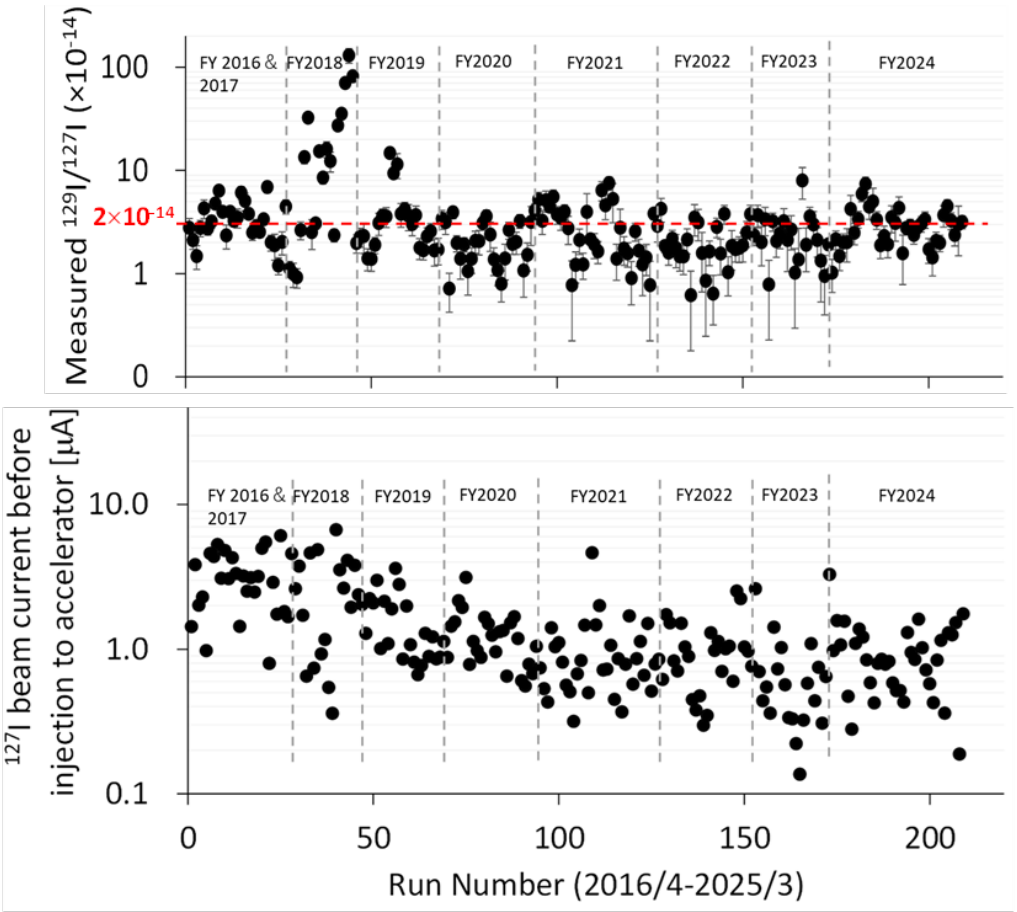

Fig. 2. Ratio of ^{129}I/^{127}I of old- iodine blank values and ^{127}I beam current, measured since FY2016.

[1]Kanazawa University

The measured $^{129}I/^{127}I$ values were normalized by using Standard Reference Material (SRM), Purdue-1 STD (Z94-0597) and Purdue-2 STD (Z94-0596) with an $^{129}I/^{127}I$ ratio of 8.378×10^{-12} and 6.540×10^{-11} [2] (the value was revised in 2014 [3]), which was provided by the Purdue Rare Isotope Measurement Laboratory (PRIME Lab) at Purdue University, USA. Figure 3 shows examples of STD measurements. In Purdue-1, target dependence occasionally appears in the measured values of the ^{129}I isotope ratio, but in Purdue-2, such dependence is almost absent, and stable measurement results were obtained. The averaged $^{129}I/^{127}I$ ratios with its standard deviation (1σ) are $(7.455 \pm 0.521) \times 10^{-12}$ (7.0%) and $(5.886 \pm 0.227) \times 10^{-11}$ (3.8%) for Purdue-1 (run number 436) and Purdue-2 (run number 294), respectively in FY2024. The ratios of the averaged $^{129}I/^{127}I$ ratio to the nominal ratio are 0.8898 ± 0.062 and 0.9000 ± 0.0346 for Purdue-1 and Purdue-2, respectively, which are in good agreement.

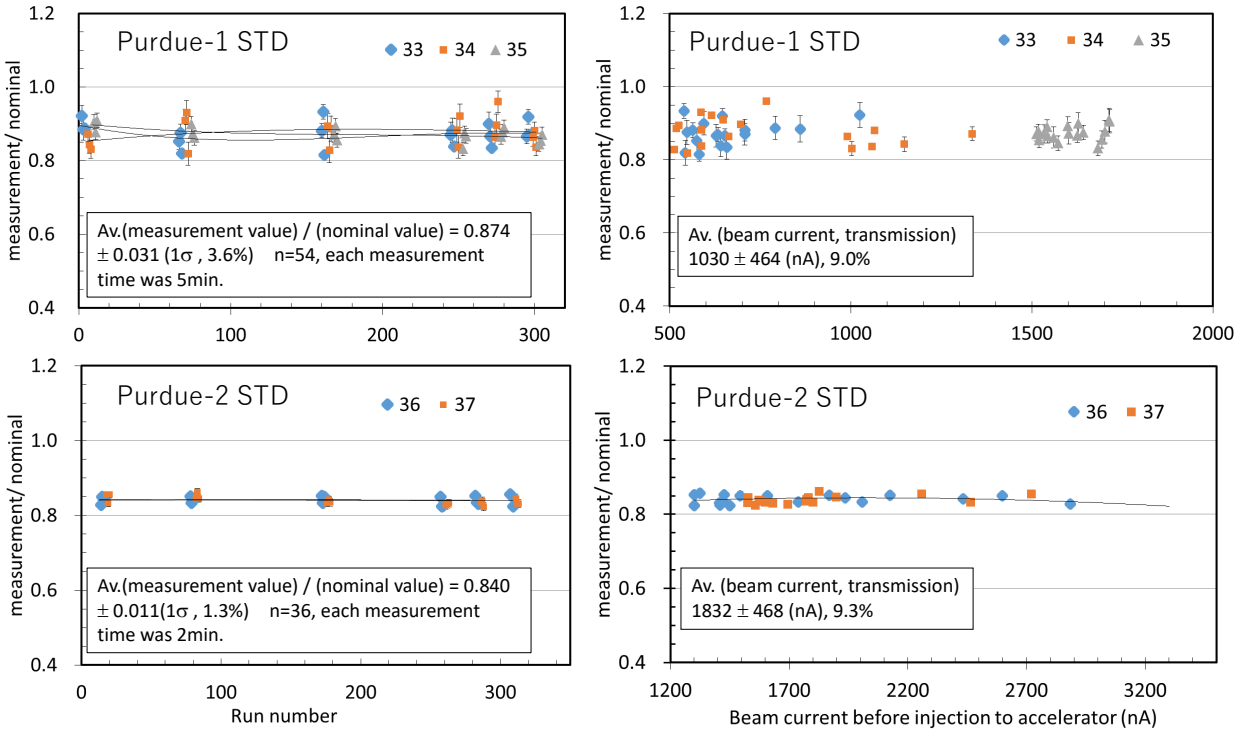

Fig. 3. Examples of STD-measurements performed on November 29, 2024. The targets numbers of AgI from 33 to 37 are indicated.

This work was supported in part by JSPS KAKENHI Grant Number 23K23269 and 24H02753.

References

[1] K. Sasa et al., UTTAC Annual Report 2017, UTTAC-87 (2018) 13.

[2] P. Sharma et al., Nucl. Instr. Meth. Phys. Res. B 123 (1997) 347.

[3] M. Caffee, (Purdue University), Private communication (2014).

3.6 Investigation of Iodine-129 fallout in rainwater in Japan

M. Matsumura, T. Matsunaka[1], T. Yoshida, T. Takahashi, Z. Shi, A. Sakaguchi, K. Sasa

Long-lived radioactive isotope ^{129}I (half-life 15.7 million years) exists in extremely trace amounts in the environment. Its natural sources include reactions between xenon in the upper atmosphere and cosmic rays, as well as spontaneous fission of ^{238}U in the Earth's crust. Anthropogenic sources include nuclear tests and nuclear-related activities. Research on ^{129}I is of social importance since ^{129}I is useful as an indicator of material cycles within the Earth, and also for environmental monitoring at nuclear facilities. Accumulating baseline data on ^{129}I concentrations and iodine isotope ratios in the environment, as well as measuring data at various locations, is of critical importance for geoscience in relation with environmental radioactivity. This study aimed to measure the concentration of ^{129}I falling with rainwater and survey the level of ^{129}I in domestic rainwater in order to accumulate basic data on ^{129}I fallout and support research on natural and anthropogenic hazards.

Rainwater was collected, with a focus on western Japan where there are few research examples, at Ehime University, Okayama University, Osaka University, Kanazawa University, Kyoto University, Tottori University, and Tokushima University, other than University of Tsukuba. The measurement over a month was carried out twice a year, in summer (August) and winter (February), using a special rainwater-collection device. The collected rainwater was filtered through a 0.45 μm membrane filter and then thoroughly mixed to become 150–200 mL volume, to which stable isotope iodine ^{127}I was added. The experimental procedure is similar to the previous case [1], except that we used a different carrier reagent ‘‘old Iodine’’ provided from Deepwater Chemicals, Inc., USA, with $^{129}I/^{127}I = 2 \times 10^{-14}$. After chemically separating the iodine, silver iodide was precipitated and dried, thereby ^{129}I was measured using AMS at UTTAC [2]. Approximately 5 mL of the remaining rainwater was sampled, and the ^{127}I concentration was determined by inductively coupled plasma mass spectrometry (ICP-MS). The iodine isotope ratio ^{129}I /^{127}I, ^{129}I concentration, and deposition amount were then determined. The results are presented in Table 1; A slightly higher trend is observed in winter than in summer. These results reproduce previous ones obtained from Tsukuba City rainwater [3].

Table 1. ^{129}I and ^{127}I concentrations in rainwater FY2024

	^{127}I concentration (ppb)	^{129}I concentration ($\times 10^7$ atoms L^{-1})	$^{129}I/^{127}I$ ($\times 10^{-9}$)
Aug. 2024	1.4 ± 0.4	2.4 ± 0.8	3.9 ± 1.4
Feb. 2025	3.0 ± 0.5	12 ± 6.4	8.6 ± 4.8
Average	2.2 ± 1.0	7.3 ± 6.7	6.3 ± 4.1

[1]Kanazawa University

Acknowledgments: We would like to express our gratitude for their cooperation in collecting rainwater samples, Assistant Professor T. Iwasaki (Ehime University), Associate professor T. Hanafusa and Dr. T. Nagamatsu (Okayama University), Assistant professor M. Kita (Tottori University), Professor M. Sakama (Tokushima University), Professor T. Yoshimura (Osaka University), Professor Y. Matsushi and A. Morikawa (Kyoto University). This work was supported in part by JSPS KAKENHI Grant Number 23K23269 and 24H02753.

References

[1] M. Matsumura et al., Anal. Sci. 36 (2020) 631.
[2] K. Sasa et al., Nucl. Instrum. Meth. Phys. Res. B 437 (2018) 98.
[3] M. Matsumura et al., Geochem. J. 52 (2018) 155.

3.7 Riverine ^{129}I dynamics during high-flow events in the Niida river

Y. Wakiyama[1], M. Matsumura, T. Matsunaka[2], S. Hirao[1], K. Sasa

The long-lived ^{129}I (half-life: 15.7 million years) is one of radionuclides of interest released from the Fukushima Daiichi Nuclear Power Plant (FDNPP). ^{129}I is of interest in relation to the ALPS treated water release which started from August 2023 as substantial amount of ^{129}I remained in wastewater drained from the damaged power plant. The situation underlines the importance of quantitative information of ^{129}I discharge from terrestrial for understanding impacts of the ALPS treated water release. On the motivation described above, we continued analyses of ^{129}I in river waters collected from the Niida river in collaboration of Environmental Radioactivity Research Network Center (ERAN) program.

Samples were collected at the Haramachi site (206 km^2 of catchment area and 853 kBq/m^2 of catchment mean ^{137}Cs inventory) and at the Warabidaira site (29 km^2 and 1420 kBq/m^2) along the Niida river during high-flow events on August 2016 and October 2017. All river water samples were filtered with 0.45 μm membrane filter and obtained samples of suspended solids (SS) and filtrates were subject to pretreatment, ^{129}I/^{127}I ratio measurement by accelerator mass spectrometry, and ^{127}I concentration measurement by ICP-QQQ-MS by following Muramatsu et al. [1]. Data of ^{129}I were compared with those of ^{137}Cs.

Table 1 shows updated results of ^{129}I analyses. Mean values of ^{129}I concentrations and ^{129}I/^{127}I ratios are higher at the Warabidaira than the Haramachi, reflecting presumably difference in ^{129}I inventory in the catchments. There is no clear dependence of the concentrations and ratios on magnitude of high-flow event. Mean values of dissolved ^{129}I concentration are lower than those in Ueda et al. [2], presenting 0.44 μBq/L at the site close to Haramachi and 0.69 μBq/L at the site close to Warabidaira. One possible explanation is a dilution-like effect during the high-flow events observed in this study. Dissolved ^{129}I concentration is positively correlated with dissolved ^{137}Cs concentration, suggesting similar behavior of those two nuclides during high-flow events.

Table 1. Summary of results of ^{129}I analyses

Site (river name)	Sample collection period	Number of samples	Mean dissolved ^{129}I conc.	Mean ^{129}I conc. in SS	Mean distribution coefficient	Mean ^{129}I/^{127}I in water	Mean ^{129}I/^{127}I in SS
			(μBq/L)	(mBq/kg)	(L/kg)	(10^{-9})	(10^{-9})
Haramachi	16-17 Aug. 2016	5*	0.174	4.07	22500	5.53	27.6
	22-23 Oct. 2017	6	0.129	2.36	22200	4.92	31.3
Warabidaira	16-17 Aug. 2016	5	0.236	11.2	56100	10.4	48.5
	22-23 Oct. 2017	6	0.274	5.16	21600	13.6	37.0

* Number of samples for Mean ^{129}I conc.in SS, Mean distribution coefficient, and Mean ^{129}I/^{127}I in SS are four.

References

[1] Y. Muramatsu et al., J. Environ. Radioact. 139 (2015) 344.

[2] S. Ueda et al., J. Environ, Radioact. 282 (2025) 107617.

[1]Fukushima University
[2]Kanazawa University

3.8 Limit of quantitation of I-129 in Southern Ocean seawater using the UTTAC AMS System

T. Matsunaka[1], Y. Kumamoto[2], M. Matsumura, T. Takahashi, A. Sakaguchi, K. Sasa

The Antarctic Circumpolar Current (ACC) connects the Atlantic, Indian, and Pacific Oceans and is shifting southward due to strengthening westerly winds caused by global warming. This shift moves the upwelling zone of warm Circumpolar Deep Water (CDW) southward, contributing to Antarctic sea ice melt and further warming. Iodine-129 (I-129), with a half-life of 15.7 million years, originates mainly from nuclear activities. In the Southern Hemisphere, its main source is Pacific nuclear bomb testing. I-129 levels in the Southern Ocean (Pacific side) are 2–5 orders of magnitude lower than in the Northern Hemisphere, yet still above pre-nuclear levels [1]. This makes the Southern Ocean ideal for tracing anthropogenic I-129. While previous I-129 studies traced CDW in the Pacific sector [2], none have been conducted in the Indian sector. Understanding the southward shift of CDW is crucial. This study aims to determine quantitation limit of seawater I-129 by UTTAC AMS, while clarifying seawater circulation in the Indian sector of the Southern Ocean through vertical profiles of dissolved I-129 and water mass analysis.

Seawater samples were collected both vertically and horizontally at six stations in the Southern and Indian Oceans (maximum sampling depth: 5,230 m) during the JAMSTEC MR19-04 cruise (December 2019 – February 2020), and horizontally at 15 stations along a transect from Australia to Syowa Station, Antarctica, during the National Institute of Polar Research (NIPR) SR21 expedition (November 2021 – March 2022). Each 500 mL seawater aliquot was spiked with 1 mg of I-127 carrier (Deepwater iodine, I-129/I-127 = 1×10^{-14}), followed by iodine extraction and purification via solvent extraction. The extracted iodine was precipitated as silver iodide (AgI) and pressed into targets for accelerator mass spectrometry (AMS) analysis. The I-129/I-127 isotopic ratios were determined using the AMS system at UTTAC, with normalization to the S-Purdue standard material (Purdue University, I-129/I-127 = 8.378×10^{-12}). The AMS measurements were performed using a terminal voltage of 5 MV and a charge state of 5+. The I-127 concentrations in seawater were quantitated separately using inductively coupled plasma mass spectrometry (ICP-MS). Final I-129 concentrations were calculated from the measured I-129/I-127 ratios and corresponding I-127 concentrations.

The isotope ratio of the process blank was 2.19×10^{-14} for an average of 10 data points, with a standard deviation of 0.55×10^{-14} (Fig.1). The count rate was 0.5 counts min^{-1}. Based on this standard deviation, we determined that the detection limit for seawater is 1.16×10^{-14} and the quantitation limit is 7.78×10^{-14}. Also, since these values are isotope ratios with carrier added, the limit of quantitation of I-129 in seawater is 2.87×10^{5} atoms L^{-1}, which is equivalent to the pre-nuclear level (3.0×10^{5} atoms L^{-1}), when calculated based on the analytical conditions of seawater. In the Southern Hemisphere Indian Ocean, I-129 levels range from 10^{5} to 10^{7} atoms L^{-1}, similar to or lower than North Pacific levels. In the Southern Ocean, I-129 is below 3×10^{5} atoms L^{-1}. Figure 2 shows that water temperature, salinity, and I-129 decrease with latitude, with I-

[1]Kanazawa University
[2]JAMSTEC

129 below pre-nuclear levels in surface waters. I-129 correlates positively with temperature and salinity, reflecting mixing of water masses and tracing anthropogenic I-129 and polar fronts. Ra-228 (half-life 5.27 years) and Ra-226 (1600 years) come from Th-232 and U-238 and indicate continental shelf water. Ra-226 is a better deep-water tracer and was higher in the Southern Ocean, suggesting active vertical mixing. I-129 and Ra-226 are negatively correlated. The ACC contributes 80–100% of Southern Ocean surface water [3], explaining the low I-129 due to deep water influence. Future work will analyze the relationship between anthropogenic I-129-bearing water masses and Circumpolar Deep Water (CDW) in the Southern Ocean using vertical profiles of I-129.

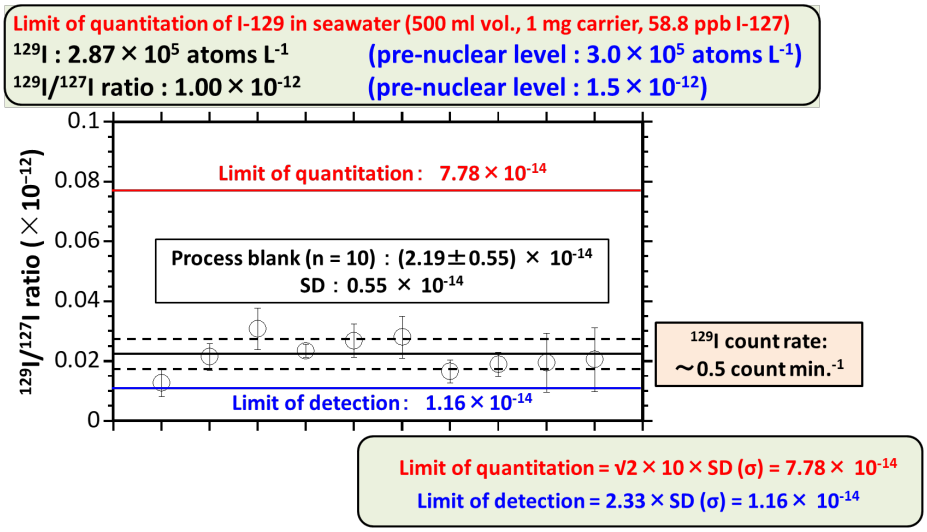

Fig. 1. Limit of quantitation of I-129 in the seawater.

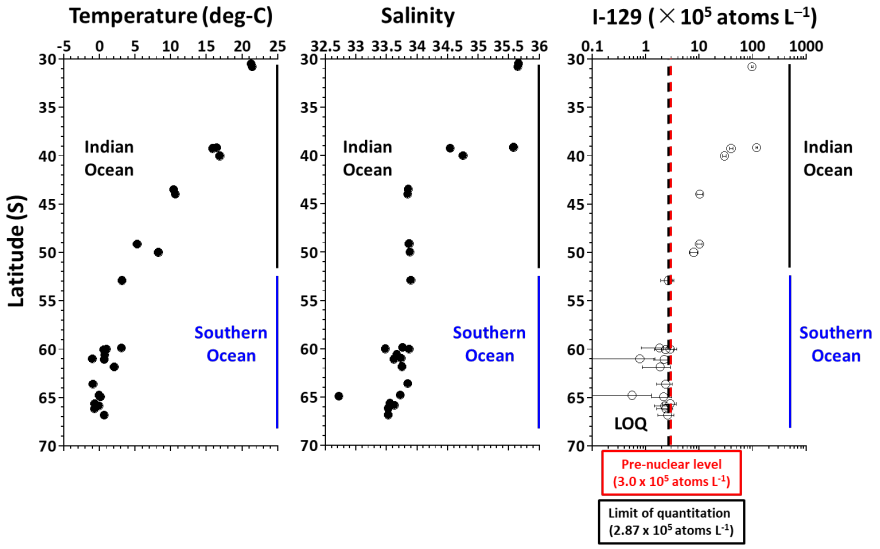

Fig. 2. Latitudinal surface distribution of I-129 in the Indian and Southern Oceans.

References

[1] S. Xing et al., Sci. Rep. 7 (2017) 7726.

[2] S. Xing et al., J. Environ. Radioact. 225 (2020) 106424.

[3] M. Inoue et al., Sci. Rep. 12 (2022) 1781.

3.9 Changes in iodine-129 concentrations in seawater near the Fukushima Dai-ichi Nuclear Power Plant due to the discharge of ALPS treated water

H. Miura[1], T. Matsunaka[2], K. Sasa, T. Takahashi, M. Matsumura, T. Yoshida

Anthropogenic ^{129}I has been released into the ocean as a result of nuclear weapons testing, nuclear fuel reprocessing, and nuclear accidents, including the Fukushima Dai-ichi Nuclear Power Plant (FDNPP) accident. Since August 2023, Tokyo Electric Power Company has been discharging water treated by the Advanced Liquid Processing System (ALPS-treated water), which contains trace amounts of ^{129}I, into the ocean. This study aims to investigate the distribution of ^{129}I in seawater using Accelerator Mass Spectrometry (AMS), in order to support model-based estimations of ^{129}I concentrations for radiation dose assessments.

Surface seawater samples were obtained near the FDNPP using a fishing vessel. Iodine was extracted and purified at the Low Level Radioactivity Laboratory, Kanazawa University. The ^{129}I /^{127}I ratio was measured using AMS at the University of Tsukuba, with a terminal voltage of 5 MV and a charge state of 5+ [1]. The measured ratio was normalized against the Purdue-1 standard reference material (^{129}I /$^{127}I = 8.378 \times 10^{-12}$), obtained from Purdue University. The concentration of ^{127}I in alkaline solution was determined using Inductively Coupled Plasma Mass Spectrometry (ICP-MS). The ^{129}I /^{127}I ratio from AMS and the ^{127}I concentration from ICP-MS were used to calculate the ^{129}I concentration in seawater.

Before the release of the ALPS-treated water, ^{129}I concentrations at the sites more than 2 km away from the FDNPP had decreased to levels comparable to those before the FDNPP accident (on the order of 10^{-8} Bq/L). On the other hand, within a 2 km radius of the FDNPP (Fig. 1), concentrations on the order of 10^{-7} to 10^{-6} Bq/L were observed, suggesting that leakage of water containing radioactive nuclides from the FDNPP or its vicinity has been continuing.

During the ALPS-treated water discharge on October 11, 2023, samples collected within the 2 km radius showed variations in concentration depending on the location, with particularly high concentrations observed at sites to the south (a in Fig. 2). Furthermore, samples collected four days after the discharge was completed on October 27, 2023, showed high concentrations at all sites (b in Fig. 2). As these observed concentrations are difficult to explain based on monitoring results alone, an ocean dispersion simulation of ^{129}I was conducted, leading to the following findings:

(1) On October 11, 2023, seawater originating from the ALPS-treated water flowed southward.

(2) On October 27, 2023, seawater derived from the ALPS-treated water remained near the FDNPP.

These results were consistent with monitoring trends, and the concentration levels predicted by the simulation were generally in agreement with the monitoring data. It was shown that the distribution of ^{129}I concentrations near the plant can be reasonably reproduced by the simulation.

No clear increase in concentration was observed when comparing the data before and after the start of the discharge, and the monitoring results indicate that it is difficult to quantitatively assess the impact of the

[1]Central Research Institute of Electric Power Industry
[2]Kanazawa University

ALPS-treated water release. In addition, the continuous leakage of radioactive nuclides from within or near the FDNPP may have a non-negligible impact compared to the ALPS-treated water release, highlighting the need to identify the amount and source of leakage. Future work will include speciation analysis of ^{129}I (inorganic and organic forms) and discussion in combination with other isotopes (e.g., ^{137}Cs, ^{3}H).

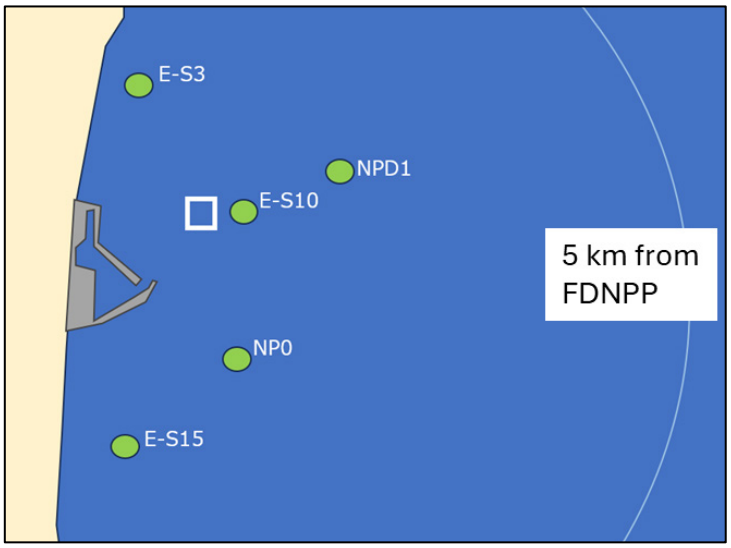

Fig. 1. Sampling sites within 2 km from the FDNPP are shown on the map.

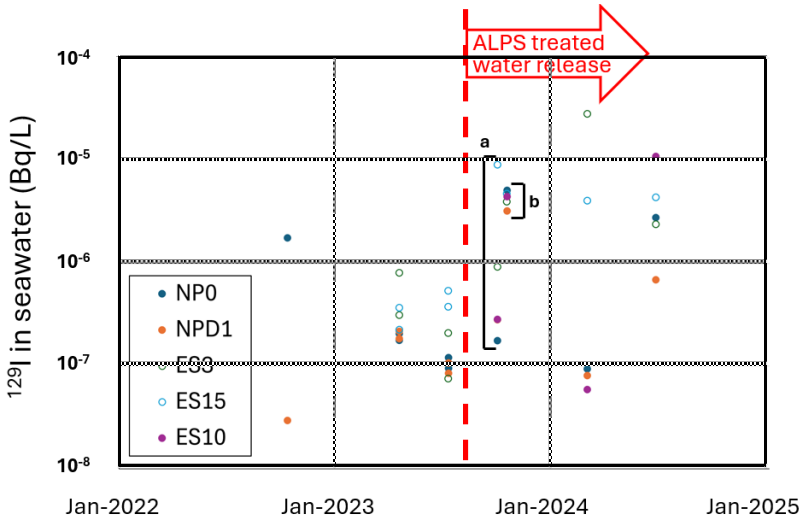

Fig. 2. The ^{129}I concentration in seawater in the sites within 2 km from the FDNPP.

Reference

[1] K. Sasa et al., Nucl. Instr. Meth. Phys. Res. B 437 (2018) 98.

4.

MATERIALS RESEARCH

Tandem Control Area Captured by a Fixed-Position Camera

4.1 D/H characterization of materials by T-ERDA

H. Kudo, H. Naramoto, M. Sataka. S. Ishii, K. Sasa, S. Tomita

Recoil detection analysis of transmission type (T-ERDA) at 0° is useful for unique characterization of materials. Indeed, this method allows non-destructive determination of the ratio of D to H concentration (so-called D/H ratio) [1]. Technically, the notable advantage of this method is that the 0° layout rigorously satisfies the requirement that the beam axis and the detector's center axis intersect at the surface of a thin sample even when the sample is tilted or moved back and forth. Furthermore, this method is insensitive to fluctuations in the incident beam current since the D/H ratio is determined from the peak yields on the same spectrum that is accumulated by pulse-height analysis.

The D/H ratio affects properties of industrial materials, for example, the C-D chemical bond in a typical resin is more stable than the C–H bond against irradiation of energetic charged particles [1,2]. While the D/H ratio is approximately equal to 10^{-4} wherever hydrogen is found on the earth, change in the D/H ratio is expected to occur in H-containing materials that are chemically synthesized. At present, it is unclear in what range the actual D/H ratio lies, hence collecting reference data for industrial materials is needed for wide use of T-ERDA. In this study, the D/H ratio of Kapton was investigated.

Figure 1 shows the H peak measured four times at a fixed He^{2+} beam spot on the Kapton film of 7.5 μm thickness. If a semiconductor detector is used instead of the pin-photo detector, the spectrum will have a rectangular shape with its width shown by the red arrow in Fig. 1, which is given by SRIM calculations [3]. The relatively low energy resolution is not serious in in the present analysis of the areas of H and D peaks to determine the D/H ratio. Unlike the previous case of mylar and PPS [1], there is no discernable irradiation-induced H loss under the low beam-dose conditions up to 2×10^{14} He^{2+}/cm^2. Similar behavior was seen for 8.0 MeV He^{2+}. Considering the measurement error of the incident He^{2+} charge, the H concentration obtained from the H peak area agrees with the calculated one from the atomic component and the density (1.42 g/cc) of Kapton, i.e., 2.24×10^{22} $/cm^3$.

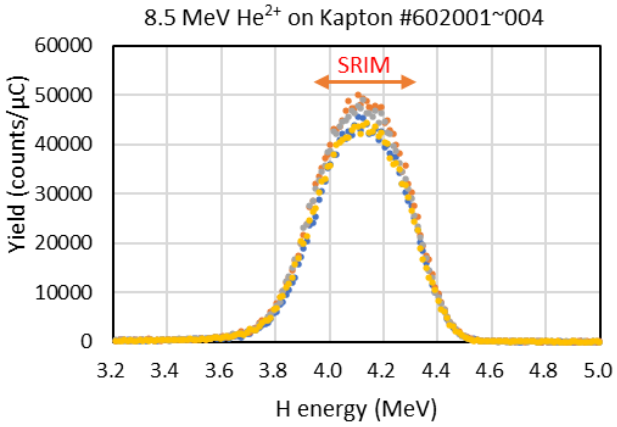

Fig. 1. Recoil H spectra from Kapton, measured by 0-degree T-ERDA using an 8.5 MeV He^{2+} beam.

Figures 2 and 3 show D peaks obtained by using the beams of 8.5 and 8.0 MeV He^{2+}, respectively, together with the calculated D-peak ranges by SRIM. The D peak for 8.5 MeV He^{2+} is not clearly recognized possibly due to the nuclear reaction yield overlapped on the low-energy side, in contrast to the well-distinguished D peak for 8.0 MeV He^{2+}. The D/H ratios have been determined from the integral of the yield in Figs. 2 and 3 in the range indicated by red arrows (SRIM values). The detailed procedure to determine the D/H ratio is described elsewhere [1]. The uncertainty in the determined D/H ratios of Kapton originates mainly from the statistical errors of the D yield.

The results obtained are shown in Table 1, together with the D/H ratios of Mylar, PPS, and seawater. The D/H values obtained for Kapton are about five times the average value of 1.55×10^{-4} for seawater, and about seven times the values determined previously for Mylar and PPS. It is speculated that such a significant enrichment of deuterium occurred during the synthesizing process of Kapton.

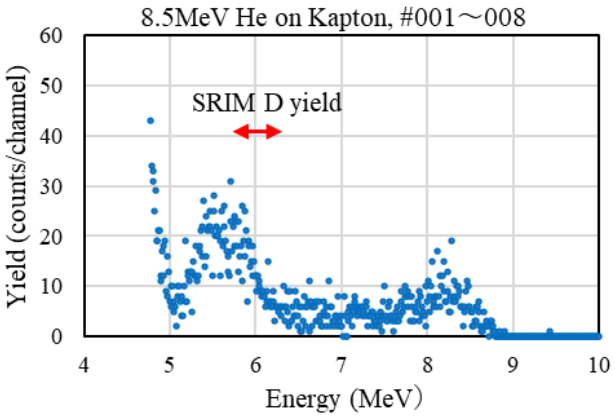

Fig. 2. Recoil D spectrum from Kapton, measured by 0-degree T-ERDA using 8.5 MeV He^{2+}.

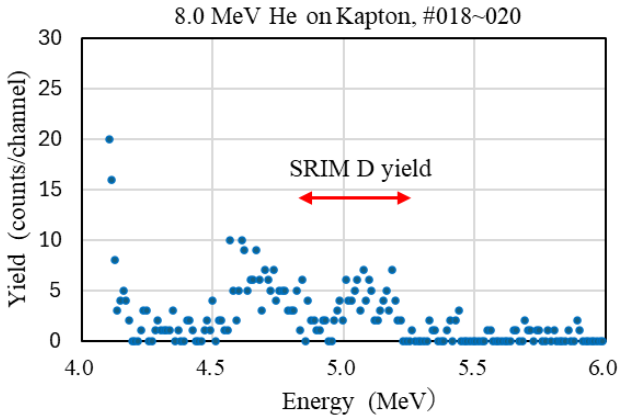

Fig. 3. Recoil D spectrum from Kapton, measured by 0-degree T-ERDA using 8.0 MeV He^{2+}.

Table 1. Determined D/H ratios and the D/H value of Standard Mean Ocean Water (V-SMOW)

Sample	Incident He^{2+} energy	D/H ratio	Comment
Kapton	8.5 MeV	$(7.5\pm0.03)\times10^{-4}$	This work
Kapton	8.0 MeV	$(8.3\pm0.07)\times10^{-4}$	This work
Mylar	8.02 MeV	$(1.09\pm0.08)\times10^{-4}$	Previous work (NIMB-2024)
PPS	8.02 MeV	$(1.25\pm0.08)\times10^{-4}$	Previous work (NIMB-2024)
Seawater	———	$(1.5576\pm0.0010)\times10^{-4}$	V-SMOW [4]

The present work is summarized as follows:

(1) Kapton is suitable as a calibration standard for hydrogen quantification of thin films by T-ERDA.

(2) The D/H ratio of Kapton is 5 times higher than that of seawater and 7 times higher than that of Mylar and PPS, indicating significant concentration of D in the synthesizing process.

(3) It has been demonstrated that T-ERDA can be successfully applied to non-destructive D/H characterization of not only natural, but also industrial materials.

References

[1] H. Kudo et al., Nucl. Instr. Meth. Phys. Res. B 554 (2024) 165404.

[2] F. Abel et al., Nucl. Instr. Meth. Phys. Res. B 266 (1995) 86.

[3] J. F. Ziegler, J. P. Biersack, SRIM2013, The Stopping and Range of Ions in Matter, http://www.srim.org/.

[4] J. C. De Wit et al., Geostand. Geoanal. Res. 4 (1980) 33.

4.2 Characterization of thin HfO_2 films using positron annihilation spectroscopy

A. Uedono, Kawakami, T. Kuribara, R. Hasunuma, Y. Harashima[1], Y. Shigeta, Z. Ni[2], Y. Ruolin[3], H. Nakamura[3], A. Notake[4], T. Moriya[5], K. Michishio[6], S. Ishibashi[6]

A thin layer of HfO_2 deposited using atomic layer deposition (ALD) often appears in an amorphous state, and it tends to crystallize during the post-deposition process. HfO_2 is polymorphous and has phases such as cubic, monoclinic, tetragonal, and orthorhombic crystal systems. Its dielectric constant (k) varies depending on these crystalline phases (20–40) [1]. Thus, controlling the crystalline phases of HfO_2-based dielectrics is a key factor in device fabrication because the polycrystalline state can lead to fluctuations in k values. Intrinsic point defects are expected to play a crucial role in the transition from the amorphous to the crystalline phase of HfO_2 and in the mechanism of current leakage. In this study, we utilized monoenergetic positron beams to investigate the vacancies in thin HfO_2 films.

When a positron is implanted into solids, it annihilates with an electron and emits γ quanta. The momentum component of the annihilating electron-positron pair broadens the energy distribution of the γ rays. A positron can be trapped by a vacancy due to Coulomb repulsion from the ion cores (Fig. 1). Since the momentum distribution of electrons in the defects differs from that of electrons in the bulk, the defects can be detected by measuring the Doppler broadening spectra of the annihilation radiation. The change in the spectra due to positron trapping is shown in Fig. 1. Due to the low electron density in vacancies, the lifetime of positrons increases when they are trapped in vacancies.

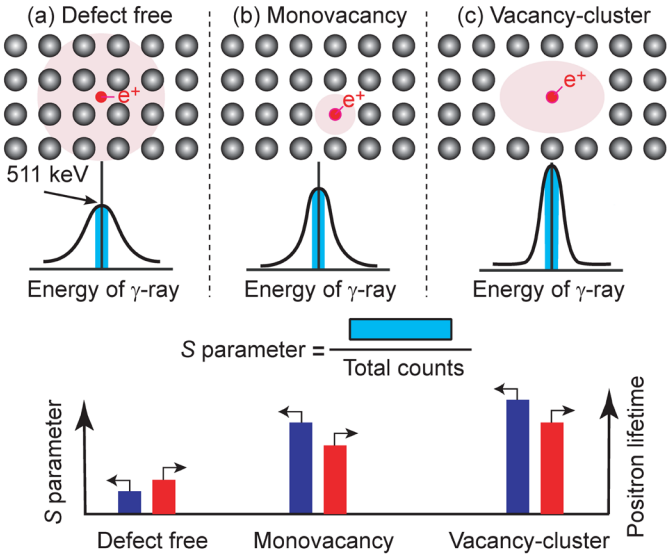

Fig. 1. Schematic drawing of Doppler broadening spectra for annihilation of positrons (a) in delocalized state, (b) trapped by monovacancy, and (c) trapped by vacancy cluster. The spectra are characterized by S parameter. Positron lifetime and S are increased by trapping of positrons by vacancies.

A 20-nm-thick TiN layer was deposited on a Si substrate by ALD using $TiCl_4$ and NH_3 as precursors. HfO_2 layers with thicknesses of 4–30 nm were deposited on TiN/Si by ALD using organic Hf precursor. Vacancy-type defects in the HfO_2 layers were probed using monogenetic positron beams. Details on this technique are

[1]Nara Institute of Science and Technology
[2]S-Technology Development Center, TEL Solutions Ltd.
[3]Development Department 1, TEL Solutions Ltd.
[4]Digital Design Center, TEL Ltd.
[5]Software and Data Engineering Division, TEL Technology Solutions Ltd.
[6]AIST

given elsewhere [2]. The Doppler broadening spectra of the annihilation radiation were measured by hyper-pure Ge detectors, and they were evaluated using the *S* parameter. The positron lifetimes for the HfO_2 layers were also measured using a pulsed monoenergetic positron beamline [3].

Figure 2 shows the *S* values as a function of incident positron energy *E* for HfO_2/TiN/Si. The value of *S* at *E*=1–1.5 keV can be associated with the annihilation of positrons in the HfO_2 layer. The *S* values for the HfO_2 layer increase as the HfO_2 thickness decrease, suggesting that the size of vacancies increases as the film thickness increases. The lifetime spectra of positrons were measured, and by comparing the obtained positron lifetimes with computer simulations, the defect species were identified. The major vacancy-type defects were identified as a Hf vacancy (V_{Hf}) coupled with multiple oxygen vacancies (V_{OS}) and larger vacancy clusters, where the number of V_{OS} coupled with V_{Hf} increases as the HfO_2 thickness decreases.

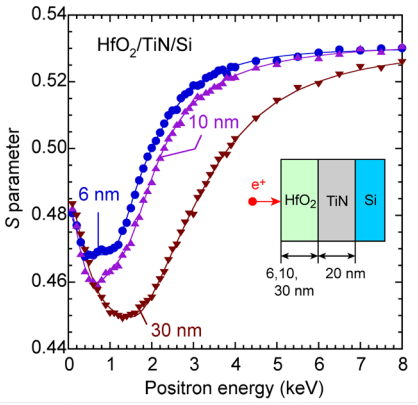

Fig. 2. *S*–*E* plots for HfO_2(6, 10, and 30 nm)/TiN/Si. The *S* value at *E*=1–1.5 keV is attributed to the annihilation of positrons in HfO_2 films. The inset shows the sample structure.

Figure 3 shows the annealing behaviors of *S* corresponding to positron annihilation in HfO_2 layers. For the 4-nm and 6-nm thick HfO_2 layers, their overall annealing behaviors of *S* are almost the same, and the *S* value increases as the annealing temperature increases up to 500ºC, suggesting the agglomeration of vacancy-type defects. A hump is observed after annealing at 500ºC, and this temperature coincides with the onset temperatures of the crystallization. This is attributed to the agglomeration of vacancies to absorb intrinsic open spaces in the amorphous phase. The 30-nm-thick HfO_2 layer shows crystalline phase before annealing, and its *S* value increases monotonically as the annealing temperature increases up to 800°C. Our results demonstrate that positron annihilation spectroscopy can provide insights into the behavior of vacancy-type defects in high-*k* dielectrics. The observed close relationship between the vacancy clusters and the phase transition suggests the possibility of controlling the phase transition of high-*k* dielectrics by modifying the defect properties.

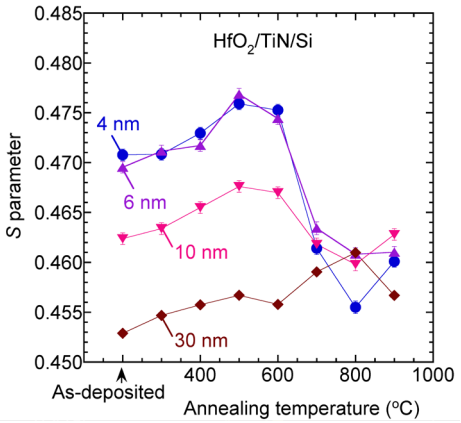

Fig. 3. Annealing behaviors of *S* corresponding to positron annihilation in HfO_2 layers. The thicknesses of HfO_2 are shown in the figure.

References

[1] J. Robertson and R. M. Wallace, Mat. Sci. Eng. R. 88 (2015) 1.

[2] A. Uedono et al., Thin Solid Films 762 (2022) 139557.

[3] B. E. O'Rourke et al., Jpn. J. App. Phys. Conf. Proc. 2 (2014) 011304.

4.3 Fabrication and functional development of one-dimensional organic nanostructures using high-energy charged particles

M. Nobuoka[1], A. Taguchi[1], H. Inoue[1], H. Miyashita[1], W. Choi[1], S. Seki[1]

Optoelectronic devices based on semiconductors are rapidly developing, driven by advances in the fabrication processes such as nanolithography. While fabrication of inorganic nanowires is already well-established, organic nanowires with finely tuned 1D structures have been rarely reported, despite expectations for a wide dynamic range of physical properties due to the designability of conjugated systems.

Our original fabrication technique for 1D nanomaterials offers a powerful and unique platform for developing nanomaterials with a broad dynamic range reflecting the nature of organic molecules. High-energy charged particles penetrating organic molecular condensates release kinetic energy within nanometer-scale regions called particle tracks. This efficient energy conversion into reactive intermediates enables localized chemical reactions such as polymerization and crosslinking, which our group has utilized over the past decade to design and produce functional nanomaterials from a variety of organic molecules [1]. This technique is referred to as Single Particle Linear Polymerization (STLiP) or Single Particle Nanofabrication Technique (SPNT) (Fig. 1).

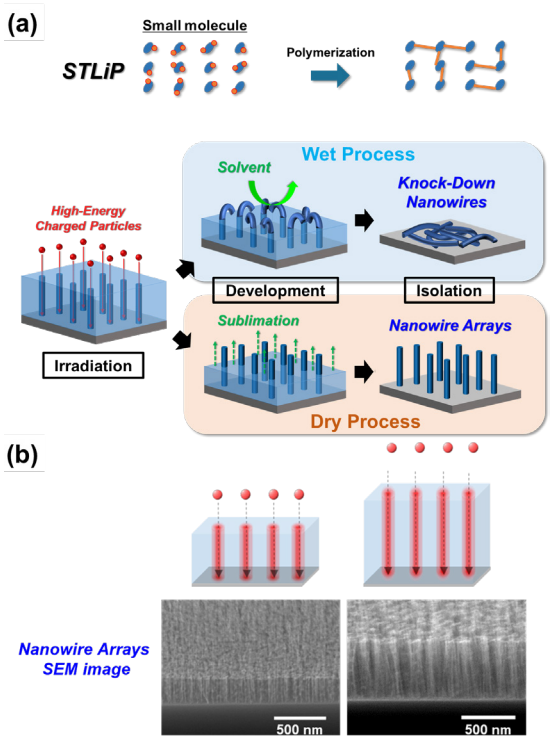

Fig. 1. (a) Schematic illustration of nanowire isolation and its morphology (wet and/or dry process) in SPNT and STLiP methods. (b) Scanning electron microscope (SEM) images of nanowire arrays by the STLiP method.

When targeting sublimable organic molecules, the STLiP technique enables fabrication of 1D nanomaterials with extremely high aspect ratios, unattainable by conventional methods [2]. Furthermore, sublimation-based protocols for developing and isolating the resulting 1D nanostructures minimize morphological impact, leading to nanowire arrays (Fig. 1) with aspect ratios over ~100 on a substrate via a simple process.

The particle energy primarily determines the penetration range in molecular condensates and thus the maximum aspect ratio of nanostructures, while particle fluence directly correlates with the density of nanostructures formed under the “one particle gives one 1D nanostructure” scheme. These free-standing ultra-high aspect ratio nanowires are envisioned for future applications in 1) sensing, 2) separation, and 3) energy harvesting.

[1]Kyoto University

1) Nanowires aimed at functional chemical modifications

Developing nanowires with chemically functionalizable surfaces is a key strategy for advancing sensor technologies. In this study, we selected tetrakis(4-ethynylphenyl)methane (TEPM), a derivative bearing highly reactive ethynyl groups. The feasibility of surface functionalization via Huisgen cycloaddition targeting residual ethynyl groups on the nanowires was examined. TEPM films were deposited onto silicon substrates by vacuum deposition and irradiated with Au ion beams (72–90 MeV) from the 6MV tandem accelerator at UTTAC. After irradiation, samples were immersed in solvent to remove unreacted regions. The nanowire formation was confirmed by microscopy (Fig. 2). Attempts to functionalize the isolated nanowires with 11-azido-3,6,9-trioxaundecan-1-amine (PEG) showed no significant chemical changes. We will focus on modifying with fluorescent molecules and explore alternative materials optimized for other chemical reactions.

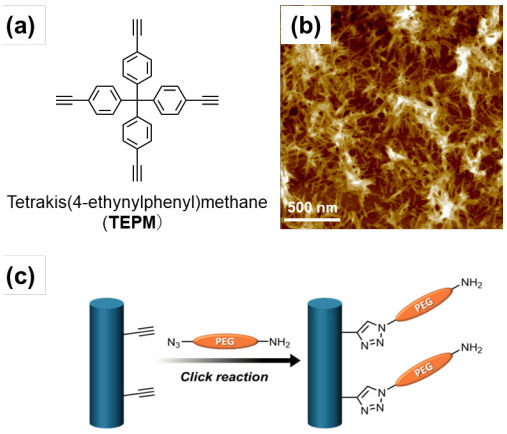

Fig. 2. Nanowires aimed at functional chemical modifications. (a) Molecular structure of TEPM. (b) Atomic force microscope (AFM) image of TEPM nanowires. (c) Schematic image of huisgen cycloaddition to organic nanowires.

2) Organic-Inorganic Hybrid Nanowires

Polyhedral Oligomeric Silsesquioxanes (POSSs) are a class of organic-inorganic hybrid materials in which organic side chains are chemically bonded to an Si-O-based inorganic framework. By combining the properties of both organic and inorganic components, POSSs exhibit a wide range of physical characteristics, including solubility, thermal and thermo-mechanical stability, mechanical strength, optical transparency, gas permeability, dielectric constant, flame resistance, and more. In this study, thin films of POSS were deposited onto silicon substrates via vacuum deposition and subsequently irradiated with Au beams (72–90 MeV) from the 6MV tandem accelerator at UTTAC. After irradiation, the samples were annealed at 200°C under high vacuum, resulting in the successful isolation of vertically aligned nanowires (Fig. 3). These nanowires, which are presumed to exhibit a glass-like structure, are being explored for applications in optical waveguides and fibers, leveraging the intrinsic advantages of organic-inorganic hybrid materials such as high dielectric performance and superior optical transparency.

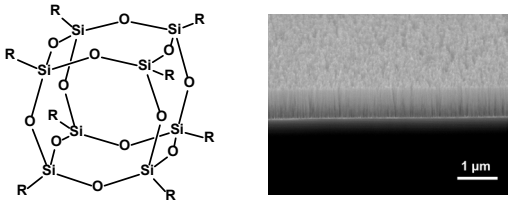

Fig. 3. Organic-inorganic hybrid nanowires. (a) Molecular structure of POSSs. (b) Scanning electron microscope (SEM) tilted image of POSS-derived nanowires.

References

[1] S. Sakaguchi et al., Quantum Beam Sci. 4 (2020) 7.

[2] K. Kamiya et al., Nat. Commun. 12 (2021) 4025.

4.4 Structural change in amorphous SiO_2 introduced with swift heavy ions

K. Awazu, K. Sasa, A. Uedono

A latent track is created by a swift heavy ion in silica glass. It is visualized by etching with the vapor of hydrofluoric acid. We successfully observed collision cascades, dotted columnar defects, and parallel latent tracks. We could create uniform holes with several nanometers in diameter with an aspect ratio of 100. These data are expected to be of great help to industrial research. For example, optical waveguides were created in glass with a high-energy ion beam for 6G telecommunication. It is also required from the industrial side to create holes with high aspect ratios in glass.

We used Corning 8655 as a fused silica. Silanol concentration is less than 1 ppm wt. The impurities are less than 1 ppb wt, and optical transmission at 193 nm is over 99.75%/cm. There must be very low concentrations of silanol because it has been known that in the case of silica, which contains a high silanol concentration, defects become unstable, and eventually its concentration decreases over time. The glass block is cut into 1 cm^2 square plates with a thickness of 1mm and polished to be suitable for the following experiments.

The 6MV tandem accelerator at UTTAC was employed for irradiation with 80 MeV I^{13+}. We used the 1m-diameter chamber on the L2 beamline, which is dedicated to beam irradiation of materials. Irradiation was performed at room temperature and a residual pressure below 1×10^{-4} Pa. The 80 MeV I^{13+} beam was scanned in vacuum by an alternating electromagnetic field to uniformize the ion fluence on the surface of a silica plate. To prevent the beat generation, the frequencies of the x and y directions were set to prime numbers, e.g., 5 and 7 Hz, respectively. While observing with an oscilloscope that the scanned area became homogenous, the optimum frequencies of the x- and y- direction were determined. The scan area (x and y) was 1.5×1.5 cm^2 for a silica glass plate with 1.0×1.0 cm^2. The beam current was monitored with two Faraday cups on the upstream and downstream sides of the irradiation position to measure the fluence.

Vapor etching of the irradiated silica glass was performed with a hydrofluoric acid diluted with $HF:H_2O = 1:2$. Since the etching rate is sensitive to temperature and humidity, the experiment was carried out in a clean room where the room temperature and humidity were constant at 23 ± 1℃ and 38 ± 4%, respectively. The temperature of the water bath was 21 ± 1℃, and the silica glass was kept at 38℃ on a temperature-controlled heater during etching.

Scanning Electron Microscope (SEM) gives us an image of nanopores of etched tracks. Figure 1 shows the SEM image of the silica glass surface irradiated with 80 MeV I^{13+} at a fluence of 1×10^{10} cm^{-2} and followed by vapor etching with diluted hydrofluoric acid. The number of holes can be estimated from the SEM image. When the number of holes was counted from 20 points on the surface of the 1 cm^2 of silica glass, there was an error of about ±30%. The hole diameter was estimated to be 37 ± 8 nm.

A cross-sectional specimen of the irradiated silica glass was prepared using a focused ion beam (FIB) and observed by TEM. Figure 2 shows a cross-sectional TEM image, where the ion tracks appeared by etching. The silica glass surface corresponds to the upper horizontal line, and 80 MeV I^{13+} passes from top to bottom and stops at a depth of 15 μm. The incident direction of ions on the silica glass surface was 7° off from the

surface normal to distinguish them from stripes that may be introduced during FIB processing. The dark gray holes tilted at 7° with high aspect ratios are all parallel. The diameter of the etched track at a depth of about 30 nm from the surface is estimated to be 30 nm, consistent with the SEM image in Fig. 1. In contrast, we should draw attention to the fact that the diameter of the etched track that extends to a depth of 1 to 2 μm is on the order of several nm. It is also noticed that the tracks of recoil atoms are visualized with etching.

Figure 3 shows the simulation result of the trajectory of 80 MeV I^{13+} in silica glass. The ions are incident perpendicular to the surface of silica glass from left to right. Note that in Fig. 3 a side view of 3×3 μm^2 area is shown. White lines are latent tracks due to 80 MeV I^{13+} ions. The trajectories of recoils of oxygen and silicon are indicated in red and blue, respectively. The simulated recoil pattern reproduces the actual TEM image.

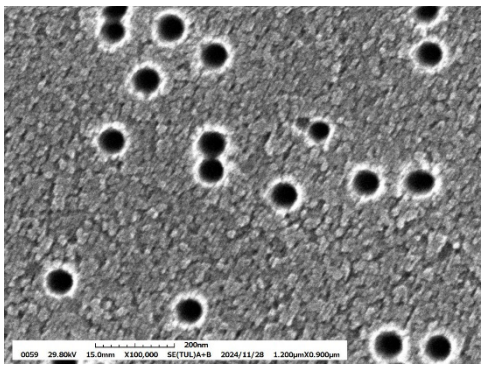

Fig. 1. SEM image of the surface of silica glass irradiated with 80 MeV I^{13+} at a fluence of 1 × 10^{10} cm^{-2} and followed by vapor etching. A scale bar of 200 nm is shown.

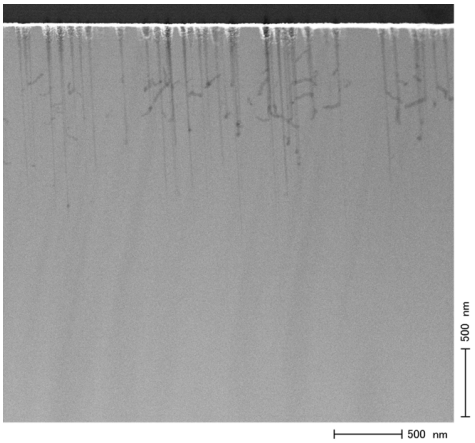

Fig. 2. Cross-sectional TEM image of the irradiated silica glass shown in Fig. 1.

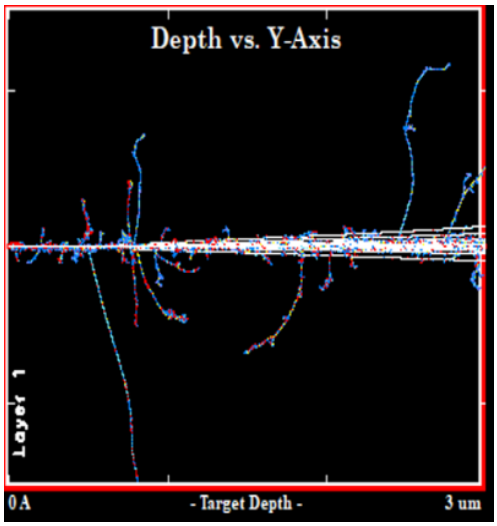

Fig. 3. Simulated trajectories of 80 MeV I^{13+} incident on silica glass. In the 3×3 μm^2 area, latent tracks are shown with white lines, while recoils of oxygen and silicon atoms are indicated in red and blue, respectively.

This work was conducted at the Nano Processing Facility in AIST. The Kakehashi-project, which TIA founded, financially supported this work.

4.5 Valence evaluation of Fe atoms in reactively sputtered Fe oxide thin films by Conversion Electron Mössbauer Spectroscopy (CEMS)

R. Minami, E. Kita, H. Yanagihara

We have demonstrated that continuous growth from metallic α-Fe to Fe_2O_3 is possible when iron oxides such as spinel ferrite are deposited by sputtering for use as thin-film magnetic materials [1]. Applications of thin-film materials are expanding from magnetic recording media to electronic devices, particularly those based on spintronics technology. Thin-film growth has become an important technology in manufacturing various high-performance devices. The growth mode of iron oxide changes from metallic to compound mode depending on the amount of O_2 gas in Ar, and the products and deposition rate are not uniquely determined. The deposition rate has hysteresis, and deposition cannot be controlled by gas flow rate and input power alone. To overcome this difficulty, we are conducting research to predict the deposition rate and products by observing plasma emission spectra (PES), which are thought to reflect all conditions during deposition [2]. In this report, Mössbauer spectroscopy is used to analyze the valence distribution in sputtered iron oxide films fabricated under different conditions. The ratio of Fe_3O_4 and γ-Fe_2O_3 in the thin film will be determined from the Mössbauer data, and a method will be developed to predict the valence by comparing the PES data with principal component analysis [3, 4]. For the purpose of film deposition control, we clarify the relationship between the intensity of plasma emission spectrum (PES), film deposition rate and an Fe valence distribution in the deposited thin films.

Fe oxide thin films were grown on MgO single crystal substrates by reactive sputtering and the plasma emission spectrum (PES) was measured during film formation. The conditions for sample preparation and plasma emission measurement were the same as in the previous report [3]. The ^{57}Fe Mössbauer spectroscopy was used to identify the valence distribution of Fe atoms, The valence of the Fe atoms in the product was identified using the ^{57}Fe conversion electron Mössbauer spectroscopy (CEMS). For CEMS, a RiKon5 CEMS detector (product of WissEL) was used with a He (1% isobutane) gas mixture (Q gas). To prevent the sample from being charged, the surface of the sample was electrically grounded with carbon tape. The spectra were analyzed with a least squares fitting program (MossWinn4).

Figures 1 and 2 show the Mössbauer spectra of Fe oxide thin films prepared by varying the oxygen gas flow rate. Figure 1 corresponds to the ascending process, in which the flow rate was increased from 0 to 1.5 sccm, while Fig. 2 represents the descending process, where the flow rate was decreased from 1.5 to 0 sccm. Two-digit numbers in Figs. 1 and 2 indicate the oxygen flow rate, for example “00” and “05” mean 0 and 0.5 sccm, respectively. Other letters, Asc and Des indicate the ascending and the descending process, respectively.

In the “00” case, the Mössbauer spectrum is in good agreement with bcc Fe. In the case of “02 Asc”, the Mössbauer spectrum shows a mixture of bcc Fe and a paramagnetic singlet peak probably due to FeO. For the higher oxygen rates, Fe_3O_4 were formed in the oxygen flow rate between 0.3 and 0.9 and γ-Fe_2O_3, at higher oxygen flow rates than 0.9 sccm. A hysteresis phenomenon was observed near the oxygen flow rate of 0.9 sccm. The valence distribution of Fe was determined by numerical fitting.

Optical emission spectrometry is a useful technique to analyze the growth process of iron oxide thin films in real time and to predict the valence and deposition rate of thin films. For the analysis, clarification is needed on how iron valence, film thickness, and optical emission data are related. The optical emission spectrometry data spans 3,000 channels, and we used principal component analysis to make the data channel smaller and simpler. The analysis determined principal component axes (PC1, PC2), and we successfully completed the analysis and clarified the relation between valence and principal components. Details will be published elsewhere [4]. The next step will be to achieve real-time control of film deposition with valence control of Fe oxides.

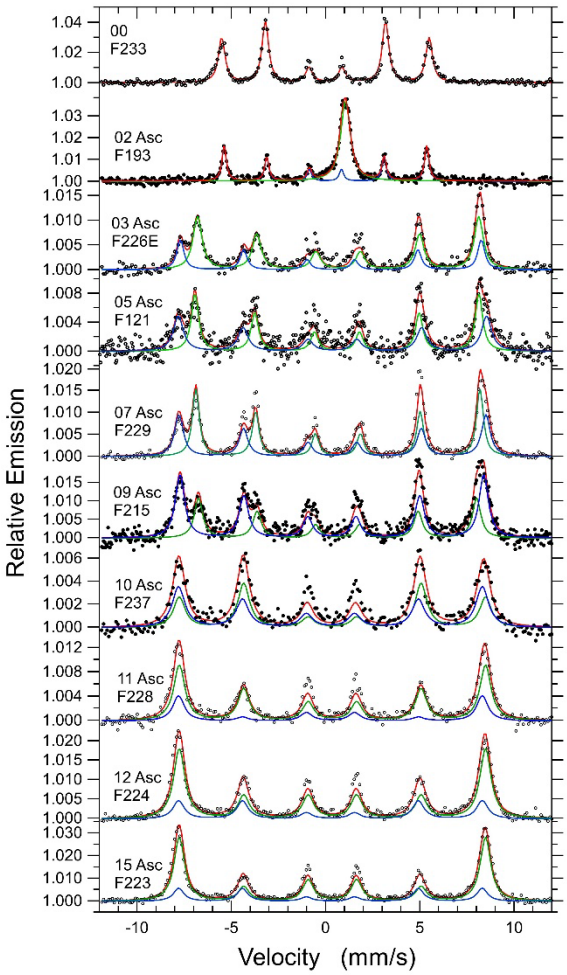

Fig. 1. CEMS for reactively sputtered Fe thin films grown in the ascending process.

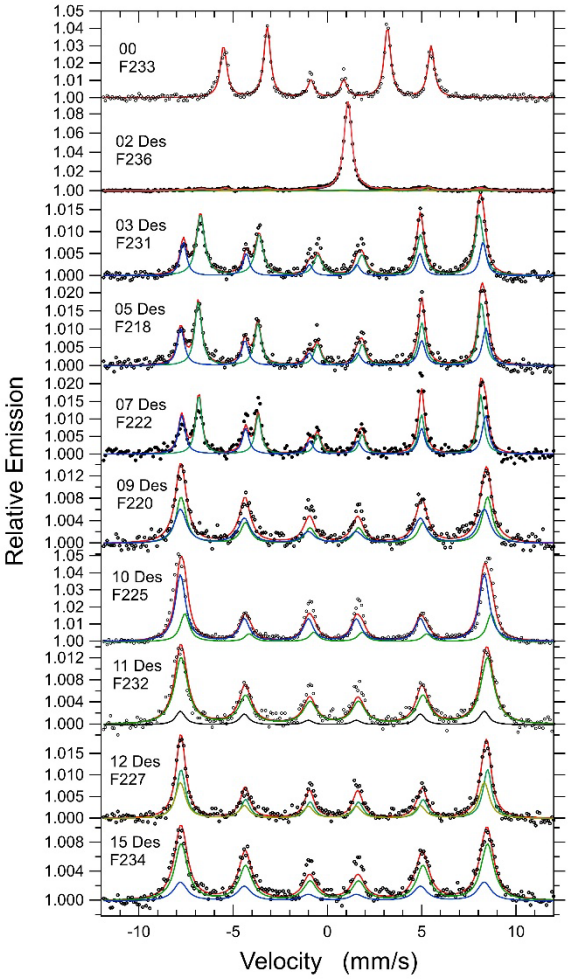

Fig. 2. CEMS for reactively sputtered Fe thin films grown in the descending process.

References

[1] H. Yanagihara et al., J. Phys. D 46 (2013) 175004.

[2] R. Minami et al., UTTAC Annual Report 2023, UTTAC-93 (2024) 29.

[3] R. Minami, Master thesis, Feb. 2025, Master's program in engineering science, University of Tsukuba.

[4] R. Minami et al., submitted to Science and Technology of Advanced Materials: Methods.

4.6 Mössbauer study of FeO thin films prepared with reactive sputtering

R. Waseda, R. Minami, E. Kita, H. Yanagihara

In spintronic devices such as MRAM, perpendicular magnetization is required due to its advantages for high-density integration. Therefore, research on magnetic materials with strong perpendicular magnetic anisotropy (PMA) is actively being pursued. Furthermore, iron (Fe) is abundant on Earth and is an important constituent element not only for structural materials but also for materials with high saturation magnetic flux density. Previous studies have confirmed PMA in Fe-containing composite systems such as Fe/MgO and Fe/NiO [1,2]. Therefore, we have focused on FeO, which, like MgO and NiO, is a divalent metal oxide with a rock-salt structure, and we anticipate the emergence of PMA at the Fe/FeO interface. However, because FeO is in a non-equilibrium state at room temperature, it is difficult to grow stoichiometric crystals using conventional sample preparation methods. To overcome this difficulty, high pressure synthesis methods have been attempted. Furthermore, non-equilibrium sample synthesis methods such as reactive sputtering are also considered to be effective, but the deposition of FeO thin films has not yet been fully established compared to the growth of iron oxides in high oxidation states [3,4]. Therefore, in this study, we aimed to prepare FeO thin films using the reactive sputtering method.

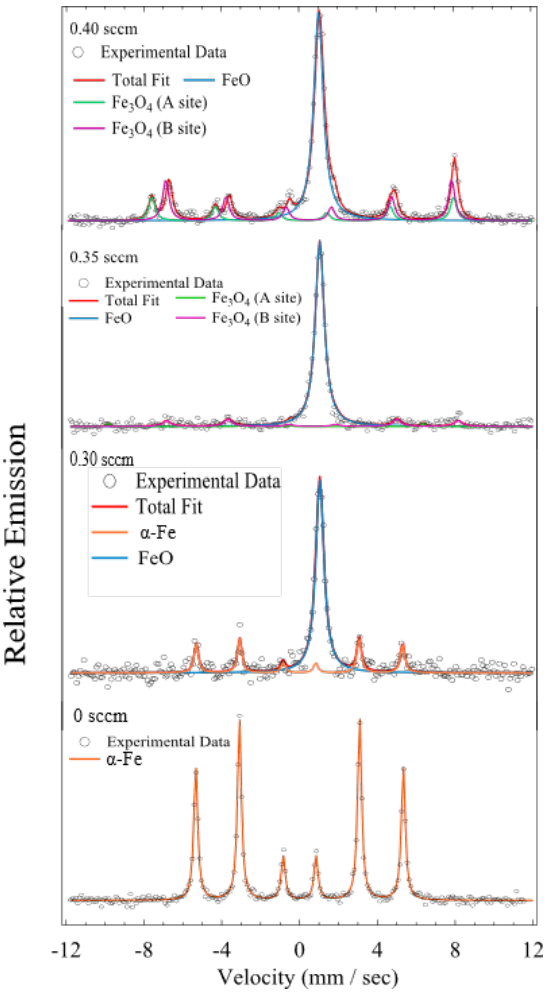

Fig. 1. Mössbauer spectra of Fe-O reactively sputtered films.

For the growth of FeO thin films, reactive RF magnetron sputtering was employed using a metallic iron (Fe) target, with O_2 gas introduced into an Ar gas atmosphere as the reactive gas. MgO(001) single crystals were used as substrates, and samples were fabricated by varying the oxygen flow rate between 0.00 and 0.60 sccm [3]. These samples were analyzed by conversion electron Mössbauer spectroscopy (CEMS) to determine the valence state of the Fe atoms. The CEMS measurements were performed using a RiKon5 CEMS detector (manufactured by WissEL) with a He (1% isobutane) gas mixture (Q-gas) as the counter gas. Samples with an area of approximately 10 × 10 mm² were set in the CEMS detector. To prevent electrostatic charging, carbon tape was attached to the sample surface and then grounded. RHEED measurements after film growth confirmed that the iron oxide thin film grew epitaxially on the MgO substrate. Figure 1 shows the Mössbauer spectra for samples prepared at oxygen flow rates of 0.00,

0.30, 0.35, and 0.40 sccm. For the sample prepared at an oxygen flow rate of 0.00 sccm, a six-line spectrum indicative of magnetic splitting was observed. Based on its internal magnetic field of 33 T and an isomer shift of 0 mm/s, this sample can be identified as α-Fe. Furthermore, since no spectral lines other than this sextet were observed, it was confirmed that the sample is a single phase of α-Fe.

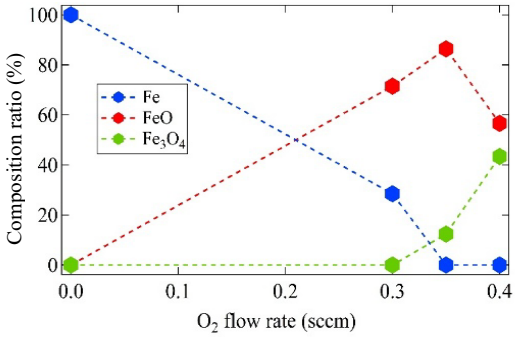

Fig. 2. Oxygen flow rate dependence of the composition ratio of the samples.

In samples prepared with oxygen flow rates exceeding 0.30 sccm, an unsplit singlet spectrum was also observed. This is attributed to FeO, which is paramagnetic at room temperature. Additionally, at an oxygen flow rate of 0.30 sccm, α-Fe spectra were observed alongside the FeO spectrum. In contrast, at 0.35 and 0.40 sccm, Fe_3O_4 spectra were detected. These results indicate that with increasing oxygen flow rate, the phase composition of the grown thin films changes sequentially from α-Fe to FeO, and then to Fe_3O_4. Figure 2 illustrates the estimated proportions of the constituent phases in the thin films at various oxygen flow rates, as determined from the Mössbauer spectroscopy results. The proportion of FeO is observed to increase up to an oxygen flow rate of 0.35 sccm and then decrease at higher flow rates. This indicates that single-phase FeO is formed at an oxygen flow rate around 0.35 sccm.

By adjusting the oxygen flow rate during the deposition of iron oxide thin films, the resulting phases changed from α-Fe to FeO, and then to Fe_3O_4. Figure 2 suggests that single-phase FeO can potentially be formed at oxygen flow rates between 0.30 and 0.35 sccm.

Table 1. Mössbauer parameters of Fe oxide thin film prepared with reactive sputtering

Sample	Site		H_{hf} (T)	*IS* (mm/s)	LW (mm/s)	Area (%)
0.4 sccm	M1	Spinel A	48.5	0.214	0.37	15.9
	M2	Spinel B	45.8	0.661	0.314	27.5
	S1	FeO	–	1.07	0.596	56.56
0.35 sccm	M1	Spinel A	50.3	0.215	0.268	1.21
	M2	Spinel B	46.6	0.675	0.495	12.4
	S1	FeO	–	1.05	0.556	86.4
0.3 sccm	M1	α-Fe	33.1	0.000	0.263	28.5
	S1	FeO	–	1.05	0.511	71.5
0.0 sccm	M1	α-Fe	33.1	0.000	0.242	100.0

H_{hf}: hyperfine magnetic field, *IS*: isomer shift relative to α-Fe, LW: line width

References

[1] J. W. Koo et al., Appl. Phys. Lett. 103 (2013) 192401.

[2] S. Kobayashi et al., Phys. Rev. Appl. 19 (2023) 064005.

[3] H. Yanagihara et al., J. Phys. D: Appl. Phys. 46 (2013) 175004.

[4] R. Minami et al., UTTAC Annual Report 2023, UTTAC-93 (2024) 29.

4.7 Mössbauer study of M-type La-Co-Sr ferrite fine particles using a molten salt method

K. Horie, E. Kita, M. Kishimoto, H. Yanagihara

M-type Sr-ferrite is currently used in various applications due to its cost-effectiveness, as it is less expensive than other permanent magnet materials and exhibits a relatively high maximum energy product. Therefore, extensive researches have been conducted to enhance the magnetic properties of M-type Sr-ferrite. In our previous studies, instead of using the conventional solid-state reaction method, we aimed to improve the coercivity of M-type Sr-ferrite by employing the molten salt method [1]. This technique utilizes a flux agent capable of dissolving other substances at high temperatures, allowing crystal growth to occur within the solution during heat treatment. Consequently, M-type Sr-ferrite can be crystallized at lower temperatures compared to the solid-state reaction method, resulting in uniform and fine crystalline particles. If the crystal grain size becomes smaller than the critical radius for forming a single magnetic domain, the coercivity is expected to increase.

Moreover, it is known that substituting Sr^{2+} with La^{3+} and Fe^{3+} with Co^{2+} in M-type Sr-ferrite enhances its magnetic properties compared to the unsubstituted form [2]. This improvement arises because Co^{2+}, which has a smaller magnetic moment than Fe^{3+}, substitutes preferentially at some of the antiparallel Fe sites among the five Fe sites in the structure, thereby increasing the net magnetization. Therefore, identifying the specific Fe sites where Co^{2+} is substituted and their occupancy ratios is crucial for optimizing performance. The site occupancy of Co^{2+} can be estimated using Mössbauer spectroscopy. In this study, we synthesized La and Co substituted M-type Sr-ferrite fine particles via the molten salt method with the aim of enhancing their magnetic properties.

The metal chlorides were weighed according to their stoichiometric ratios, and NaOH was added and stirred to form precipitates of hydroxides. KBr was added as a flux agent, and the mixture was dried at 80°C, followed by heat treatment at 900°C in a muffle furnace to obtain La-Co-substituted M-type Sr-ferrite fine particles. The crystalline structure of the synthesized samples was analyzed by X-ray diffraction (XRD) and, ^{57}Fe Mössbauer spectroscopy was conducted at room temperature for 2 samples of non-doped M-type Sr-ferrite, $SrFe_{12}O_{19}$, (SrM) and $Sr_{0.9}La_{0.1}Fe_{11.9}Co_{0.1}O_{19}$ (La-Co-SrM) fine particles. The spectra were fitted using the commercial analysis software MossWinn Pro4 and the Fe site substitution of Co^{2+} in the samples was estimated from the result.

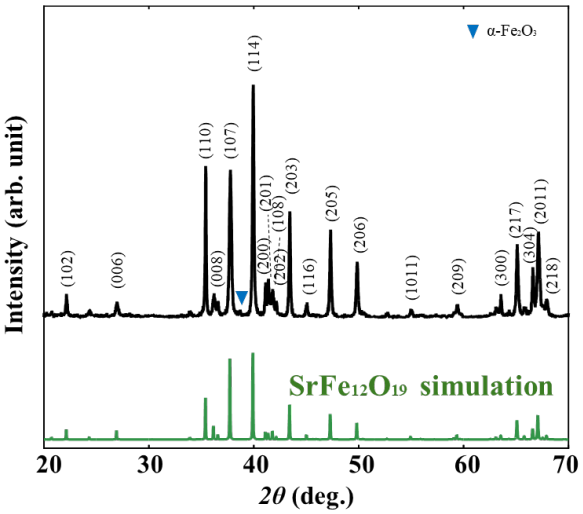

Fig. 1. XRD pattern of $Sr_{0.9}La_{0.1}Fe_{11.9}$ $Co_{0.1}O_{19}$ particles. Upper panel and lower panel show experimental data and the result of numerical simulation, respectively.

Figure 1 shows the XRD measurement results. The

diffraction pattern confirms that the main phase is M-type Sr-ferrite, although minor peaks corresponding to α-Fe_2O_3 were also observed. The result of Rietveld refinement is shown in the lower part of Fig. 1, indicating that the M-type Sr-ferrite phase accounts for 92.1 wt%.

Figure 2(a) presents the spectrum of unsubstituted M-type Sr-ferrite, while Fig. 2(b) shows the spectrum of the La-Co-substituted sample. The Mössbauer parameters of hyperfine fields (H_{hf}), isomer shifts (*IS*) and quadrupole shifts (*QS*) obtained from the fitting, along with the corresponding crystallographic sites [3], are listed in Table 1. The fitting curves are shown by solid lines in Fig. 2. A comparison of the two spectra reveals a noticeable change in the peak shape around 9 mm/s. Furthermore, Table 1 shows that the relative area of the $4f_2$ site decreased significantly by 5% compared to the other sites, suggesting that a majority of Co^{2+} ions were substituted at the $4f_2$ site.

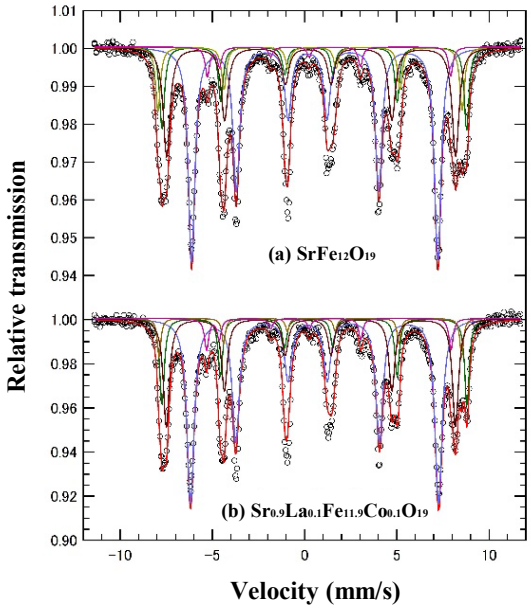

Fig. 2. Mössbauer spectra of $SrFe_{12}O_{19}$ and $Sr_{0.9}La_{0.1}Fe_{11.9}Co_{0.1}O_{19}$ particles. Open circles display experimental data, and solid lines show results of fitting.

Table 1. Mössbauer parameters of $SrFe_{12}O_{19}$ and $Sr_{0.9}La_{0.1}Fe_{11.9}Co_{0.1}O_{19}$

Sample	Site	H_{hf} (T)	*IS* (mm/s)	*QS* (mm/s)	LW (mm/s)	Area (%)
SrM	12k	41.5	0.353	0.387	0.432	47.1
	4f1	51.3	0.380	0.291	0.314	13.3
	4f2	51.2	0.347	–0.101	0.315	10.3
	2a	48.7	0.274	0.155	0.449	25.1
	2b	41.0	0.263	2.12	0.263	4.23
La-Co-SrM	12k	41.8	0.350	0.375	0.465	49.8
	4f1	51.4	0.379	0.311	0.299	15.1
	4f2	51.0	0.334	–0.0436	0.231	5.17
	2a	48.7	0.266	0.151	0.396	25.0
	2b	41.2	0.258	2.10	0.271	4.96

IS: isomer shift relative to α-Fe.

References

[1] M. Kishimoto and H. Yanagihara, J. Magn. Magn. Mater. 579 (2023) 170871.

[2] A. Shimoda, et al., J. Solid State Chem. 239 (2016) 153.

[3] G. P. Nethala, et al., Physica B: Condensed Matter 550 (2018) 136.

4.8 Preparation and Mössbauer study of NdFe oxide nanoparticles

M. Kishimoto, T. Sekido, E. Kita, H. Yanagihara

Rare Earth-Transition metal alloys have been utilized for high performance magnets such as $Nd_2Fe_{14}B$. Research into new materials is being continuously conducted to meet the demand for lighter permanent magnets and improved cost performance. In particular, the thermal characteristics of the coercive force of permanent magnets are important research subjects that need to be improved. To address this issue, high magnetic anisotropy and high transition temperature are desired. However, even if excellent properties can be predicted, it is not necessarily possible to achieve them using conventional methods. Therefore, other methods must be considered. We focus on $NdFe_{12}$ compounds, which have a $ThFe_{12}$ type crystal structure, and pursue the possibility of realizing them through the synthesis of oxide nanoparticles.

Nd-containing FeO-based nanoparticles [Fe(Nd)O] were prepared by mixing Fe and a small amount of Nd chloride solutions to the desired composition of Nd:Fe = 1:11, and adding sodium hydroxide to obtain hydroxides as coprecipitates. The coprecipitates were then heated to 350 °C under a hydrogen atmosphere (reduction treatment) and further heated to 450 °C in nitrogen gas (heat treatment) as shown in Table 1. X-ray diffraction (XRD), transmission electron microscopy (TEM), and Mössbauer spectroscopy were performed on the obtained samples.

TEM images of the reduced Fe(Nd)O nanoparticles confirmed that the particle size was 20-30 nm. Figure 1 shows the XRD pattern. Peaks derived from the FeO crystalline phase are mainly observed, with a broad peak due to the spinel structure observed around $2\theta = 30°$. On the other hand, in Sample 5, which has a low reduction temperature of 360°C, the peak derived from the FeO phase shifts to the high-angle side, suggesting the possibility that the FeO lattice contracts. In addition, peaks derived from the Fe_3O_4 phase and the α-Fe phase also appear.

Table 1. List of samples

Sample	Heat Treatment
# 0	380°C× 5min(H_2) + 450°C×29h(N_2)
# 5	360°C× 5min(H_2)
# 6	360°C× 5min(H_2) + 450°C×29h(N_2)

The Mössbauer spectra recorded at room temperature and 3 K for Samples 0, 5, and 6 are shown in Figs. 2 and 3, respectively. At room temperature, all spectra can be fitted with paramagnetic doublets, probably derived from Fe^{3+} and Fe^{2+} ions, as well as a small amount of α-Fe and Fe_3O_4. Two paramagnetic doublets have almost the same parameters and are differing only in the area ratio, which suggests that the paramagnetic part has a similar structure (basically FeO) throughout the samples. The magnetic ordering temperature of FeO is about 200 K, which seems to support the results in the paramagnetic state. In contrast, the

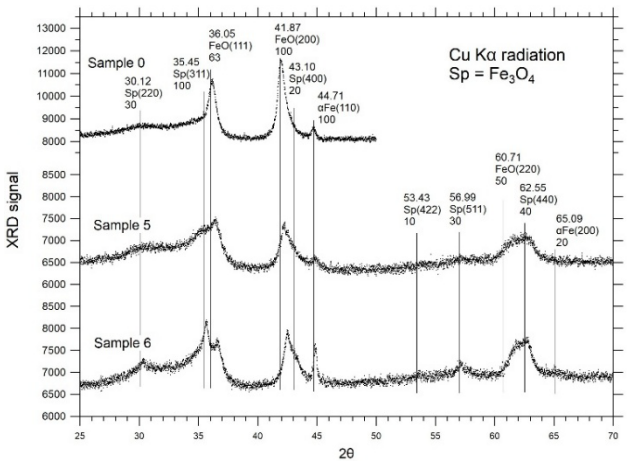

Fig. 1. XRD patterns of NdFe oxide nanoparticles.

Mössbauer spectra measured at 3 K are not very similar. For Sample 0, the Mössbauer spectrum shown in Fig. 3(a) is composed of Mössbauer spectra from Fe^{3+} and FeO [1], and the parameters are summarized in Table 2. The observed hyperfine magnetic field component of 50 T can be attributed to Fe^{3+} belonging to both spinel and FeO sites. In Samples 5 and 6, both spectra are consistent with those of mainly Fe^{3+} ions, with a small amount of α-Fe. These spectra suggest that Samples 5 and 6 are composed mainly of iron oxides of Fe^{3+}, e.g., γ-Fe_2O_3. It is more clearly seen in Sample 6. Since the magnetic transition temperature of γ-Fe_2O_3 is about 600 K, the paramagnetic behavior observed at room temperature is not due to a normal magnetic transition, but due to superparamagnetic behavior resulting from the small grain size. This study discovered the possibility of forming FeO, which is stable at high temperatures, into nanoparticles at low temperatures. Future work will involve determining the location of the Nd atoms and clarifying the magnetic properties.

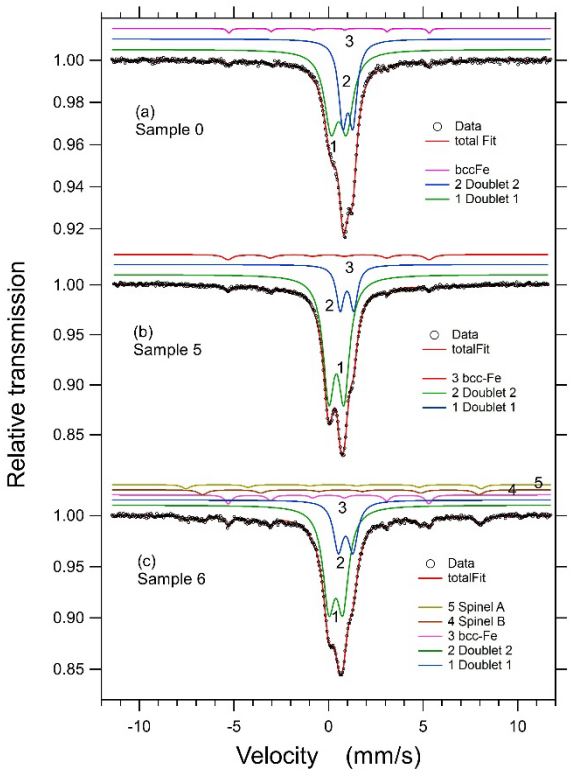

Fig. 2. Mössbauer spectra of NdFe oxide nanoparticles recorded at room temperature.

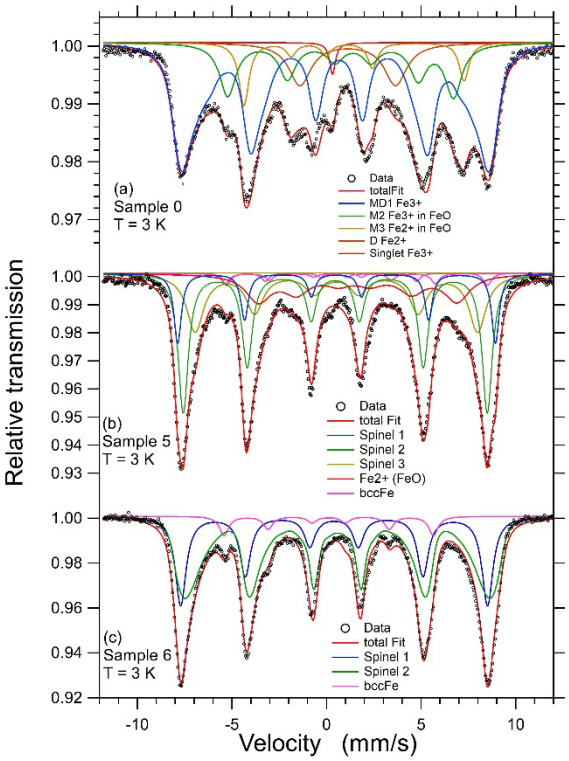

Fig. 3. Mössbauer spectra of NdFe oxide nanoparticles recorded at 3 K.

Table 2. Mössbauer parameters for Sample 0 measured at 3 K

	Sub-spec		H_{hf} (T)	*IS* (mm/s)	*QS*(mm/s)	*LW*(mm/s)	Area(%)
Sample 0 T=3K	MD1	Fe^{3+} Spinel	48	0.567	–0.205	0.771	61
	M2	Fe^{3+} in FeO	36.2	0.249	2.378	0.62	8
	M3	Fe^{2+} in FeO	37.1	1.07	–0.648	1.05	19
	D	Fe^{2+}	-	1.112	5.05	1.43	10
	S1	Fe^{3+}	-	0.316	-	0.37	1

H_{hf}: hyperfine magnetic field, *IS*: isomer shift relative to α-Fe, *QS* : quadrupole shift, *LW*: line width

Reference

[1] C. Wilkinson et al., Inorganic Chem. 23 (1984) 3136.

4.9 Estimation of Li mobility in all-solid-state Li-ion battery

N. Kishi, K. Yamamoto, S. Shinohara, D. Sekiba, S. Kobayashi[1], R. Shimizu[1], T. Hitosugi[1]

Recently, we have studied the Li migration in the all-solid-state Li-ion batteries by nuclear reaction analysis (NRA) with ^{7}Li(p, α)^{4}He. The battery consists of three layers: the cathode layer (pure Li), the electrolyte (Li_3PO_4, so called LPO), and the anode (pure Au). The experimental setup and the details of sample structures were described in previous reports [1,2].

Discharge of the Li battery corresponds to the case that it powers and/or drives an external device. In this case, we observed a decrease of the Li amount in the cathode layer, and on the other hand, the formation of Li-Au alloy in the anode layer was found out. This implies the Li migration toward the anode. The microscopic detail occurring in the LPO layer is, however, unknown. In other words, we do not yet understand the contribution of Li in the LPO layer containing a lot of Li atoms.

The primary question of interest for us is whether the LPO layer contains a rigid structure or not. If not, the LPO layer is the electrolyte of the battery, meanwhile it could play also the role of the Li ion provider. In order to examine this issue, we prepared a simple double-layered sample. We deposited $^{6}Li_3PO_4$ (t=600 nm)/$^{7}Li_3PO_4$ (t=600 nm) on an Al_2O_3 substrate by using the laser ablation and an isotope-enriched target. The chemical potentials of the two layers for the Li ions are, in principle, the same except the isotope (or entropy) effect, which is negligible at room temperature. Only thermal diffusion can induce intermixing of the mobile ^{6}Li and ^{7}Li ions, if such mobile ions exist.

Figure 1 shows the NRA profile measured for this sample. We note that our NRA is sensitive only to ^{7}Li. The result is somewhat unexpected one. Most of ^{7}Li atoms (or ions) spread out over the two layers almost uniformly. From the deconvolution of the spectral feature, ~95% of the Li atoms in LPO is highly mobile. No rigid structure is expected to exist in the LPO layer.

This result implies that the positive charge transfer in the battery is not caused by simple Li^{+} ion migration, but by collaboration with the Li atoms (and/or ions) provided from the electrolyte.

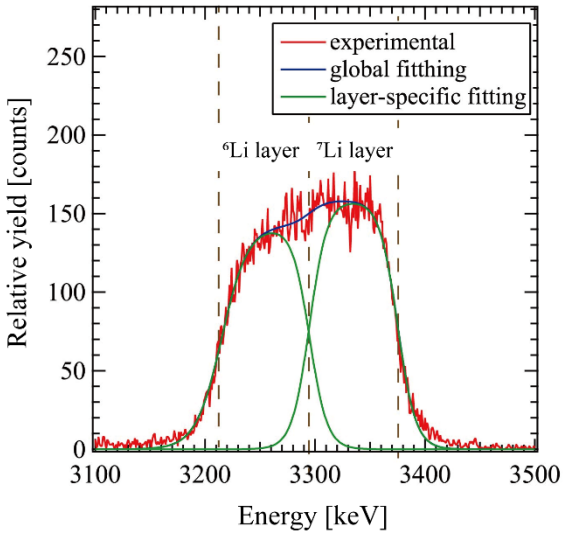

Fig. 1. NRA profile of the double layered ($^{6}Li_3PO_4$/$^{7}Li_3PO_4$) sample deposited on an Al_2O_3 substrate. Each layer has the thickness of 600 nm.

References

[1] N. Kishi et al., UTTAC Annual Report 2022, UTTAC-93 (2023) 33.

[2] N. Kishi et al., UTTAC Annual Report 2023, UTTAC-94 (2024) 35.

[1]The University of Tokyo

4.10 ERDA on Fomblin oil as a neutron reflection material

K. Yamamoto, S. Shinohara, N. Kishi, D. Sekiba, S. Kawasaki[1], K. Mishima[2]

The amount of hydrogen absorbed on and/or contained in Fomblin oil has been quantified by conventional elastic recoil detection analysis (ERDA) at D-course of 1MV Tandetron at UTTAC. While Fomblin oil is nominally hydrogen-free in terms of its chemical composition, the amount of surface-adsorbed hydroxyl groups and water molecules dissolved in the oil has not been quantitatively characterized. The previously developed rotational sample holder for ERDA on liquids was used to determine the hydrogen content both on the surface and inside of Fomblin oil [1].

A 2.5 MeV He^{2+}beam was employed for ERDA. The recoils and backscattered particles were detected by Si surface barrier detector (SSD) mounted at 30° and 150° with respect to the ion incident direction, respectively. Figure 1 (a) and (b) show the results of Rutherford backscattering spectrometry (RBS) and ERDA, respectively. The duration of data acquisition was about 6 hours for ERDA with the beam current of ~1 nA. Although the number of recoil signals is relatively small, it is significantly higher than the background. From these results, it was found that hydrogen exists at an atomic density of $(8.0 \pm 1.2) \times 10^{18}$ atoms/cm^3 up to 100 nm below the surface of Fomblin oil. The results revealed that the hydrogen content is higher than initially expected. The potential influence of this amount of hydrogen on neutron reflection will be investigated in future work.

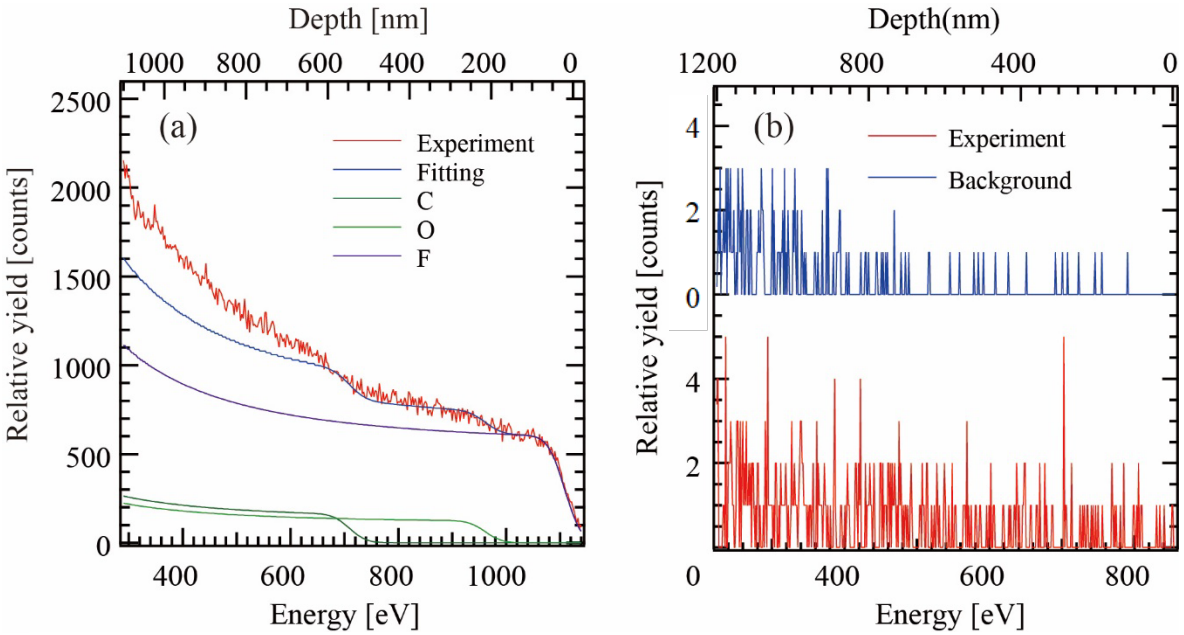

Fig. 1. (a) RBS spectrum of Fomblin oil with corresponding simulation results, (b) ERDA results for analysis of hydrogen distribution in Fomblin oil.*

Reference

[1] D. Sekiba et al., UTTAC Annual Report 2023, UTTAC-94 (2024) 37.

[1]High Energy Accelerator Research Organization (KEK)
[2]Osaka University
*The vertical axis label in Fig. 1 (b) was revised by the editorial team to reflect the content of the text.

5.

ION-BEAM IRRADIATION EFFECT

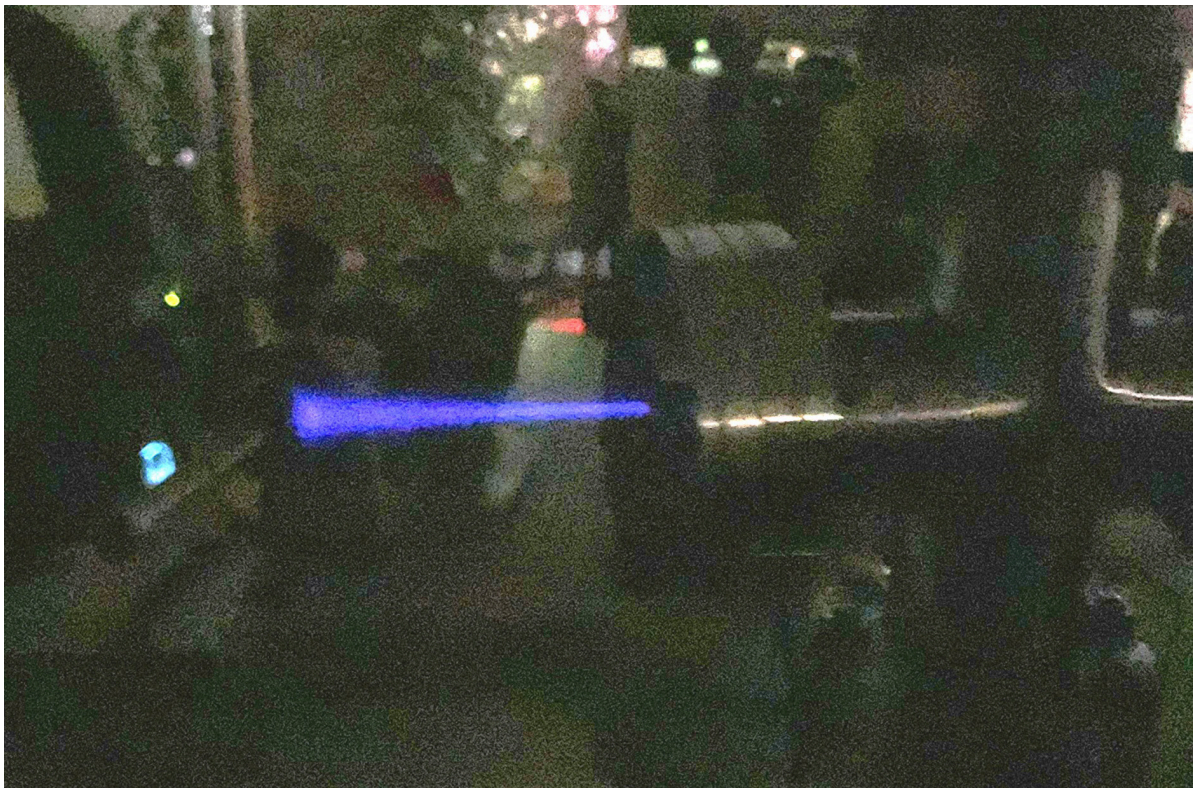

Ion Beam Irradiation in the Atmosphere. A 1.9 MeV hydrogen beam, emerging into the air through Kapton film from vacuum (from right to left), emits blue light upon collision with nitrogen in the atmosphere.

––*Report 5.1*

5.1 An investigation for an integrated proton-dynamic therapy, iPDT, using the resonant nuclear reaction between ^{15}N and a proton beam

H. Matsui, H. Kurokawa, A. Taninaka, I. Suzuki, Y. Kobayashi, K. Sasa, S. Ishii

We have carried out test measurements regarding basic research for cancer treatment using the resonant nuclear reaction ^{15}N(^{1}H, $\alpha_1\gamma$)^{12}C between the stable isotope ^{15}N in the cancer cells and a MeV proton beam [1, 2]. Test samples were normal gastric epithelial cells and gastric cancer cells with/without ^{15}N-aminolevulinic acid (^{15}N-ALA) treatment.

A 1.92 MeV proton beam from the UTTAC Tandetron was led into the atmosphere after passing through a Kapton film of 7.5 μm thickness and was incident on the samples. The beam current and the beam size before entering the Kapton film were ~1nA and 2–3 mm, respectively.

After 2 nC proton irradiation of the cells with ^{15}N-ALA, a cancer specific cellular nuclear modification occurred. As seen in Fig. 1, the cancer cellular nuclei obviously suffer a morphological change while normal cellular nuclei remain few changes. In the 2025 academic year, the authors plan to investigate a possible mechanism of the phenomenon.

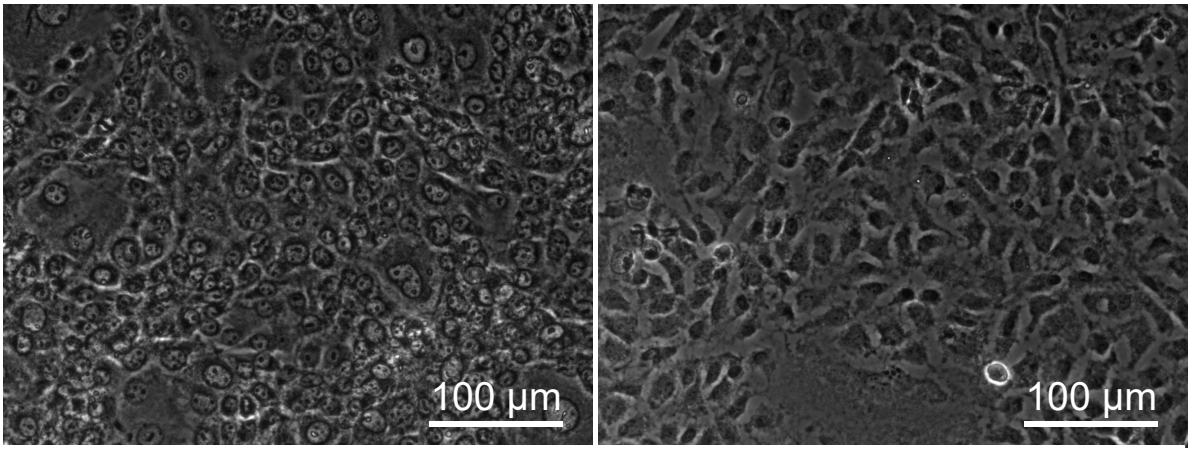

Fig. 1. Optical phase contrast images of both cancer (left) and normal (right) gastric epithelial cells after iPDT.

References

[1] I. Suzuki, et al., UTTAC Annual Report 2021, UTTAC-91 (2022) 50.

[2] I. Suzuki, et al., UTTAC Annual Report 2022, UTTAC-92 (2023) 45.

5.2 Comparison of SEE tolerance in different 4H-SiC MOSFET structures

M. Takahashi[1], K. Hiramatsu[2], M. Iwata[1], T. Suzuki[1], S. Harada[2], H. Shindou[1]

Silicon carbide (SiC) power devices are considered highly promising candidates for space applications due to their superior physical and electronic properties. However, several challenges have been identified with SiC devices when exposed to harsh radiation environments, including Single Event Effects (SEEs) induced by heavy ions. Among these, Single Event Burnout (SEB) and Single Event Gate Rupture (SEGR) can lead to catastrophic device failure [1-3]. In this study, two types of SiC power MOSFETs were subjected to heavy ion irradiation tests to evaluate and compare their susceptibility to SEEs and to identify their distinct failure modes associated with each device.

Figure 1 illustrates the cross-sectional structures of the two types of SiC MOSFETs fabricated at the National Institute of Advanced Industrial Science and Technology (AIST) and evaluated in this study. Fig. 1(a) and (b) show a SiC trench-gate MOSFET and a planar-gate MOSFET, respectively. Both devices feature epitaxial layers with a thickness of 10 μm grown on n-type 4H-SiC substrates with a doping level of 1.0×10^{16} cm^{-3}. A 60-MeV Al^{9+} beam from the 6MV tandem accelerator at UTTAC was used to conduct irradiation tests, in which the device chips were irradiated in the direction perpendicular to their surfaces with a fluence set at 3.0×10^5 p/cm^2. In this case, LET and the range in SiC are 12.1 MeV/(mg/cm^2) and 14.9 μm, respectively. The drain current (I_D) and the gate current (I_G) were monitored during the irradiation.

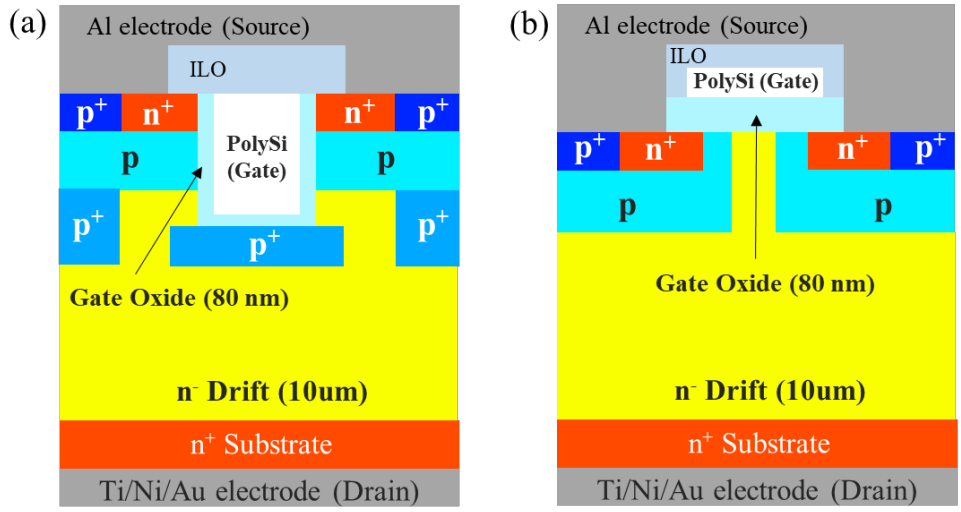

Fig. 1. Cross-sections of the two types of 4H-SiC MOSFETs used in this study. (a) trench-gate MOSFET, (b) planar-gate MOSFET.

Figure 2 shows the transitions of I_D and I_G as functions of the applied drain voltage (V_D) during the irradiation. The trench-gate MOSFET demonstrated higher SEE tolerance compared to the planar-gate

[1]Japan Aerospace Exploration Agency (JAXA)
[2]National Institute of Advanced Industrial Science and Technology (AIST)

MOSFET, and distinct failure mechanisms were observed for each device. In the trench-gate MOSFET, a rapid increase in drain current was observed at V_D = 800 V, leading to SEB. On the other hand, a rapid increase in gate current at V_D = 400 V indicates the occurrence of SEGR in the planar-gate MOSFET. These findings suggest that the structural differences between trench-gate MOSFETs and planar-gate MOSFETs lead to variations in internal electric field distributions under the Al^{9+} irradiation. Consequently, the locations of electric field concentration within the MOSFETs changed, resulting in different failure modes, as indicated in Fig. 2.

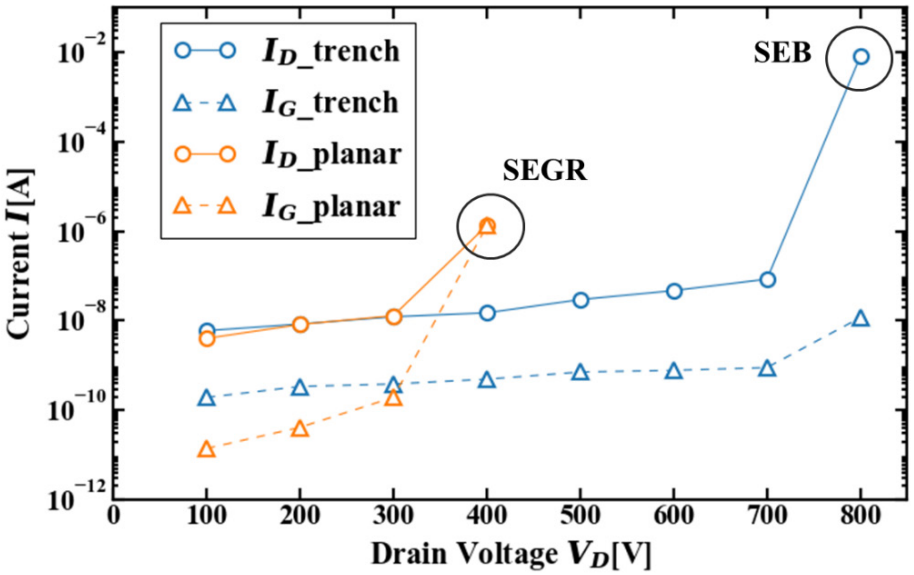

Fig. 2. Results of I_D and I_G transition during the Al^{9+} irradiation of trench-gate and planar-gate 4H-SiC MOSFETs.

This study was conducted under a joint research project of Tsukuba Power Electronics Constellations (TPEC). K. Hiramatsu was assigned from MIRISE technologies.

References

[1] C. Martinella et al., IEEE Trans. Nucl. Sci. 66 (2019) 1702.

[2] M. Takahashi et al., Solid State Phenomena 358 (2024) 1.

[3] M. Takahashi et al., abstract of ICSCRM 2024, p. 220 (2024).

5.3 Unusual saturation of critical current density in $YBa_2Cu_3O_7$ films irradiated with 300- and 84-MeV Au ions

H. Matsui[1], I. Yamaguchi[1], N. Ishikawa[2]

Critical current density (J_c) in a zero applied-magnetic-field, namely, a so-called self-field J_c (J_c^{sf}), is one of the most fundamental physical quantities in a superconductor and determines the performance of practical devices such as power transmission cables. However, the ideal microstructures for maximizing J_c^{sf} has not been well clarified in $YBa_2Cu_3O_7$ (YBCO), especially at high temperatures (> 60 K). For understanding the mechanism and enhancement strategy of J_c^{sf} in YBCO at high temperatures, it is essential to clarify the systematic variation in the J_c^{sf} in response to well-characterized and controlled vortex-pinning-centers (pins) in the range (at least) near the current highest-reported value, namely, about 10% of depairing current density (J_0).

In this work [1], we have accomplished this task by observing an ion-irradiation-driven, 2-fold enhancement of J_c^{sf} in YBCO films at 77 K, reaching a maximum $0.12J_0$ (i.e. J_c^{sf} = 4.5 MA/cm^2 vs J_0 = 36 MA/cm^2). YBCO epitaxial films (critical temperature T_c = 90 K) on CeO_2-buffered $SrTiO_3$ substrates were prepared by fluorine-free metal-organic deposition [1]. Irradiation with 84- and 300-MeV Au ions in a vacuum of 1×10^{-6} Torr at room temperature was respectively performed using a tandem accelerator at the University of Tsukuba and at Japan Atomic Energy Agency (JAEA). The incident angle of ions was set normal to the film surface. Figure 1 shows cross-sectional transmission-electron-microscopy (TEM) images of our 84 and 300-MeV irradiation samples. The dark contrasts correspond to the irradiation damages (pins). J_c^{sf} and T_c were measured inductively with a THEVA Cryoscan (liquid nitrogen bath).

Figure 2(a) shows the dose (Φ) dependence of J_c^{sf} in Au-irradiated YBCO films. To clearly show the detailed J_c^{sf} variation in the low Φ region, Fig. 2(b) shows the linear plots of the same data as Fig. 2(a). The matching field $B_\Phi = \Phi_0\Phi$ (Φ_0 is the flux quantum) is labeled by the top axes, and the Φ-dependence of T_c for samples with t =1000 nm is shown in the inset in Fig. 2(a). We find that J_c^{sf} starts to increase at around Φ_{sf} ranging from 5 to 16 ($\times 10^8$ cm^{-2}) [double-headed arrows in Fig. 2(a)], then saturates to a value at around Φ^* [downward arrows in Fig. 2(b)] and finally plummets due to excess irradiation. As a result, in Fig. 2(a), we find trapezoid-shaped $J_c^{sf}(\Phi)$ profiles that have a plateau in the middle of each profile. In addition, in the 84-MeV data in Fig. 2(a), a "stairstep"-like additional J_c^{sf} enhancement appears, namely, a sectional uplift of the plateau in the Φ range of 3 to 10 ($\times 10^{10}$ cm^{-2}) immediately before the J_c^{sf} drop [shaded area in Fig. 2(a)].

As we extensively discussed in Ref. 1, the characteristic J_c^{sf} saturation when Φ was increased was well reproduced by the so-called vortex-accommodation-probability-formalism. Dependence of the location of saturation on the film thickness t indicates that the vortex-accommodation efficiency depends on t. The stairstep observation suggests presence of distinct pinning phases in a single-vortex/1D-pin system depending on pin spacing and applied current density. These novel findings obtained near $J_c^{sf} \sim 0.1J_0$ at

[1]National Institute of Advanced Industrial Science and Technology (AIST)
[2]Japan Atomic Energy Agency (JAEA)

77 K will contribute to understanding the mechanism of J_c^{sf} in YBCO at large thermal fluctuations.

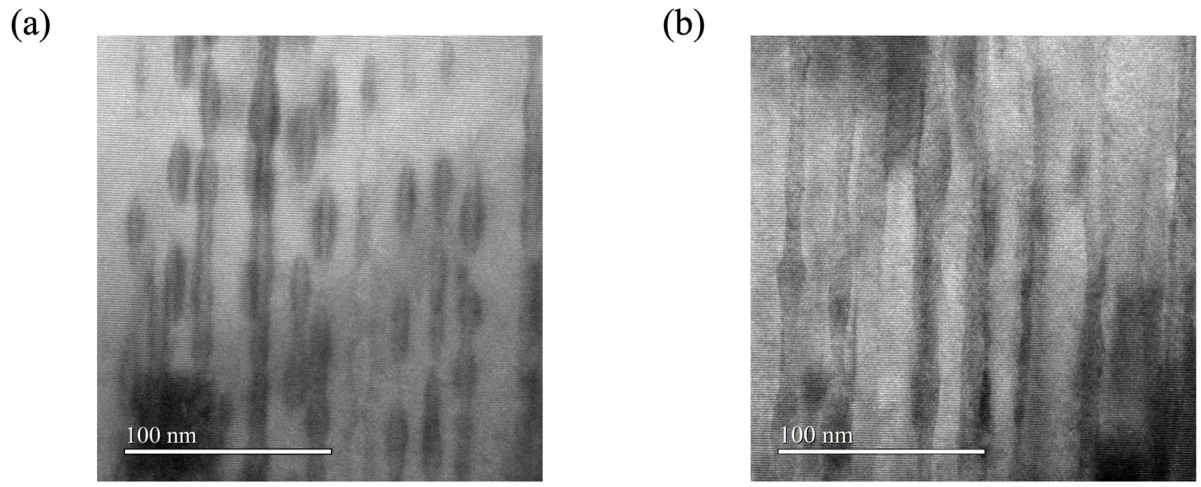

Fig.1. Cross-sectional TEM images of YBCO films irradiated with (a) 84- and (b) 300-MeV Au ions [1].

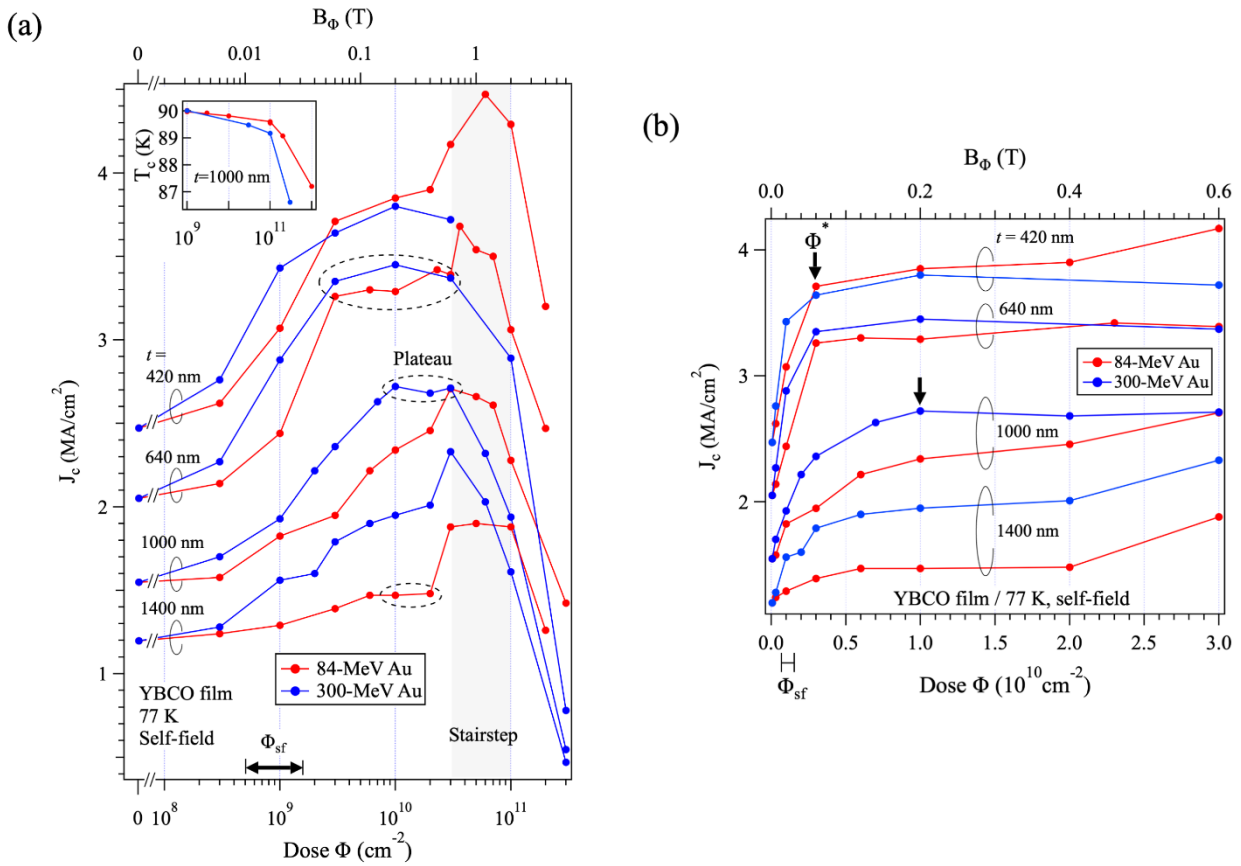

Fig. 2. (a) Dose dependence of J_c for our Au-irradiated YBCO films. Examples of the plateau are indicated by dashed ellipses. The shaded area is the dose region of a sectional uplift of the plateau ("stairstep") in the 84-MeV data. The inset shows the dose-dependence of T_c for samples with t =1000 nm. (b) The same data as (a) plotted in linear scale and enlarged in the range below 3×10^{10} cm^{-2} [1].

Reference

[1] H. Matsui et al., Phys. Scr. 100 (2025) 075917. [DOI: 10.1088/1402-4896/adde93]

5.4 Controlling the surface resistance of sapphire by nickel ion implantation for improving surface flashover voltage

A. Ogura, T. Kaneko, S. Ishii, S. Katagiri

One approach to improving the surface flashover voltage of insulators used to support conductors in vacuum is to coat the surface of the insulator with a semi-conductive layer [1]. This technique facilitates the dissipation of surface charge and suppresses secondary electron emission, thereby enhancing the breakdown voltage. Regarding the semiconductivity of insulators, there have been reports demonstrating that the implantation of Ni ions into sapphire substrates can achieve volume resistivity dependent on ion fluence [2]. Based on this concept, the present study aims to control the surface resistance of sapphire substrates through Ni ion implantation.

Ni ions were implanted into c-plane (0001) sapphire substrates using the 1 MV Tandetron accelerator. Ni ions were selected due to their demonstrated performance in prior studies and their relatively high beam current compared to other ion species. The implantation energy was set at 300 keV, which is the minimum energy at which the accelerator can operate stably. However, TRIM simulations revealed that at 300 keV, the Ni ions do not accumulate sufficiently near the surface. To overcome this issue, two approaches were employed to localize the implanted ions closer to the surface:

1. A titanium (Ti) film was deposited on the sapphire surface prior to ion implantation, and subsequently removed after implantation. The Ni ions lose energy while passing through the Ti layer, causing the implantation peak to occur at the Ti/sapphire interface.
2. After ion implantation, reactive ion etching (RIE) was performed to remove the surface layer down to the ion-implanted region. This method enables the ion distribution peak to be exposed at the surface region.

This report focuses on the method involving Ti film deposition for controlling the surface resistance.

The samples used in this study had dimensions of 4 mm × 47 mm, with the ion irradiation area set to 4–8 mm. Ti thin films were deposited using a DC magnetron sputtering method. Surface resistance measurements were carried out using a vacuum chamber system developed in our laboratory. To quantitatively evaluate the depth distribution of the implanted metal ions, secondary ion mass spectrometry (SIMS) was employed.

As a preliminary step, a Ti film was deposited on a sapphire substrate and subsequently removed without ion irradiation. Current-voltage measurements were then conducted to assess any potential influence of residual Ti on the resistance. The Ti film was removed using hydrogen peroxide solution. Since only current at the noise level was detected, it was confirmed that the deposition and removal of the Ti film did not affect the surface resistance.

The irradiation samples had Ti film thicknesses of 220 nm and 194 nm for the first and second trials, respectively. Ion implantation distributions for each Ti thickness were simulated using TRIM (Transport of Ions in Matter), and the Ni ion fluence was determined based on the simulation results. The simulated ratio of fluence between the Ti layer and the sapphire substrate was approximately 4:1 for the 220 nm film and

2:1 for the 194 nm film. Accordingly, to achieve the target fluence within the sapphire substrate, the total implantation fluence was set to five times the target value for the 220 nm Ti film and three times for the 194 nm Ti film.

As shown in Fig. 1, a linear relationship between fluence and surface resistance was observed on a log–log plot. This trend is consistent with previous studies, confirming the reproducibility of the results [1]. Although the thicknesses of the Ti films differed, similar slopes were obtained. However, the surface resistance values at the same fluence varied between the two cases. This discrepancy is likely due to the horizontal axis representing only the fluence of implanted Ni ions, without accounting for the influence of the Ti film. Numerical simulations using TRIM revealed that, during passage through the Ti film, the incident Ni ions induced a knock-on effect, displacing a significant number of Ti atoms and embedding them into the surface region of the sapphire substrate. Therefore, it is necessary to revise the horizontal axis of Fig. 1 to account not only for the implanted Ni ions but also for the Ti atoms displaced and embedded into the substrate. For this purpose, quantitative analysis of each element was conducted using SIMS.

Figures 2(a) and (b) show the depth profiles of Ti and Ni obtained from SIMS analysis for samples with Ti film thicknesses of 220 nm (fluence: 5.0×10^{15} cm^{-2}) and 194 nm (fluence: 8.0×10^{15} cm^{-2}), respectively. For Ni, no significant differences were observed between the two Ti film thicknesses. In the case of Ti, a higher concentration was observed at depths beyond 50 nm for the 220 nm film compared to the 194 nm film. It may result from in-plane variation or from characteristic atomic knock-on effects associated with SIMS analysis. In any case, near the surface, the concentration of Ti exceeded that of Ni, which is consistent with the TRIM simulation results that account for the knock-on effect. When the horizontal axis was corrected to include the total fluence of both Ni and Ti ions, all data points aligned nearly on a single straight line (data not shown). This indicates that the surface resistance of sapphire is determined by the total fluence of all implanted ions.

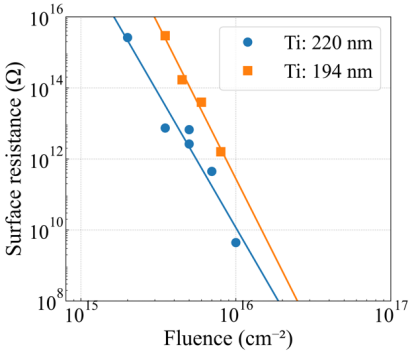

Fig. 1. Fluence dependence of surface resistance for samples implanted with Ni ions through Ti films of 220 nm and 194 nm thickness.

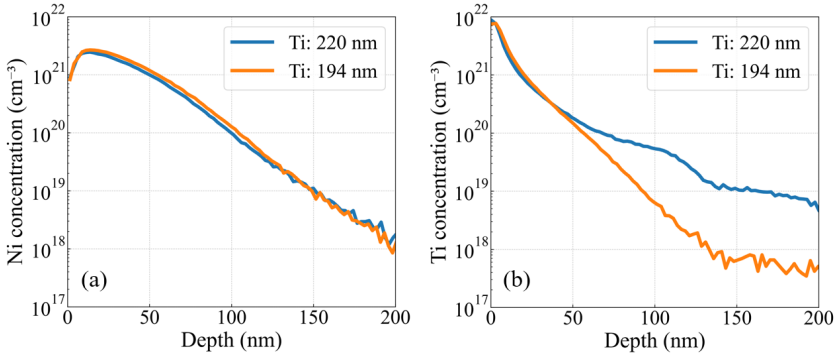

Fig. 2. Depth profiles of (a) Ni and (b) Ti concentrations obtained by SIMS analysis for samples with Ti films of 220 nm and 194 nm thickness.

References

[1] T. S. Sudarshan et al., IEEE Trans. Electr. Insul. E-11 (1976) 32.

[2] T. Kobayashi et al., Nucl. Instr. Meth. Phys. Res. B 116 (1996) 187.

5.5 Impact of gate oxide formation process on SEGR tolerance in SiC-MOS capacitors

K. Kobayashi[1,2], M. Takahashi[3], M. Iwata[3], H. Shindou[3], A. Shima[1], S. Harada[2]

Silicon carbide (SiC) has attracted significant attention as a next-generation semiconductor material for power electronics due to its superior properties, including a wider bandgap and higher thermal conductivity than those of conventional silicon. These characteristics enable SiC-based metal-oxide-semiconductor (MOS) devices to achieve low conduction losses and high-efficiency power conversion, making them suitable for electric vehicles, renewable energy, and other power conversion systems [1]. However, ensuring reliability is especially important for high-altitude and space-based systems, where devices are exposed to high-energy cosmic radiation. In such environments, high-energy particles like cosmic rays and neutrons can interact with semiconductors, inducing single event effects (SEE) [2]. In power devices, single event burnout (SEB) and single event gate rupture (SEGR), which are included in SEE, are the primary causes of reliability degradation. SEB has been extensively studied in silicon devices, where activation of parasitic bipolar transistors in MOSFETs is a key factor. SEGR involves catastrophic breakdown of the gate oxide and is potentially more severe in SiC devices due to higher electric fields at the gate. To ensure SiC device reliability in radiation-prone environments, understanding SEGR mechanisms is essential. Therefore, it is important to understand the SEGR mechanism in SiC devices and to improve their SEGR tolerance. In this study, the impact of the gate oxide formation process on SEGR tolerance was investigated through heavy ion irradiation tests of fabricated SiC-MOS capacitors.

Figure 1 shows the cross-sectional view of the fabricated SiC-MOS capacitors. SEGR is a phenomenon that occurs when a MOSFET is in a depletion state. To mitigate electric field crowding at the gate edge, a capacitor structure incorporating a junction termination extension (JTE) was fabricated. Electrodes corresponding to the gate, source, and drain terminals of a MOSFET were implemented as gate, body, and substrate (Sub) electrodes, respectively. The SiC-MOS capacitors were fabricated on 4H-SiC substrates. The epitaxial layer was 10 μm thick with a donor concentration of 1×10^{16} cm^{-3}. The gate oxide layer was 50 nm thick and formed by dry oxidation. To investigate the influence of the gate oxide formation process on SEGR tolerance, three types of samples were prepared with varying durations of post-oxidation annealing in nitric oxide (NO): no annealing, 10 minutes, and 60 minutes. The irradiation tests were carried out using a 72 MeV $^{32}S^{11+}$ beam from the UTTAC 6MV tandem accelerator under the condition of beam incidence perpendicular to the surface of the device chip. In this case, LET is 16.5 MeV/(mg/cm^2).

Figure 2 shows the measurement sequence. During the irradiation, the gate leakage current was continuously monitored and recorded. The applied voltage was increased stepwise from an initial voltage V_s = 25 V, in increments of V_{step} = 25 V, until the leakage current density exceeded a predefined threshold. The

[1]Hitachi, Ltd.
[2]National Institute of Advanced Industrial Science and Technology
[3]Japan Aerospace Exploration Agency

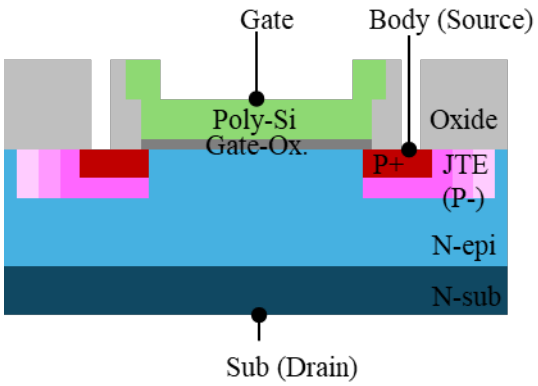

Fig. 1. Cross sectional view of the fabricated SiC-MOS capacitor.

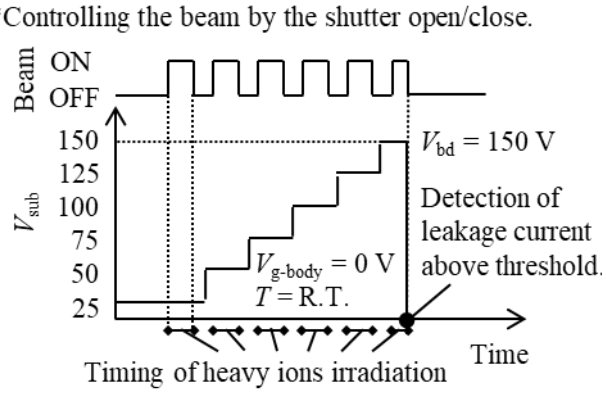

Fig. 2. Measurement sequence of the irradiation test.

ion flux and fluence at each voltage step were set to approximately 5,000 $cm^{-2}\cdot s^{-1}$ and 300,000 cm^{-2}, respectively.

Figure 3 shows the time evolution of the gate leakage current for the NO-60 minutes sample, with overlaid waveforms corresponding to each V_{sub}. The gate leakage current is stable between 25 V and 200 V; however, a sharp increase of the current was observed at 225 V. This sudden rise in leakage current is interpreted as the onset of dielectric breakdown. Accordingly, the drain voltage at which this abrupt increase occurred is defined as the breakdown voltage.

Figure 4 shows the relationship between the breakdown voltage and the post-oxidation annealing (POA) time. It is evident that the breakdown voltage increases with longer POA times. This suggests that POA enhances the device's tolerance to holes generated by the ion irradiation. Although further investigation is required to clarify the underlying mechanism, one possible explanation is that NO annealing reduces the hole trap density at the SiC/SiO_2 interface [3], thereby altering the electric field distribution at the interface.

This study was implemented under a joint research project of Tsukuba Power Electronics Constellations (TPEC).

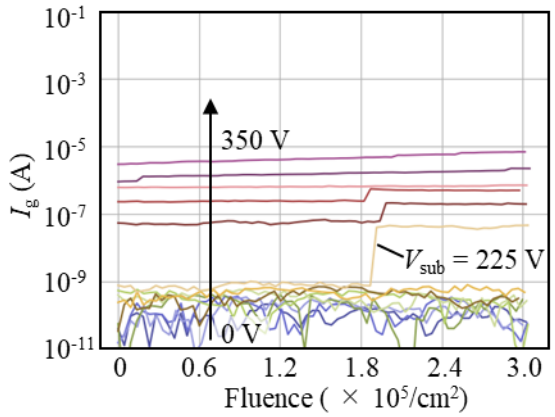

Fig. 3. Time dependence of gate leakage current.

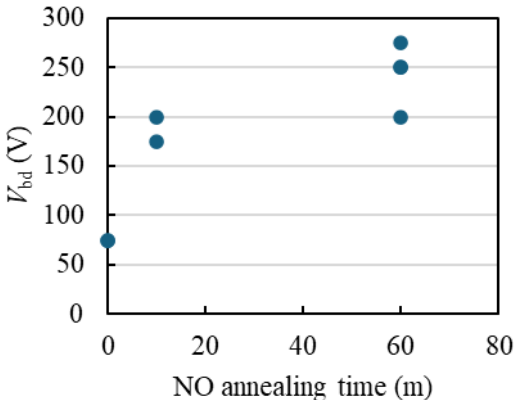

Fig. 4. Dependence of breakdown voltage on annealing time.

References

[1] T. Kimoto, Jpn. J. Appl. Phys. 54.4 (2015) 040103.

[2] J. L. Titus, IEEE Transactions on nuclear science 60.3 (2013) 1912.

[3] M. Hayashi et al., Jpn. J. Appl. Phys. 57, 4S (2018) 04FR15.

6.

LIST OF PUBLICATIONS AND PRESENTATIONS

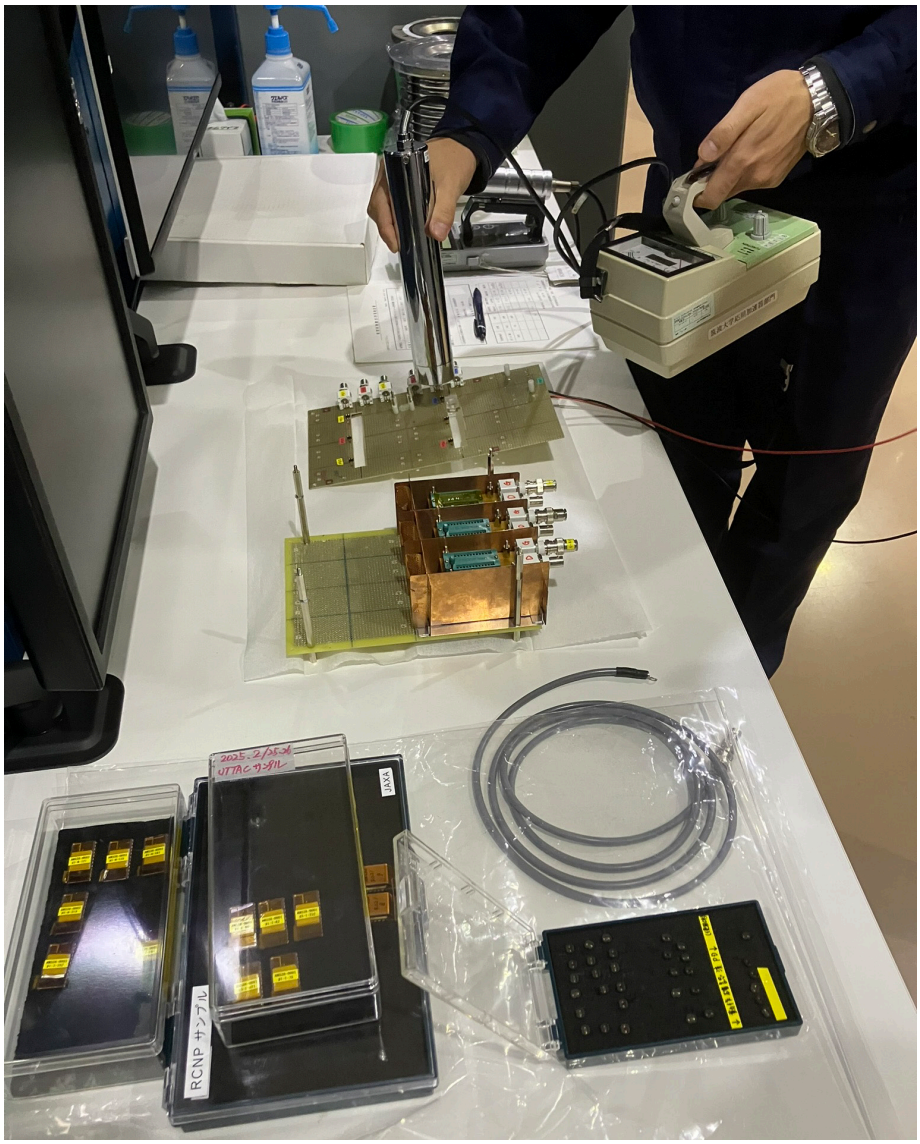

Confirmation of Residual Radioactivity after Ion Beam Irradiation by the 6MV Tandem Accelerator

6.1 Peer-reviewed and proceedings papers

1. A. Uedono, R. Hasunuma, K. Onishi, H. Kitagawa, F. Inoue, K. Michishio, N. Oshima, “Annealing behaviors of open spaces and gas desorption in chemical vapor deposited SiO_2 studied with monoenergetic positron beams”, J. Appl. Phys. 136 (2024) 045304(1-8). [DOI: 10.1063/5.0217760]

2. A. Uedono, C. Fleischmann, J.-P. Soulié, M. Ayyad, J.E. Scheerder, C. Adelmann, J. Uzuhashi, T. Ohkubo, K. Michishio, N. Oshima, S. Ishibashi, “Vacancy-Type Defects and Oxygen Incorporation in NiAl for Advanced Interconnects Probed by Monoenergetic Positron Beams and Atom Probe Tomography”, ACS Appl. Elect. Mat. 6 (2024) 5894. [DOI: 10.1021/acsaelm.4c00877]

3. S.F. Chichibu, K. Shima, A. Uedono, S. Ishibashi, H. Iguchi, T. Narita, K. Kataoka, R. Tanaka, S. Takashima, K. Ueno, M. Edo, H. Watanabe, A. Tanaka, Y. Honda, J. Suda, H. Amano, T. Kachi, T. Nabatame, Y. Irokawa, Y. Koide, “Impacts of vacancy complexes on the room-temperature photoluminescence lifetimes of state-of-the-art GaN substrates, epitaxial layers, and Mg-implanted layers”, J. Appl. Phys. 135 (2024) 185701(1-20). [DOI: 10.1063/5.0201931]

4. K. Onishi, H. Kitagawa, S. Teranishi, A. Uedono, F. Inoue, “Temporary direct bonding by low temperature deposited SiO_2 for chiplet applications”, ACS Appl. Elect. Mat. 6 (2024) 24496. [DOI: 10.1021/acsaelm.4c00114]

5. A. Uedono, R. Tanaka, S. Takashima, K. Ueno, M. Edo, K. Shima, S.F. Chichibu, J. Uzuhashi, T. Ohkubo, S. Ishibashi, K. Sierakowski, M. Bockowski, “Vacancy-type defects and their trapping/detrapping of charge carriers in ion-implanted GaN studied by positron annihilation”, Phys. Stat. Sol. B 261 (2024) 240060(1-10). [DOI: 10.1002/pssb.202400060]

6. K.M. Senados, M.S.L. Lima, T. Aizawa, I. Ohkubo, T. Baba, A. Uedono, T. Sakurai, T. Mori, “Influence of Ge to the formation of defects in epitaxial $Mg_2Sn_{1-x}Ge_x$ thermoelectric thin films”, Jpn. J. Appl. Phys. 63 (2024) 02SP40(1-6). [DOI: 10.35848/1347-4065/ad1259]

7. T. Kimura, H. Shimazu, K. Kataoka, K. Itoh, T. Narita, A. Uedono, Y. Tokuda, D. Tanaka, S. Nitta, H. Amano, D. Nakamura, “Impurity reduction in lightly doped n-type gallium nitride layer grown via halogen-free vapor-phase epitaxy”, Appl. Phys. Lett. 124 (2024) 052104(1-6). [DOI: 10.1063/5.0191774]

8. K. Shima, K. Kurimoto, Q. Bao, Y. Mikawa, M. Saito, D. Tomida, A. Uedono, S. Ishibashi, T. Ishiguro, S.F. Chichibu, “Improved midgap recombination lifetimes in GaN crystals grown by the low pressure acidic ammonothermal method”, Appl. Phys. Lett. 124 (2024) 181103. [DOI: 10.1063/5.0208853]

9. C. Fleischmann, A. Uedono, J.E. Scheerder, J.-P. Soulié, S. Park, C. Adelmann, Z. Tőkei, “Resolving nanoscale composition fluctuations and defects in advanced interconnects: a crucial step to comprehend thin film resistivity”, IEEE Int. Interconnect Tech. Conf. (IITC), 2024. [DOI: 10.1109/IITC61274.2024.10732594]

10. S. Ebiko, S. Iacovo, S.-A. Chew, B. Zhang, A. Uedono, F. Inoue, “Exploring bonding mechanism of SiCN for hybrid bonding”, IEEE 74th Elect. Components & Tech. Conf. (ECTC), (2024) 1953. [DOI: 10.1109/ECTC51529.2024.00331]

11. K. Mihara, T. Hare, H. Sakai, S. Aoki, T. Terada, M. Murugesan, H. Hashimoto, H. Kino, T. Tanaka, T. Fukushima, F. Inoue, A. Uedono, “D2W hybrid bonding system achieving high-accuracy and high-throughput with minimal configurations”, IEEE 74th Elect. Components & Tech. Conf. (ECTC), (2024) 420. [DOI: 10.1109/ectc51529.2024.00074]

12. Y. Wakiyama, M. Matsumura, T. Matsunaka, S. Hirao, K. Sasa, “Riverine ^{129}I dynamics during high flow events on the Abukuma River in Fukushima”, Appl. Geochem. 173 (2024) 106134. [DOI: 10.1016/j.apgeochem.2024.106134]

13. H. Shen, D. Chen, L. Wang, Z. Li, J. Tang, G. Zhang, L. Qi, K. Wu, X. Han, H. Ouyang, Y. He, N. Wang, X. Sun, M. He, K. Sasa, S. Jiang, “Experimental conditions for ^{14}C graphite preparation at the GXNU LAB, CHINA”, Radiocarbon 66 (2024) 1322. [DOI: 10.1017/RDC.2024.44]

14. H. Shen, L. Qi, H. Ouyang, X. Han, G. Zhang, D. Chen, K. Wu, J. Tang, L. Wang, N. Wang, X. Sun, M. He, K. Sasa, J. Shan, “Sample preparation system for carbonate and DIC in water at the GXNU-AMS LABORATORY”, Radiocarbon 66 (2024) 1310. [DOI: 10.1017/RDC.2024.65]

15. H. Kudo, H. Naramoto, M. Sataka, S. Ishii, K. Sasa, S. Tomita, “Transmission ERDA of ubiquitous deuterium in H-containing materials”, Nucl. Instrum. Methods Phys. Res. B 554 (2024) 165404. [DOI: 10.1016/j.nimb.2024.165404]

16. S. Shiki, G. Fujii, S. Tomita, K. Sasa, “Particle induced X-ray emission apparatus utilizing superconducting tunnel junction detector”, Nucl. Instrum. Methods Phys. Res. B 554 (2024) 165451. [DOI: 10.1016/j.nimb.2024.165451]

17. Y. Shiina, R. Kinoshita, S. Funada, M. Matsuda, M. Imai, K. Kawatsura, M. Sataka, K. Sasa, T. Kaneko, S. Tomita, “Vicinage effect on the yield of convoy electrons emitted from thin carbon foil induced by the penetration of 3.5 MeV/atom C_n^+ ions”, Phys. Rev. A 110 (2024) 062826. [DOI: 10.1103/PhysRevA.110.062826]

18. I. Harayama, Y. Hirose, D. Sekiba, “Cathode shape dependence of gas ionization chamber on electron collection in ΔE-E telescope ERDA”, Nucl. Instrum. Methods Phys. Res. B 554 (2024) 165435 (1-6). [DOI: 10.1016/j.nimb.2024.165435]

19. T. Ozawa, Y. Sugisawa, Y. Komatsu, R. Shimizu, T. Hitosugi, D. Sekiba, K. Yamauchi, I. Hamada, K. Fukutani, “Isotope-dependent site occupation of hydrogen in epitaxial titanium hydride nanofilms”, Nat. Commun. 15 (2024) 9558. [DOI: 10.1038/s41467-024-53838-6]

20. Y. Abe, Y. Yamaguchi, M. Wakasugi, H. Baba, T. Fujinawa, Z. Ge, A. Goto, S. Michimasa, H. Miura, T. Moriguchi, D. Nagae, S. Naimi, J. Ohnishi, S. Omika, S. Ota, A. Ozawa, F. Suzaki, H. Suzuki, S. Suzuki, N. Tadano, A. Tokuchi, T. Uesaka, K. Wakayama, T. Yamaguchi, Y. Yano, “Performance of a precise isochronous magnetic field over a wide momentum range in the Rare-RI Ring”, Nucl. Instrum. Methods Phys. Res. A 1072 (2025) 170083. [DOI: 10.1016/j.nima.2024.170083]

21. G. Hudson-Chang, S. Naimi, Y. Abe, R. Crane, H.F. Li, T. Moriguchi, M. Mukai, D. Nagae, A. Ozawa, S. Suzuki, T. Uesaka, T. Yamaguchi, Y. Yamaguchi, A. Yano, “Development of a low energy loss micro-channel plate based position-sensitive detector for the Rare Radio-Isotope Ring”, Nucl. Instrum. Methods Phys. Res. A 1069 (2024) 169980. [DOI: 10.1016/j.nima.2024.169980]

22. T. Moriguchi, R. Kagesawa, A. Ozawa, W. Horiuchi, Y. Abe, M. Amano, D. Kamioka, A. Kitagawa, M. Mukai, D. Nagae, M. Sakaue, S. Sato, B.H. Sun, S. Suzuki, T. Suzuki, T. Yamaguchi, A. Yano, K. Yokota, “Investigation of total reaction cross sections for proton-dripline nuclei ^{17}F and ^{17}Ne on a proton target”, Phys. Rev. C 110 (2024) 014607. [DOI: 10.1103/PhysRevC.110.014607]

23. D. Nagae, S. Omika, Y. Abe, Y. Yamaguchi, F. Suzaki, K. Wakayama, N. Tadano, R. Igosawa, K. Inomata, H. Arakawa, K. Nishimuro, T. Fujii, T. Mitsui, T. Yamaguchi, T. Suzuki, S. Suzuki, T. Moriguchi, M. Amano, D. Kamioka, A. Ozawa, S. Naimi, Z. Ge, Y. Yanagisawa, H. Baba, S. Michimasa, S. Ota, G. Lorusso, Yu.A. Litvinov, M. Wakasugi, T. Uesaka, Y. Yano, “Isochronous mass spectrometry at the RIKEN Rare-RI Ring facility”, Phys. Rev. C 110 (2024) 014310. [DOI: 10.1103/PhysRevC.110.014310]

24. S. Ishitani, M. Fukuda, M. Fukutome, G. Takayama, R. Taguchi, K. Watanabe, M. Tanaka, T. Ohtsubo, N. Noguchi, K. Takatsu, Y. Ota, T. Suzuki, T. Yamaguchi, M. Kanda, N. Shinozaki, D. Nishimura, H. Takahashi, S. Sugawara, C. Une, A. Ozawa, T. Moriguchi, N. Kaname, A. Yano, A. Moriyama, S. Sato, S. Fukuda, A. Kitagawa, “Charge-Changing Cross Sections for Mirror Nuclear Pair, ^{22}Ne and ^{22}Mg”, Interactions 45 (2024) 65. [DOI: 10.1007/s10751-024-01874-5]

25. R. Taguchi, M. Fukuda, G. Takayama, M. Fukutome, M. Tanaka, K. Takatsu, D. Nishimura, H. Takahashi, S. Sugawara, M. Mihara, Y. Kimura, K. Watanabe, T. Ohtsubo, M. Takechi, M. Ogose, N.

Noguchi, Y. Kobayashi, Y. Tazawa, N. Shindo, T. Izumikawa, C. Fukushima, T. Suzuki, T. Yamaguchi, A. Ozawa, T. Moriguchi, A. Yano, S. Sato, S. Fukuda, A. Kitagawa, “Charge-Changing Cross Sections and Charge Radii of B, C, and N Isotopes”, Interactions 45 (2024) 112.
[DOI: 10.1007/s10751-024-01943-9]

26. D. Freire-Fernández, W. Korten, R.J. Chen, S. Litvinov, Yu.A. Litvinov, M.S. Sanjari, H. Weick, F.C. Akinci, H.M. Albers, M. Armstrong, A. Banerjee, K. Blaum, C. Brandau, B.A. Brown, C.G. Bruno, J.J. Carroll, X. Chen, C.J. Chiara, M.L. Cortes, S.F. Dellmann, I. Dillmann, D. Dmytriiev, O. Forstner, H. Geissel, J. Glorius, A. Görgen, M. Górska, C.J. Griffin, A. Gumberidze, S. Harayama, R. Hess, N. Hubbard, K.E. Ide, Ph.R. John, R. Joseph, B. Jurado, D. Kalaydjieva, Kanika, F.G. Kondev, P. Koseoglou, G. Kosir, Ch. Kozhuharov, I. Kulikov, G. Leckenby, B. Lorenz, J. Marsh, A. Mistry, A. Ozawa, N. Pietralla, Zs. Podolyák, M. Polettini, M. Sguazzin, R.S. Sidhu, M. Steck, Th. Stöhlker, J.A. Swartz, J. Vesic, P.M. Walker, T. Yamaguchi, R. Zidarova, “Measurement of the Isolated Nuclear Two-Photon Decay in ^{72}Ge”, Phys. Rev. Lett. 133 (2024) 022502. [DOI: 10.1103/PhysRevLett.133.022502]

6.2 Reviews and books

1. 小野寺礼尚, 喜多英治, “実学講座　金属材料実験の手引き, 2.特性の計測評価, 2-3 磁気特性の計測と解析, 2-3-2 磁気測定の応用：動的磁化測定 (測定)”, まてりあ 63 (2024) 842.

6.3 Poster and oral presentations

1. 喜多英治, 南 麟太朗, 柳原英人, “メスバウアー分光を利用した反応性スパッタによる鉄酸化物薄膜成長の評価”, 第 23 回メスバウアー分光研究会シンポジウム, 姫路市
(2024 年 4 月 26–27 日).

2. R. Minami, E. Kita, S. Sharmin, H. Yanagihara, “Monitoring Iron Oxide Thin Film Growth by Plasma Emission Spectrometry in Reactive Sputtering Process”, IEEE Int. Magnetics Conf. (INTERMAG 2024) Rio de Janeiro, Brazil (May 5–10, 2024).

3. S. Ebiko, S. Iacovo, S.-A. Chew, B. Zhang, A. Uedono, F. Inoue, “Exploring bonding mechanism of SiCN for hybrid bonding”, IEEE 74th Elect. Components & Tech. Conf. (ECTC), Colorado, USA
(May 28–31, 2024).

4. K. Mihara, T. Hare, H. Sakai, S. Aoki, T. Terada, M. Murugesan, H. Hashimoto, H. Kino, T. Tanaka, T. Fukushima, F. Inoue, A. Uedono, “D2W hybrid bonding system achieving high-accuracy and high-

throughput with minimal configurations", IEEE 74th Elect. Components & Tech. Conf. (ECTC), Colorado, USA (May 28–31, 2024). (Invited Talk)

5. C. Fleischmann, A. Uedono, J.E. Scheerder, J.-P. Soulié, S. Park, C. Adelmann, Z. Tőkei, "Resolving nanoscale composition fluctuations and defects in advanced interconnects: a crucial step to comprehend thin film resistivity", 2024 IEEE Int. Interconnect Tech. Conf. (IITC), San Jose, USA (Jun. 3–6, 2024). (Invited Talk)

6. 森口哲朗, 小沢 顕, 大和良広, 冨田啓介, 矢野朝陽, H. Zhang, 関 優也, 松本 樹, "筑波大学タンデム加速器施設における偏極イオン源を用いた不安定核の核モーメント測定", 第 36 回タンデム加速器及びその周辺技術の研究会, 理化学研究所 和光キャンパス, 和光市 (2024 年 6 月 27–28 日).

7. 吉田哲郎, 石井 聡, 高橋 努, 大和良広, 松村万寿美, 中沢智幸, 森口哲朗, 笹 公和, "筑波大学タンデム加速器施設の現状", 第 36 回タンデム加速器及びその周辺技術の研究会, 理化学研究所 和光キャンパス, 和光市 (2024 年 6 月 27–28 日).

8. 笹 公和, 左高正雄, 楢本 洋, 工藤 博, 吉田哲郎, 高橋 努, "筑波大学における放射線耐性試験のための宇宙利用素子照射試験装置の開発", 第 36 回タンデム加速器及びその周辺技術の研究会, 理化学研究所 和光キャンパス, 和光市 (2024 年 6 月 27–28 日).

9. 吉田哲郎, 大和良広, 笹 公和, 広田克也, 古坂道弘, "タンデム静電加速器に関する VR を利用した教育用教材の開発", 第 21 回日本加速器学会年会, 山形テルサ, 山形市 (2024 年 7 月 31 日–8 月 3 日)

10. 古坂道弘, 広田克也, 池松克昌, 池田 進, 福田将史, 設楽哲夫, 岩下芳久, 山本昌志, 城野哲, 矢野博明, 笹 公和, 大和良広, 吉田哲郎, O'Rourke Brian, 林 憲志, 太田紘志, 清水康平, 田中慎一郎, 加藤政博, "メタバース加速器博物館による人材育成と広報", 第 21 回日本加速器学会年会, 山形テルサ, 山形市 (2024 年 7 月 31 日–8 月 3 日).

11. 笹 公和, 石井 聡, 高橋 努, 大和良広, 吉田哲郎, 中沢智幸, 松村万寿美, 森口哲朗, "筑波大学タンデム加速器施設の現状報告", 第 21 回日本加速器学会年会, 山形テルサ, 山形市 (2024 年 7 月 31 日–8 月 3 日).

12. 森口哲朗, 景澤怜央, 小沢 顕, 堀内 渉, 阿部康志, 天野将道, 上岡大起, 北川敦志, 向井もも, 長江大輔, 坂上 護, 佐藤眞二, B.H. Sun, 鈴木伸司, 鈴木 健, 山口貴之, 矢野朝陽, 横田健次郎, "陽子ドリップライン核 ^{17}F, ^{17}Ne の固体水素標的を用いた反応断面積測定", 日本物理学会第 79 回年次大会, 北海道大学, 札幌市（2024 年 9 月 16–19 日).

13. 岸奈津子, 小林 成, 山本和樹, 清水亮太, 一杉太郎, 関場大一郎, “^{6}Li トレーサーを用いた簡易電池のオペランド NRA”, 日本物理学会第 79 回年次大会, 北海道大学, 札幌市 (2024 年 9 月 16–19 日).

14. 市川 豪, 不破康裕, 長谷川拓郎, 広田克也, 星野公邦, 細川律也, 猪野 隆, 岩下芳久, 北口雅暁, 古賀 淳, 松崎 俊, 三島賢二, 茂木駿紀, 音野瑛俊, 關 義親, 関場大一郎, 嶋 達志, 清水春樹, 清水裕彦, 角 直幸, 角野浩史, 谷田征輝, 山下 了, 吉岡瑞樹, “J-PARC/BL05 における中性子寿命測定実験：NaI 検出器を用いた γ 線背景事象の測定と CO_2 ガスによる物理測定解析”, 日本物理学会第 79 回年次大会, 北海道大学, 札幌市 (2024 年 9 月 16–19 日).

15. 茂木駿紀, 不破康裕, 長谷川拓郎, 広田克也, 星野公邦, 細川律也, 市川 豪, 猪野 隆, 岩下芳久, 北口雅暁, 古賀 淳, 松崎 俊, 三島賢二, 音野瑛俊, 關 義親, 関場大一郎, 嶋 達志, 清水春樹, 清水裕彦, 角 直幸, 角野浩史, 谷田征輝, 山下 了, 吉岡瑞樹, “J-PARC/BL05 における中性子寿命測定実験：2023 年までの解析結果”, 日本物理学会第 79 回年次大会, 北海道大学, 札幌市 (2024 年 9 月 16–19 日).

16. 笹 公和, 松村万寿美, 吉田哲郎, 高橋 努, "^{36}Cl の加速器質量分析における妨害同重体 ^{36}S のイオン源での抑制”, 第 85 回応用物理学会秋季学術講演会, 朱鷺メッセ, 新潟市 (2024 年 9 月 16–20 日).

17. 西塚魁人, 笹 公和, 高橋 努, 松村万寿美, 浅井志保, 高久雄一, 山﨑信哉, 末木啓介, V. Kanivets, 坂口 綾, “水環境中における有機・無機よう素同位体定量法の検討ーチョルノービリ原子力発電所冷却池のよう素同位体”, 第 85 回応用物理学会秋季学術講演会, 朱鷺メッセ, 新潟市 (2024 年 9 月 16–20 日).

18. 南 麟太朗, 喜多英治, 柳原英人, “反応性スパッタリングプロセス中に発生するプラズマ発光による成長中の酸化鉄薄膜の価数及び成膜速度予測”, 第 85 回応用物理学会秋期学術講演会, 朱鷺メッセ, 新潟市 (2024 年 9 月 16–20 日).

19. 小野寺礼尚, 喜多英治, 髙橋弘紀, “Fe 基アモルファス合金に対する磁場中低温焼鈍の効果”, 第 85 回応用物理学会秋期学術講演会, 朱鷺メッセ, 新潟市 (2024 年 9 月 16–20 日).

20. A. Yano, “Mass measurements of rare-radioactive isotopes with a unique storage ring”, INTERNATIONAL SCHOOL OF NUCLEAR PHYSICS: 45th Course: Nuclei in the Laboratory and in Stars, Erice, Sicily, Italy (Sep. 16–22, 2024).

21. 松中哲也, 田中さき, 小澤萌音, 熊本雄一郎, 猪股弥生, 笹　公和, 長尾誠也, “ヨウ素 129 を用いた北極海・南極海における多環芳香族炭化水素類の水平分布解析”, 2024 年度日本地球化学会第 71 回年会, 金沢大学・角間キャンパス, 金沢市 (2024 年 9 月 18–20 日).

22. T. Matsunaka, S. Tanaka, M. Ozawa, Y. Kumamoto, K. Sasa, S. Nagao, “Variation factor of polycyclic aromatic hydrocarbons in surface seawater in the Arctic Ocean during 2019–2022”, SETAC Asia-Pacific 14th Biennial Meeting, Tianjin, China (Sept. 21–25, 2024).

23. 吉田 剛, 渡邉瑛介, 山﨑翔太, 塩原良建, 石田正紀, 津金聖和, 松村万寿美, 松村 宏, 豊田晃弘, 中村 一, 三橋正裕, 山田正明, 大石晃嗣, 三浦太一, 笹 公和, “加速器質量分析法(AMS)による大型陽子加速器施設内の電源ケーブル被覆中 ^{36}Cl の定量”, 日本放射化学会第 68 回討論会, 静岡市 (2024 年 9 月 23–25 日).

24. A. Uedono, C. Fleischmann, J.-P. Soulie, M. Ayyad, J.E. Scheerder, C. Adelmann, J. Uzuhashi, T. Ohkubo, K. Michishio, N. Oshima, S. Ishibashi, “Point Defects in NiAl Interconnects Probed by Positron Annihilation Spectroscopy and Atom Probe Tomography”, Advanced Metallization Conf., Tokyo, Japan (Oct. 3–4, 2024). (Invited Talk)

25. 松村万寿美, 坂口 綾, 高橋 努, 吉田哲郎, 笹 公和, 松中哲也, “加速器質量分析法(AMS)を用いた雨水中の I-129 調査”, 日本アイソトープ協会令和 6 年度放射線安全取扱い部会年次大会, あがたの森文化会館, 松本市 (2024 年 10 月 17–18 日).

26. K. Sasa, M. Matsumura, T. Yoshida, T. Takahashi, “Improvement of Cl-36 measurements at the Tsukuba 6 MV AMS facility”, The 16th Int. Conf. on Accelerator Mass Spectrometry, Guilin, China (Oct. 20–26, 2024). (Invited Talk)

27. R. Mundo, M. Matsumura, A. Sakaguchi, T. Matsunaka, T. Nakanowatari, K. Sasa, T. Takahashi, Y. Taniuchi, “Reanalysis of the formation mechanism of the Cold Water Belt in the southern Okhotsk Sea using I-129 as chemical tracer”, The 16th International Conference on Accelerator Mass Spectrometry, Guilin, China (Oct. 20–26, 2024).

28. M. Matsumura, K. Sasa, T. Matsunaka, A. Sakaguchi, T. Takahashi, K. Sueki, “Iodine-129 deposition from atmosphere in the sample preparation rooms for AMS”, The 16th International Conference on Accelerator Mass Spectrometry, Guilin, China (Oct. 20–26, 2024).

29. M. Matsumura, K. Sasa, T. Matsunaka, R. Tomita, T. Takahashi, H. Matsuzaki, K. Sueki, “Distribution of I-129 in the terrestrial environment after the Fukushima Daiichi Nuclear Power Plant accident”, The 16th International Conference on Accelerator Mass Spectrometry, Guilin, China (Oct. 20–26, 2024).

30. T. Matsunaka, T. Inoue, N. Mutsuo, S. Inomata, Y. Kumamoto, M. Matsumura, T. Takahashi, A. Sakaguchi, K. Sasa, “Seawater circulation in the Indian and Southern Oceans traced by I-129”, The 16th International Conference on Accelerator Mass Spectrometry, Guilin, China (Oct. 20–26, 2024).

31. T. Matsunaka, K. Sasa, K. Sueki, M. Matsumura, T. Takahashi, H. Matsuzaki, “Study on the migration behaviour of Fukushima accident-derived I-129 from land area to the marine environment”, The 16th International Conference on Accelerator Mass Spectrometry, Guilin, China (Oct. 20–26, 2024).

32. K. Sasa, T. Takahashi, M. Matsumura, T. Matsunaka, A. Sakaguchi, “The 6 MV multi-nuclide AMS system at the University of Tsukuba: Status report after 10 years of operation”, The 16th International Conference on Accelerator Mass Spectrometry, Guilin, China (Oct. 20–26, 2024).

33. 松村万寿美, 坂口 綾, 高橋 努, 吉田哲郎, 笹 公和, 松中哲也, “加速器質量分析法(AMS)を用いた雨水中の I-129 調査”, 日本アイソトープ協会令和 6 年度放射線安全取扱い部会年次大会, あがたの森文化会館, 松本市 (2024 年 10 月 17–18 日).

34. A. Uedono, “Characterization of vacancy-type defects in semiconductor materials using positron annihilation spectroscopy”, National Inst. Mater. Sci./Univ. Tsukuba/National Chung Hsing Univ. Joint Workshop: Advanced Materials and Nanostructures for Future Science and Technologies, Taichung, Taiwan (Oct. 24, 2024). (Invited Talk)

35. 松井浩明, 山口 巌, 真部高明, 相馬 貢, 西島 元, 松本明善, “斜入射イオン照射による新奇超伝導ダイオード効果の発見”, 日本電子材料技術協会 第 61 回秋期講演大会, 物質・材料研究機構, つくば市 (2024 年 10 月 28–29 日).

36. S.F. Chichibu, K. Shima, A. Uedono, S. Ishibashi, H. Iguchi, T. Narita, K. Kataoka, R. Tanaka, S. Takashima, K. Ueno, M. Edo, H. Watanabe, A. Tanaka, Y. Honda, Jun Suda, H. Amano, T. Kachi, T. Nabatame, Y. Irokawa, Y. Koide, “Minority carrier capture coefficients of major midgap recombination centers in the state-of-the-art GaN substrates, epilayers, and Mg-implanted layers”, 12th Int. Workshop on Nitride Semiconductor, Hawaii, USA (Nov. 3–8, 2024).

37. S.F. Chichibu, K. Ohnishi, H. Watanabe, S. Nitta, Y. Honda, H. Amano, A. Uedono, S. Ishibashi, K. Shima, “Room-temperature photoluminescence lifetimes of Mg-doped p-type GaN layers grown by halide vapor phase epitaxy”, 12th Int. Workshop on Nitride Semiconductor, Hawaii, USA (Nov. 3–8, 2024).

38. 松村万寿美, 松中哲也, 坂口 綾, 高橋 努, 吉田哲郎, 笹 公和, “加速器質量分析法(AMS)を用いた雨水中の I-129 降下率と同位体比調査”, 日本質量分析学会同位体比部会 2024, ホテルサンバリー　アネックス, 別府市 (2024 年 11 月 18–20 日).

39. T. Moriguchi, M. Mukai, N. Kaname, A. Ozawa, S. Suzuki, Y. Abe, H. Arakawa, T. Fujii, D. Hamakawa, S. Harayama, S. Hosoi, Y. Inada, K. Inomata, R. Kagesawa, D. Kajiki, D. Kamioka, M. Kanda, A. Kitagawa, T. Kobayashi, D. Nagae, S. Naimi, K. Nishimuro, S. Omika, M. Otsu, M. Sakaue, S. Sato,

H. Seki, N. Shinozaki, T. Suzuki, K. Tomita, T. Yamaguchi, Y. Yamaguchi, A. Yano, K. Yokota, “Improvements of time-of-flight detector utilizing a thin foil and crossed static electric and magnetic fields”, The 11th International Conference on Nuclear Physics at Storage Rings (STORI’24), Huizhou, Guangdong, China (Nov. 18–22, 2024).

40. A. Yano, Y. Yamaguchi, A. Ozawa, T. Ohnishi, Y. Abe, N. Chandratakumar, G. Hudson-Chang, N. Imai, Y. Kikuchi, N. Kitamura, R. Kojima, J. Li, T. Moriguchi, D. Nagae, S. Nishizawa, F. Suzaki, K. Takiura, N. Tomioka, R. Tuchiya, M. Wakasugi, K. Watanabe, T. Yamaguchi, R. Yokoyama, H. Zhang, “Improvement of transmission efficiency of the Rare-RI Ring with vertical steering magnets”, The 11th International Conference on Nuclear Physics at Storage Rings (STORI’24), Huizhou, Guangdong, China (Nov. 18–22, 2024).

41. A. Uedono, K. Kawakami, T. Kuribara, R. Hasunuma, Y. Harashima, Y. Shigeta, Z. Ni, Y. Ruolin, H. Nakamura, A. Notake, T. Moriya, K. Michishio, S. Ishibashi, “Vacancy-type defects in thin HfO_2 layers probed by monoenergetic positron beams”, Int. Sym. on Semiconductor Manufacturing (ISSM2024), Tokyo, Japan (Dec. 9–10, 2024).

42. T. Moriguchi, “Advantages of spin-polarized fusion”, WPI-SKCM2 Winter School, Kyushu University (Dec. 9–20, 2024). (Invited Talk)

43. 上殿明良, “堂山先生と陽電子消滅”, 日本 MRS 堂山昌男先生追悼シンポジウム, 横浜市開港記念会館, 横浜市 (2024 年 12 月 18 日).（招待講演）

44. 三河美紗希, 森口哲朗, 笹 公和, 高橋 努, 松村万寿美, 吉田哲郎, 矢野朝陽, H. Zhang, 三井真音, 松本 樹, 小林颯人, 小沢 顕, “加速器質量分析で利用される長寿命核種を用いた不安定核ビーム開発の現状”, 第 13 回 停止・低速 RI ビームを用いた核分光研究会(SSRI), 九州大学, 福岡市 (2025 年 2 月 20–21 日).

45. A. Yano, “Present status of the Rare-RI Ring”, RIBF User Meeting 2025, Wako, Japan (Feb. 22–23, 2025).

46. 上殿明良, “陽電子消滅を用いた材料の欠陥，自由体積の検出”, 第 38 期 Computer Aided Materials and Molecular Design Forum (CAMM)フォーラム 本例会, 東京 (2025 年 3 月 7 日). (招待講演)

47. 三浦 輝, 松中哲也, 笹 公和, “原子力施設周辺と縁辺海・外洋における放射性ヨウ素の動態解明”, 金沢大学環日本海域環境研究センター共同研究成果報告会, 金沢大学, 金沢市 (2024 年 3 月 7–8 日).

48. 木村龍拓, 吉田 剛, 松村 宏, 松村万寿美, 笹 公和, 高橋 努, 吉田哲郎, 石田正紀, 渡邉瑛介, 津金聖和, 李 恩智, Bui Ngoc Thien, 塩原良建, 三橋正裕, 平野雄生, 中屋敷勇輔, 大石晃嗣, 栗田紗緒里, 中田実希, 佐瀬卓也, 八島 浩, ”加速器施設における電源ケーブル被覆中 ^{36}Cl の定量”, 第 26 回「環境放射能」研究会, 高エネルギー加速器研究機構, つくば市 (2025 年 3 月 12–14 日).

49. 笹 公和, 松村万寿美, 吉田哲郎, 高橋 努, “加速器質量分析による人為起源 ^{36}Cl の検出とその応用”, 第 72 回応用物理学会春季学術講演会, 東京理科大学, 野田市 (2025 年 3 月 14–17 日).

50. 小野寺礼尚, 喜多英治, 髙橋弘紀, “ Fe 基アモルファス合金のナノ結晶化組織に対する磁場中低温焼鈍の効果”, 第 72 回応用物理学会春期学術講演会 東京理科大学, 野田市 (2025 年 3 月 14–17 日).

51. 松崎晶斗, 三宅芙沙, 堀内一穂, 川村賢二, 木村勝彦, 松村万寿美, 松崎浩之, 森谷 透, 大藪幾美, 笹 公和, 高見勇楽, 武山美麗, 門叶冬樹, 山形武靖, “宇宙線生成核種を用いた紀元前 990 年頃の宇宙線変動の調査”, 第 72 回応用物理学会春季学術講演会, 東京理科大学, 野田市 (2025 年 3 月 14–17 日).

52. 笹 公和, ”筑波大学におけるタンデム加速器利用の現状と将来展望”, 令和 7 年度電気学会 全国大会, 明治大学中野キャンパス, 東京都 (2025 年 3 月 18–20 日).（招待講演）

53. T. Sakurai, S. Magallon, T. Aizawa, I. Ohkubo, A. Uedono, T. Mori, “Controlling Defects in Epitaxial Thin Film Growth of $Mg_2Sn_{1-x}Ge_x$ for Thermoelectric Device Applications”, TMS 154th Annual Meeting, Nevada, USA (Mar. 23–27, 2025). (Invited Talk)

54. 三河美沙希, 森口哲朗, 笹 公和, 高橋 努, 松村万寿美, 吉田哲郎, 矢野朝陽, H. Zhang, 三井真音, 松本 樹, 小林颯人, 小沢 顕, “宇宙線生成核種を用いた不安定核ビーム開発の現状”, 第 25 回 AMS シンポジウム (JAMS-25), つくば国際会議場, つくば市 (2025 年 3 月 25–26 日).

55. 佐久間光紀, 松村万寿美, 高橋 努, 吉田哲郎, 笹 公和, “加速器質量分析を用いた ^{129}I 用 NIST 標準試料の検定”, 第 25 回 AMS シンポジウム (JAMS-25), つくば国際会議場, つくば市 (2025 年 3 月 25–26 日).

56. 松村万寿美, 高橋 努, 吉田哲郎, 松中哲也, 三河美紗希, 木村龍拓, 佐久間光紀, 高見勇楽, 森口哲朗, 笹 公和, “筑波大学 6 MV タンデム加速器質量分析装置における多核種 AMS と応用研究の現状” (2024 年度), 第 25 回 AMS シンポジウム (JAMS-25), つくば国際会議場, つくば市 (2025 年 3 月 25–26 日).

57. [CRiES Seminar] 三浦 輝, “加速器質量分析法を用いたヨウ素 129 の海洋動態解明”, 第 5 回 CRiES セミナー, 筑波大学 放射線・アイソトープ地球システム研究センター(CRiES), オンライン開催 (2024 年 9 月 10 日). （招待講演）

58. [UTTAC Seminar] 犬飼泰地, “ALICE FoCal 検出器のための読み出し集積回路 HGCROC2 および HGCROC3 の性能評価”, 筑波大学 CRiES 応用加速器部門, つくば市 (2025 年 1 月 10 日).

59. [UTTAC Seminar] 江阪成人, “RHIC-STAR 実験 $\sqrt{s}$ = 200 GeV p+p 衝突における正味電荷数ゆらぎの測定”, 筑波大学 CRiES 応用加速器部門, つくば市 (2025 年 1 月 10 日).

60. [UTTAC Seminar] 横尾岳斗, “LHC-ALICE 実験 鉛-鉛および陽子-陽子衝突におけるジェット内荷電パイ中間子と (反) 陽子の動径方向分布および運動量分布の高統計測定”, 筑波大学 CRiES 応用加速器部門, つくば市 (2025 年 1 月 10 日).

61. [UTTAC Seminar] Zhang Hanbin, “反応断面積測定に向けた厚さが一様な固体重水素標的の開発”, 筑波大学 CRiES 応用加速器部門, つくば市 (2025 年 1 月 10 日).

62. [UTTAC Seminar] 三浦 輝, 松中哲也, 笹 公和, 坂口 綾, “加速器質量分析法を用いたヨウ素 129 の海洋動態解明”, 2024 年度放射能環境動態・影響評価ネットワーク共同研究拠点年次報告会, 筑波大学 CRiES 応用加速器部門, つくば市 (2025 年 3 月 3 日).

63. [UTTAC Seminar] 一色萌衣, “Measurements of azimuthal anisotropy at forward and backward rapidity in $\sqrt{s_{NN}}$ = 19.6 GeV Au+Au collisions at RHIC-STAR”, 筑波大学 CRiES 応用加速器部門, つくば市 (2025 年 3 月 28 日).

7.

THESES

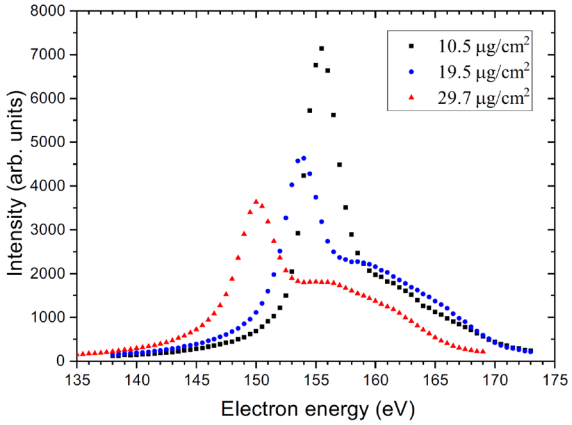

FIG. 2. Energy spectra around convoy electron peak obtained with 3.5-MeV/atom C_3^+ bombardment on carbon foils with a thickness of 10.5 μg/cm^2 (squares), 19.5 μg/cm^2 (circles), and 29.7 μg/cm^2 (triangles).

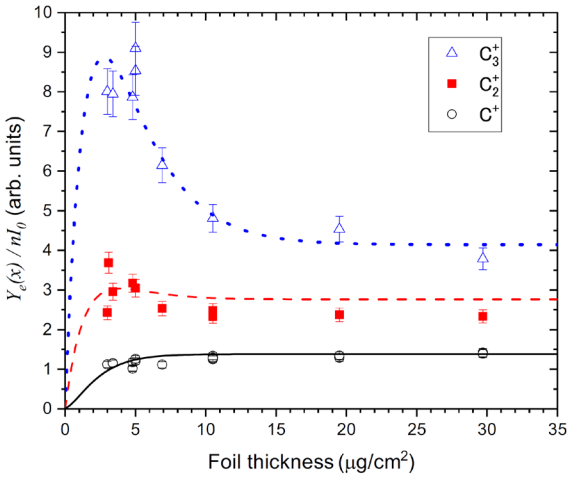

FIG. 3. Target thickness dependence of convoy electron yields for C_3^+ (open triangles), C_2^+ (filled squares), and C^+ (open circles). Lines indicate the calculated value of Eq. (6) for C_3^+ (dotted line), C_2^+ (dashed line), and C^+ (solid line).

velocity as a 3.5-MeV carbon atom is 160 eV. The position of the convoy electron peak exhibits a systematic downward shift with increasing target thickness, from 155.5 eV for 10.5 μg/cm^2 to 150 eV for 29.7 μg/cm^2. This shift directly reflects the energy loss of the projectile ions as they penetrate deeper into the material. Using the SRIM code [17], we calculated the electronic stopping power of 3.5-MeV/atom carbon ions in carbon foils to be 7.37 keV/(μg/cm^2). The calculated energy losses are 77, 144, and 219 keV for 10.5-, 19.5-, and 29.7-μg/cm^2 thick foils, respectively. These energy losses correspond to convoy electron energy

Figure 3 presents the target thickness dependence of the convoy electron yields normalized to the number of atoms in the cluster [$Y_e(x)/nI_0$]. This normalization allows us to observe the vicinage effect directly: If there were no cooperative effects between the constituent atoms, all curves would overlap. Instead, we observe that the normalized yield for C_2^+ and C_3^+ is consistently higher than that of C^+, demonstrating the enhancement beyond the simple scaling with the cluster size.

Convoy electron emission from thin foils induced by fast cluster ions exhibits synergistic effects among multiple projectiles that are never observed with fast monoatomic ions.

––Shiina et al., Phys. Rev. A 110 (2024) 062826.

Master theses

Zhang Hanbin	Development of a solid deuterium target with flat surfaces for reaction cross section measurements（反応断面積測定に向けた厚さが一様な固体重水素標的の開発）
OZEKI, Uta	Foil Thickness Dependence of Convoy Electron Yield in Diatomic Molecule Irradiation（二原子分子照射におけるコンボイ電子収量の膜厚依存性）
YAMAMOTO, Kazuki	Hydrogen analysis on Fomblin oil for neutron reflection material（中性子反射材料に向けたフォンブリンオイルの水素分析）
MINAMI, Rintarou	Estimation of the Fe valence and deposition rate of iron oxide thin films by combining plasma emission spectrometry and principal component analysis during reactive sputtering process（反応性スパッタリングプロセス中のプラズマ発光分析と主成分分析を組み合わせた酸化鉄薄膜の価数及び成膜速度の推定）
OZAWA, Mone (Kanazawa University)	Analysis for Vertical Profiles of polycyclic aromatic hydrocarbons in the Sea of Japan and Arctic Ocean（日本海および北極海における多環芳香族炭化水素類の鉛直分布解析）
KAWAKAMI, Kazuya	Characterization of thin HfO_2 films by means of positron annihilation spectroscopy (陽電子消滅法を用いた薄膜 HfO_2 層の空孔型欠陥の評価)

Undergraduate theses

KOBAYASHI, Hayato	Measurement of time of flight from Arc Plasma Source to investigate cluster ions （アークプラズマ蒸着源から出射するクラスターイオン探索のための飛行時間測定）
MATSUMOTO, Tatsuki	Estimation of Si powder target for measurement of magnetic moment of unstable ^{30}P（不安定核 ^{30}P の核磁気モーメント探索実験のための Si 粉末を用いた標的の評価）
KIMURA, Tatsuhiro	Estimation of the thermal neutron integral dose using $^{35}Cl(n, \gamma)^{36}Cl$ ($^{35}Cl(n, \gamma)^{36}Cl$ を用いた熱中性子積算線量の推定)
TAKAMI, Hayasa	Search for cosmic ray events in 990BCE using the cosmogenic nuclide ^{36}Cl（宇宙線生成核種 ^{36}Cl を用いた 990BCE の宇宙線イベント探索）
SAKUMA, Mitsuki	Interlaboratory comparison of the NIST standards for ^{129}I using Accelerator Mass Spectrometry（加速器質量分析を用いた ^{129}I 用標準試料の検定）
IWASAKI, Yoshimi	Measurement of Dissociation Products in Lifetime Measurements of Isolated Molecules（孤立分子の寿命計測における解離生成物の測定）

SINOHARA, Satoru	Reinvestigation of relationship between order parameter and symmetry breaking on second order phase transition（秩序パラメータと 2 次相転移における対称性の破れに関する再考察）
KANEKO, Tsugumi	Controlling the surface resistance of sapphire by nickel ion implantation for improving breakdown voltage（絶縁耐圧向上に向けたニッケルイオン注入によるサファイアの表面抵抗制御）
WASEDA, Ryutaro	Preparation of FeO thin films using reactive sputtering（反応性スパッタリング法を用いた FeO 薄膜の作製）
HORIE, Kazuma	Preparation of M-type La-Co-Sr ferrite fine particles using a molten salt method（溶融塩法を用いた M 型 La-Co-Sr フェライト微粒子の作製）

8.

LIST OF PERSONNEL

At the farewell party: Dr. Naramoto (second from the right) and Dr. Sataka (right) have long contributed to Open Advanced Facilities Initiative at UTTAC as core staff members.

Tandem Accelerator Complex

K. Sasa	Director, Associate Professor
D. Sekiba	Lecturer
T. Moriguchi	Assistant Professor
S. Ishii	Mechanical Engineer
T. Takahashi	Electrical Engineer
Y. Yamato	Electrical Engineer
T. Yoshida	Electrical Engineer
M. Matsumura	Technical Staff
H. Muromachi	Administrative Staff

Research Members*

Division of Physics

A. Ozawa T. Moriguchi K. Sasa

T. Yamaguchi (Saitama University [Cross appointment])

Division of Applied Physics

E. Kita D. Sekiba S. Tomita A. Uedono

H. Yanagihara H. Tanimoto A. Ogura S. Katagiri

K. Awazu (Visiting Professor) A. Taninaka (Visiting Associate Professor)

Division of Geoscience

M. Kurosawa

Division of Chemistry

A. Sakaguchi

Division of Medicine

H. Matsui H. Kurokawa (Visiting Researcher)

Division of Information and Systems

T. Kameda

Staff of Open Advanced Facilities Initiative

H. Kudo H. Naramoto M. Sataka

*__Research members__ and __External users and collaborators__ include authors and co-authors from the past three fiscal years, as well as members of research projects conducted at UTTAC.

Graduate Students

Graduate School of Science and Technology

N. Kishi	Z. Shi	A. Yano	Y. Kobayashi
M. Hiraga	U. Ozeki	Y. Yano	Y. Abe
T. Takahashi	H. Tanaka	R. Minami	T, Onuma
A. Hirata	K. Takeo	H. Zhang	M. Mikawa
M. Mitsui	M. Tabata	Y. Maeda	K. Yamamoto
R. Tanaka			

Undergraduates

Y. Kurihara	K. Endo	T. Miyazaki	Y. Iwasaki
T. Matsumoto	Y. Seki	H. Kobayashi	T. Kimura
M. Sakuma	H. Takami	T. Kaneko	K. Horie
R. Waseda			

Non-Degree Research Student

C. Shen

External Users and Collaborators*

S. Shiki	National Institute of Advanced Industrial Science and Technology (AIST)
H. Matsui	National Institute of Advanced Industrial Science and Technology (AIST)
T. Matsunaka	Kanazawa University
M. Rodorigo	Instituto de Investigaciones Tropicales de El Salvador
S. Nagao	Kanazawa University
Z. Dian	Kanazawa University
Y. Myogan	Kanazawa University
Y. Wakiyama	Fukushima University
H. Miura	Central Research Institute of Electric Power Industry
H. T. Shen	Guangxi Normal University
S. Seki	Kyoto University
M. Nobuoka	Kyoto University
W. Choi	Kyoto University
A. Taguchi	Kyoto University
H. Inoue	Kyoto University
H. Miyashita	Kyoto University
G. Yoshida	High Energy Accelerator Research Organization (KEK)
H. Matsumura	High Energy Accelerator Research Organization (KEK)

E. Ree	High Energy Accelerator Research Organization (KEK)
E. Watanabe	High Energy Accelerator Research Organization (KEK)
M. Ishida	High Energy Accelerator Research Organization (KEK)
K. Tsugane	High Energy Accelerator Research Organization (KEK)
R. Shiobara	Japan Environment Research co., LTD.
S. Yamazaki	Japan Environment Research co., LTD.
K. Oishi	Japan Environment Research co., LTD.
T. Suzuki	Saitama University
K. Takiura	Saitama University
Y. Kikuchi	Saitama University
S. Nishizawa	Saitama University
K. Watanabe	Saitama University
N. Tomitoka	Saitama University
I. Yasuda	Saitama University
R. Iwamoto	Saitama University
W. Yui	Saitama University
K. Ishiyama	Tohoku University
N. Kinoshita	Shimizu Corporation
K. Ishikawa	Nagoya University
F. Miyake	Nagoya University
A. Matsuzaki	Nagoya University
A. Iwase	Osaka Metropolitan University
H. Uno	SHI-ATEX Co., Ltd.
T. Shiobara	Nihon Dempa Kogyo Co., Ltd.
R. Onodera	National Institute of Technology, Ibaraki College
S. Kobayashi	The University of Tokyo
K. Kobayashi	Hitachi, Ltd.
M. Takahashi	Japan Aerospace Exploration Agency
M. Iwata	Japan Aerospace Exploration Agency
T. Suzuki	Japan Aerospace Exploration Agency
H. Okamoto	Ryoei Technica Corporation
A. Tsukino	Ryoei Technica Corporation
T. Kaneko	Ryoei Technica Corporation
S. Suzuki	Ryoei Technica Corporation
Y. Morishima	Ryoei Technica Corporation